Tarjei Hamre

Exploring the Modeling and Strength Prediction of Additively Manufactured Materials

Numerical and Analytical Approaches

Master's thesis in Mechanical Engineering
Supervisor: Filippo Berto

June 2019

Master's thesis

NTNU
Norwegian University of Science and Technology
Faculty of Engineering
Department of Mechanical and Industrial Engineering

NTNU
Kunnskap for en bedre verden

Tarjei Hamre

Exploring the Modeling and Strength Prediction of Additively Manufactured Materials

Numerical and Analytical Approaches

Master's thesis in Mechanical Engineering
Supervisor: Filippo Berto
June 2019

Norwegian University of Science and Technology
Faculty of Engineering
Department of Mechanical and Industrial Engineering

NTNU
Norwegian University of
Science and Technology

Preface

This thesis, written spring of 2019, concludes my two-year master of science program at the *Norwegian University of Science and Technology*, at the department of *Mechanical and Industrial Engineering*.

10 months ago, I started investigating the possibility of Additive Manufacturing of Solar Cells, after many a twist and turn, the direction of my thesis ended at a completely different and unexpected place. The directions always followed the most exciting path, and this free approach has indeed only increased my interest in the topic.

I am grateful to my supervisor Professor Filippo Berto, for having allowed me to work on a topic I wanted to explore further, letting me work independently, and providing a direction forward. I am honored to have been writing this thesis with you as my supervisor.

I am also thankful to Co-supervisor Klas Solberg for being available at all times. Your insights and help throughout the last year have been invaluable. Thank you for helping with the mechanical testing and use of SEM.

Tarjei Hamre, Trondheim, 2019

Abstract

Additive Manufacturing (AM) of metallic materials is an area of increased interest in the research community and the industry. The increased interest in this manufacturing method is attributed to its ability to manufacturing complex geometries. However, predicting the mechanical properties of an AM produced material comes with many challenges, rooted in non-negligible defects in the material, including surface roughness, porosities, and unmelted particles, which makes material characterization a challenging task. Accurate material properties are invaluable for achieving a successful Finite Element Analysis (FEA). This thesis seeks to explore the question of how AM produced materials could be modeled. How can properties of an AM produced material be estimated without extensive experimental work, specific for a single type of application? A review of several material models has been conducted. Ranging from simple phenomenological models to multiscale modeling of defects. The semi-analytical Gurson-Tvergaard-Needleman (GTN) model is suggested as a possible candidate for evaluating the reduced hardening by evaluating the amount of voids in the material. A multiscale approach is suggested as a possibility for estimating Elastic Properties.

In this thesis the effect of process parameters used in the manufacturing process is evaluated. Properties of AM produced Eutectic Al-Si alloy and 316L steel are investigated, and application of the GTN model to 316L steel is made on a tensile tested specimen. The work on estimating the Elastic and Plastic properties of AM produced materials is a valuable field of research that has the possibility of greatly benefiting the AM industry.

Sammendrag

Additiv tilvirkning av metalliske materialer er et felt som opplever økende interesse både i forskningsmiljøet og industrien. Den økende interessen for denne produksjonsmetoden tilskrives dens evne til å produsere komplekse geometrier. Å kunne forutsi de mekaniske egenskapene til et additivt tilvirket materiale kommer imidlertid med mange utfordringer, som er forankret i betydelige defekter i materialet, inkludert overflateruhet, porøsiteter og partikler, noe som gjør materialkarakterisering en utfordrende oppgave. Nøyaktige materialegenskaper er uvurderlige for å oppnå en vellykket elementanalyse. Denne oppgaven søker å utforske spørsmålene rundt hvordan additivt tilvirkede materialer kan modelleres. Hvordan kan egenskaper av et additivt tilvirket materiale estimeres uten omfattende eksperimentelt arbeid, spesifikt for en enkelt type applikasjon? En gjennomgang av flere materialmodeller har blitt gjennomført. Denne gjennomgangen strekker seg fra enkle empiriske modeller til multiskalert modellering av defekter. Den semi-analytiske Gurson-Tvergaard-Needleman (GTN) modellen er foreslått som en mulig kandidat for å evaluere den reduserte stivheten ved å evaluere mengden av porøsiteter i materialet. En multiskaleringstilnærming er foreslått som en mulighet for å estimere elastiske egenskaper.

Effekten av prosessparametere som brukes i produksjonsprosessen, blir evaluert. Egenskaper for additivt tilvirkede aluminium silisium legeringer og 316L stål undersøkes. GTN modellen er brukt til å modellere et additivt tilvirket 316L-stål. Arbeidet med å estimere de elastiske og plastiske egenskapene i additivt tilvirkede materialer er et verdifullt forskningsfelt som kan gagne industrien.

Contents

List of Figures

List of Tables

Nomenclature

B	Hardening Constant
E	Young's Moludus
E_d	Energy Density (AM)
K_{Ic}	Fracture Toughness
L_0	Original Length
P	Laser Power (AM)
S_N	Standard Deviation of Plastic Strain
S_{ijkl}	Eshelby Tensor
T	Temperature
T_m	Melting Temperature
T_r	Room Temperature
$\bar{\sigma}$	Flow Stress
Ω_{cube}	Cube Domain
Φ	Plastic Potential
$\boldsymbol{C}$	Stiffness Tensor
$\boldsymbol{I}$	Identity Tensor
$\boldsymbol{S}$	Stress Tensor for Voided Material
$\dot{\varepsilon}$	Strain Rate
$\dot{\varepsilon}_0$	Reference Strain Rate
λ_f	Magnitude of Flow
ν	Poisson's Ratio
σ	Stress
σ_b	Biaxial stress, (Hill 1993)
σ_h	Hydrostatic Stress
σ_y	Yield Stress
σ_{eq}	Equivalent Stress
σ_{ij}	Stress Tensor
σ_{th}	Threshold Stress, Fatigue
θ	Angle
ε	Strain
ε_N	Mean Value of Plastic Strain

ε_e	Elastic Strain
ε_f	Elongation at Failure
ε_p	Plastic Strain
ε_{ij}	Strain Tensor
f	Function / Void Volume Fraction / Yield Surface
f_0	Initial Void Volume Fraction
f_N	Void Nucleating Particle Fraction
f_c	Critical Void Volume Fraction
f_f	Void Volume Fraction at total Failure
h	Hatch Distance (AM)
l	Length
n	Strain Hardening Exponent / Number
q_1, q_2, q_3	GTN parameters
t	Thickness / Layer Thickness (AM)
v	Speed

Acronyms

Al-Si Aluminium Silicon.
AM Additive Manufacturing.
ASTM American Society for Testing and Materials.

BCC Body Centered Cubic.

CAD Computer-Assisted Design.
CT Computed Tomography.

DED Direct Energy Deposition.

EB Electron Beam.
EBM Elecron Beam Melting.

FCC Face Centered Cubic.
FEA Finite Element Analysis.

GTN Gurson-Tvergaard-Needleman.

HIP Hot Isostatic Pressing.

JC Johnson-Cook.

LEFM Linear Elastic Fracture Mechanics.

MT Mori-Tanaka.

PBC Periodic Boundary Conditions.
PBF Powder Bed Fusion.
PEEQ Plastic Equivalent Strain.
PPMM Process Parameter Mechanical behavior Model.

RVE Representative Volume Element.

SEM Scanning Electron Microscope.
SLM Selective Laser Melting.

UTS Ultimate Tensile Strength.

VVF Void Volume Fraction.

ZA Zerilli-Armstrong.

1 Introduction

1.1 Background

Additive Manufacturing (AM) is a term used to describe an iterative manufacturing process, where a part is built layer-by-layer guided by a Computer-Assisted Design (CAD), which enables the manufacturing of complex geometries through a one-step process [1]. The process has many advantages over traditional manufacturing processes, such as, high precision, geometric freedom, and little to none waste material. With the increasing development of technology and research in the field, the process has been adopted by the commercial industry and is currently being used in many engineering areas [2].

The materials produced by AM, however, inhabit some properties not seen in materials manufactured by traditional methods. The process of AM is known to induce defects in the material, which result in anisotropic behavior [3], and challenges in outlining the mechanical behavior. The defects induced in AM are not necessarily detrimental to the strength of the material, on the contrary, many materials produced by AM is known to be stronger than its casted counterpart [4, 5]. An abundant amount of experimental research on AM produced materials exists, where the primary focus has been on tensile, compression, and fatigue properties. However, there are fewer suggestions as to how these materials are best implemented in Finite Element Analysis (FEA), as well as suggested methods for estimating the resulting strength as a function of process parameters, be it analytical or empirical [6].

1.2 Problem Description

This thesis seeks to serve as a stepping stone for the development of a model relating process parameters to the mechanical behavior of AM produced materials. Such a model would benefit from being practical and straightforward, but it is also suggested that a robust model should be rooted in analytical work, rather than merely curve-fitting experimental results and achieve a phenomenological model. A review of several material models is conducted, and a suggested approach for implementation to AM produced materials is presented.

Porosities are proposed as the primary defect influencing material strength in AM produced materials. Thus, the present work primarily considers how to model reduced strength as a result of porosity content. Other factors, such as residual stresses, and melt pool properties are also seen as majorly influencing properties but are left out of the purposed methodology as some simplifications are considered most practical for this initial work.

1.3 Objective

The objective of this work is to suggest a suitable direction for future research on material modeling and strength prediction of additively manufactured materials.

1.4 Report Structure

This thesis concerns the elastic and plastic properties of AM produced materials. Firstly, the general concept of AM is presented, followed by a section on the general concepts of Elasticity and Plasticity, including the fundamentals of stress, strain, and material models. A review of defects in AM produced materials with a focus on eutectic Al-Si alloys and 316L steel follows.

After this, a selection of material models, relevant to the task of modeling properties of AM produced materials, has been reviewed and summarized. Then, the application of the GTN model is introduced through an initial parameter study. Multiscale modeling as a tool for strength prediction of porous metals in the elastic regime is investigated, and its benefits and limitations considered.

Next, a section considering the results of tensile tests of AM produced 316L steel follows. An attempt at curve fitting suitable equations for the stress-strain relationship, as well as a GTN model implementation for the material, is conducted. The overall findings in this thesis are discussed and summarized. Suggestions for further work on the topic concludes this thesis.

1.5 Literature

The literature used for this thesis includes journal papers concerning AM, which are summarized or used as a reference for explaining results. Fundamental concepts of structural integrity (Elasticity, Plasticity, and Fracture) are mainly adopted from textbooks. The textbooks are referenced before the chapter that they concern. Original publications on material models are used to explain plasticity theorems. However, most are accompanied by some secondary reviews and studies which can be sought out for further reading on each topic. Software and plugins are referenced appropriately as a courtesy to the programmers who have worked on these.

2 Additive Manufacturing

In this section, the general concepts of AM is introduced. An extensive review of AM is done by DebRoy et al. [2], a significant portion of the following sections is based on their findings and conclusions.

2.1 Additive Manufacturing, General Concept

AM is referred to with different names, additive fabrication, additive processes, additive techniques, additive layer manufacturing, freeform fabrication, 3D-printing, and many more [1]. The earliest application of AM dates back to the late 1980s with Chuck Hull patenting the 3D-printer [7]. However, only more recently, technology has reached the potential of becoming a fully viable commercial manufacturing process. This has led to the rise of more companies providing AM services and increased interest in research. In this section, the fundamental concepts of Additive Manufacturing will be introduced.

Additive manufacturing can be described as a layer-by-layer manufacturing process guided by a digital 3D-model [2]. Through a sintering process, a base material is iteratively formed into a solid part. The machines used for this manufacturing process is generally called 3D-printers, while there exist many machines with vastly different functionality under this umbrella-term, common for all is that 3D-printers utilize CAD software to guide the manufacturing process. Various software's of this type exist, SolidWorks, Autodesk, Siemens NX and Google SketchUp are some examples [2]. A typical file type used for 3D-printing is (.STL), a stereolithographic representation of the 3D-model. The information stored in this digital file gives information to the 3D-printer, which then reads, and constructs a 2D-cross section layer by layer [8]. During manufacturing, some geometries require a support structure for parts of the geometry. If a support structure is necessary, this can be removed with relative ease upon completion of the build. Upon completion of the build, the residual material can be reused for later parts, which means that with a one-step of manufacturing the part designer can have a physical model at hand. This provides an excellent opportunity for rapid prototyping, and such can play an essential role in the early stages of engineering projects. Being able to recreate problems physically makes for a more dynamic development process [9]. 3D-printing of plastics has for these reasons become a common tool in the design process, both in education and industry.

While the prototyping aspect of AM is an important one, this thesis concerns using AM for creating fully functional parts. There exist advantages of using AM over traditional manufacturing methods such as casting or tooling. These traditional methods often require several steps, and also limits the possible geometries, as the design has to account for the manufacturing method. The benefits of casting are apparent when there is an issue of mass production, but the benefits of AM is apparent when a small number of specialized parts are of concern. AM can also reduce the need of having spare parts available as they can be manufactured when needed. AM provides the opportunity for more complex geometries that are unthinkable to manufacture using traditional methods, such as that seen in Fig. 1. Enabling designers and engineers to achieve geometries that are perfectly suited for their purpose.

Currently, AM is not limited to plastics and other low mold temperature materials. AM of metals has been possible for several years, but with the enhancement of technology, new possibilities are frequently presented, and the field is undergoing huge developments. AM is still in its early stages of development, and it is not unreasonable to expect AM to develop into a production

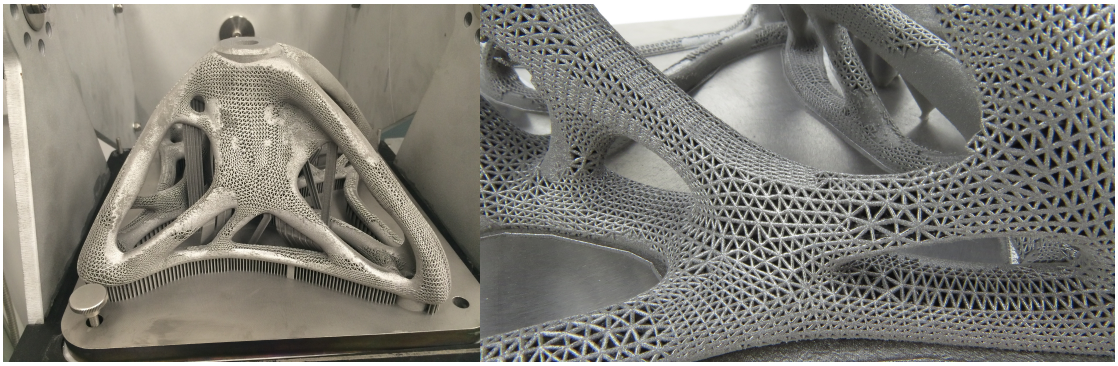

Figure 1: Example of a complex structure only possible to create using AM. This is a spider bracket in titanium created by Materialise using a Renishaw metal 3D printer. Topology optimized with a complex lattice system [10].

method used as widely as those most common today. For this to happen, there needs to be more research conducted in order to gain a better understanding of metallic parts produced by AM as well as further develop the manufacturing process, to ensure that the cost of manufacturing can rival that of traditional methods. If one compares the extensive research on, e.g., welding and the amount of knowledge and attention this area has seen throughout history, to the amount of research on AM of metallic parts, it is clear that it is a long road ahead for building an extensive knowledge in the field of AM [2].

Applications for AM produced metallic parts are many. Primary fields that can benefit from this production method are those where the cost comes secondary to weight reduction and functionality. Some possible fields of interest are aerospace, medical, energy, oil, and gas, automotive, marine, machinability and weldability, corrosion resistance applications, high-temperature applications, tools and molds, re-manufacturing and repair as well as consumer products [11, 12].

2.2 Additive Manufacturing Processes

This section provides an overview of the different processes in AM of metals, as well as an introduction to essential parameters in AM that will influence the properties of the completed build.

AM processes are differentiated through heat source and raw material supply system [3]. American Society for Testing and Materials (ASTM) separates AM processes into two categories, Direct Energy Deposition (DED) and Powder Bed Fusion (PBF). With DED systems, a nozzle supplies the raw material into the melt pool, while in PBF the material in powder form is selectively melted. Another source [1] separates AM processes into three categories, namely, powder bed systems, powder feed systems, and wire feed systems. Wire feed systems often require more extensive machining than PBF systems. Wire feed systems are relevant for larger sized objects, with lesser demands in terms of precision [1].

DED systems can also use powders for raw material supply and acquires high precision printing. The difference between PBF and DED lies in where the raw material is located during manufacturing. The heat source used in both processes is typically Laser or Electron Beam (EB). Both

Laser and EB provide high precision melting. DED systems may also make use of an electric arc as a heat source. This process commonly struggles with intricate features [2]. For the following discussion, electric arc as a heat source will be disregarded.

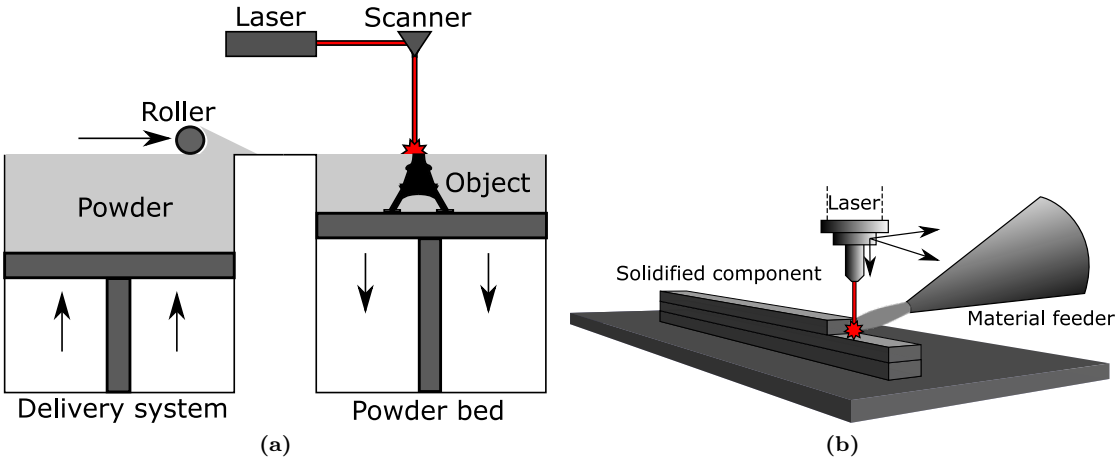

Figure 2: Illustration of (a) PBF system using a laser to sinter raw material from powder bed into a solid part (b) DED system in the form of a powder feed system, as nozzle and laser travels the part is generated layer-by-layer.

Both lasers and EB can focus heat in a small radius, the EB can have higher scanning speeds than Laser, but will only work on materials that can conduct electricity [2]. DED requires lower speed than PBF, 5-20 mm/s and 10-1000 mm/s respectively. With these processes, one can vary the heat given by the heat source as uniform or pulsed, which can affect the material properties [13]. The scanning can also follow different directions, such as unidirectional, bidirectional, zigzag, and other configurations. The applied scanning strategy is referred to as the hatching of the build.

With the primary focus of this report being on Al-Si and 316L steel, the most relevant processes are those of the PBF category, more specifically Selective Laser Melting (SLM) [14]. SLM generally produces higher quality surfaces than Elecron Beam Melting (EBM), at the cost of a longer production time [1].

Within PBF systems utilizing a laser, the literature often refers to different abbreviations. Note that SLM, Selective Laser Sintering (SLS) and Direct Metal Laser Sintering (DMLS) are in principle the same processes, mainly differentiated through the last letter in the abbreviation, i.e., Melting or Sintering. With SLS and DMLS the powder is fused via sintering, i.e., the particles are partially molten. Processes utilizing sintering often require post-treatments like secondary infiltration [15, 16]. SLM has a heat source that can completely melt powder-particles, and the build can often be utilized with little to no post-treatment. However, parts are shown to benefit from a post-build heat-treatment [17–19].

2.3 Cause of Defects in Additive Manufacturing

AM involves several parameters that will, in turn, affect the completed build, referred to as *Process Parameters*. All these parameters can be changed, resulting in a complicated process with many variables. As a result, it is quite challenging to predict, as well as control, the

outcome of the process in terms of the mechanical properties of the finished build. Variations in process parameters can change several aspects, including, but not limited to, residual stresses, surface quality, porosities, precipitates, cracking and grain structure [2]. Increasing the efficiency of production, lowering production cost, and improving the overall quality of parts produced by AM, are issues directly related to a better understanding of the processing techniques [20]. A problem related to this is the fact that detailed information regarding setup parameters is different depending on the machine used. Publications provide a different amount of detail concerning process parameters, making a comparison between results challenging.

With optimization of the SLM process, key process parameters are Laser Power, $P(W)$ Scanning Speed, $v(mm/s)$ Hatch Spacing, $h(\mu m)$ and layer thickness, $t(\mu m)$. These parameters are generalized to represent the energy density, $E_d(J/mm^3)$ of the process by Eq. (1),

$$E_d = \frac{P}{vht}. \tag{1}$$

A higher energy density will result in a slower and more energy-consuming process. To maximize the benefits of AM it is of interest to keep the cost of the process low. As will be presented later builds may benefit from high Energy Density in terms of mechanical properties. For non-critical regions of the geometry or parts that are not subjected to a large amount of load, one may decrease the energy density [21]. The Energy Density is not a reliable parameter in its own for predicting mechanical properties, as properties of the same AM produced material can vary even with E_d remaining constant [22]. This is also indicated by evaluating the collection of data on AM produced Al-12Sii in Appendix B. Laser power is determined to have a more significant influence on tensile properties than scanning speeds, and so Eq. (1) should only be used as an indication as to how much energy is being transferred to the powder bed [22].

Other primary process parameters for SLM than those included in Eq.1 are powder size and morphology, build plate temperature, pre-heating of the base plate or powder bed, and chamber gas [2]. In the following sections, an overview as to how these process parameters and corresponding induced defects may influence the mechanical properties of a material produced through AM.

2.3.1 Powder

Currently, there is a limited variety of alloys used in AM, those most used today are alloys that inhabit properties of interest in modern constructions and are also suited for AM, having a preferably low melting temperature, as well as ease in terms of powder production of the alloy. Common alloys in AM are those of steel, titanium, cobalt chrome, nickel, and aluminum [2]. The manufacturing of powders is done by three main processes: Gas Atomization, Water Atomization, and Plasma Atomization. Within these, there are other sub-categories to consider. Details on processing of powder can be found in Refs. [2, 15, 23, 24].

Depending on the process used for manufacturing the powder, its metallurgical properties can vary. Different size and shape, in turn, affects the formation of the melt pool and material structure of the build. In SLM, powders of small sizes and spherical morphology are preferred. The size of the powder affects the packing density and flow properties. Coarse powders are shown to induce larger voids acting as crack initiation sites [15]. With DED systems, where the powder is deposited through a nozzle, irregularly shaped particles can cause uneven distribution

of powder in the build. Schematics of how powder size and morphology may affect distribution (DED) and pack (PBF) are seen in Fig. 3.

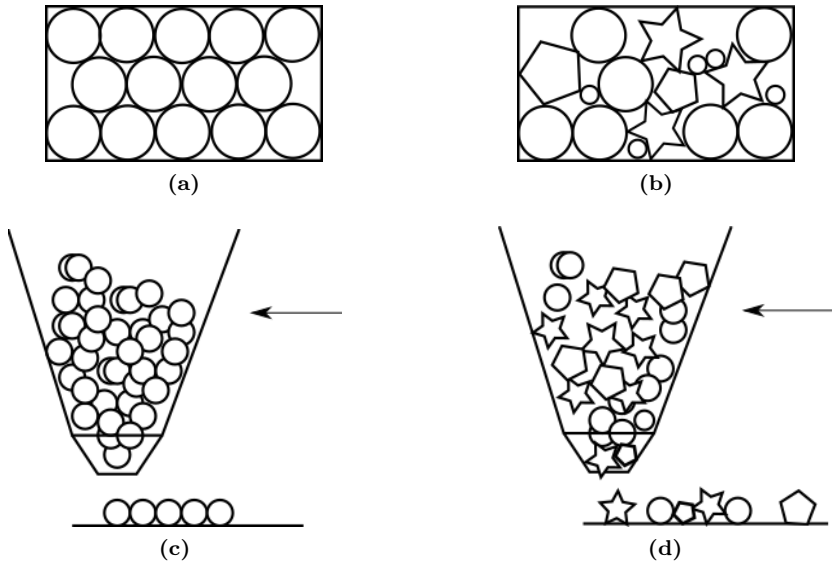

Figure 3: Simplified schematic illustrating the effect of powder morphology. (a) and (b) for a PBF system a uniform particle size makes the result more predictable. (c) and (d): If the particle shape differs, the nozzle in a DED system can possibly experience clogging, resulting in uneven distribution of powder.

2.3.2 Melt Pool

With AM, specifically SLM, the melt pool created by the heat source is a factor greatly influencing the mechanical properties of the completed build. As stated by Louvis et al. [25] "...SLM can be considered as the movement of a melt pool across a surface by the addition of powder at the front of the pool and the freezing of material at the back." The size of the melt pool is naturally dependant on the radius of the heat source. A laser provides a small radius (50 µm) while EB provides a larger(100 µm) [2].

Powder bed systems are known to provide the smallest melt pools due to the radius of the heat source but also the rapid scanning speed. High scanning speeds leads heat to linger in one place for a shorter time resulting in higher cooling rates of scanned areas. Wire feed processes can result in the largest melt pool size. This is due to the melt pool size being limited by the radius of the wire, which, depending on the material, can be several millimeters wide. Melt pools are considered to be one of the main sources of residual stresses, leading SLM to introduce larger amounts of residual stresses than processes that merely sinter material. More on the residual stresses of parts produced through AM in section 2.4.

The layer by layer melting naturally increases the temperature of not only the currently printed layer but also those below, and this leads each layer to be heated and cooled multiple times, meaning that the alloy in some cases is heated above phase transition temperatures several times, which in turn affects the microstructure of the finished build. This is a source for the specific

properties found in metals processed with AM [2]. There are various methods for predicting the temperature field created during PBF. This is a difficult task due to the many factors involved in the melting process. The heat source moves rapidly, and its interaction with the powder is governed by particle size. Estimates for melt pool size and shape can be made using FEA as well as other numerical and analytical approaches [26].

One of the primary criteria for a melt pool in SLM is that the heat source needs to be sufficient to melt particles in the intended area completely. Commonly some particles are left unmelted even after the successive heating of each area. These unmelted particles are typical in SLM of aluminum alloys, because of the oxide film naturally occurring on the border of the aluminum melt pool. The phenomenon was investigated thoroughly by Louvis [25], where it was suggested that the oxide layers trap unmelted particles in the region between two layer-wise successive melt pools, this effect is schematically shown in Fig. 4. The process parameters affect the seriousness of the areas with unmelted particles. The disrupted oxide in combination is also a source for weak spots in Al-based materials produced by AM [25, 27].

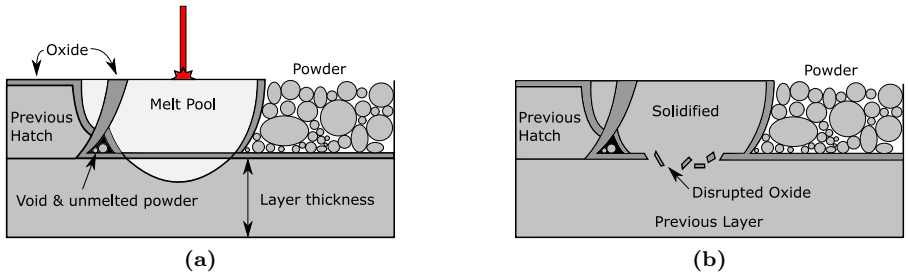

Figure 4: Schematic showing possible interaction between layer-wise successive melt pools in SLM of Aluminum alloys. Residual unmelted particles are trapped as a result of oxide layer interaction. Illustration adopted from Ref. [25].

Insufficient quality of Laser power, scanning speed and hatch distance can also cause *lack of fusion* [28], that is the size of melt pools are not sizeable enough to cause overlapping layers. The effect is schematically drawn in Fig. 5. The illustration is, of course, simplified. In a real print, the porosities would appear more randomly. Tang et al. [29], presented an analytical approach for estimating the lack of fusion porosities in AM produced materials by evaluating melt pool geometry. The amount of lack of fusion voids are seen to decrease with higher Energy Density (Eq. (1)), but at a certain value, the amount of porosities increase due to *Keyhole Porosities* [30]. Keyhole pores are attributed to a cavity forming due to alloying element essentially boiling [31]

2.3.3 Orientation

During AM, the layers are built upwards. Hence, how the material is oriented will affect the total number of layers needed for the build. A flat object will have fewer layers, while a tall needs many, affecting how many times each layer is heated and cooled. Experimental studies often observe different mechanical properties depending on the orientation of the test-specimen during manufacturing [33, 34]. Orientation specifications of test specimens of AM produced materials are standardized by ASTM [35]. The specification is included in Appendix A. Still, detailed information on printing directions in research publications is not always present [3].

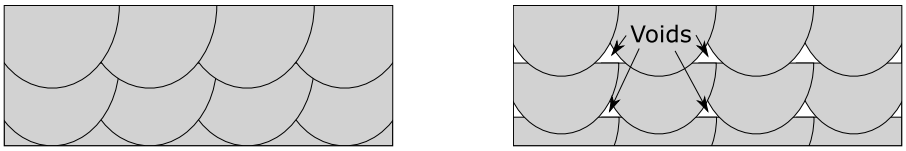

Figure 5: Lack of fusion porosity increase as the melt pool becomes smaller. (a) sufficient size, (b) insufficient size. Illustration adopted from [32].

In Lewandowski's review of Metal AM and mechanical properties [3], a large amount of research is summarized. Orientation dependence of mechanical properties is seen to be significant in most of the research which has specified orientation on the produced test-specimens. Orientation-dependent properties are generally seen to be more significant without post heat-treatment of produced parts [19].

2.3.4 Platform Temperature

With SLM, the first powder layer is fused onto the base substrate. The base substrate also referred to as build platform, can be heated to avoid nucleation of single-phase materials [2]. A heated base plate is also suggested as a means to reduce residual stresses within a finished build [16]. Base plate heating is also seen to neutralize orientation dependence of fatigue life as well as increase fatigue performance for AlSi10Mg [33]. Platform temperature is a factor that significantly influences the strength of the finished Al-Si builds. Some data on this for AM produced Al-12Si can be found in Appendix B.

2.3.5 Hatching / Scanning Strategy

The hatch distance refers to the distance between each line of scanning. The direction of the melt pool movement can be set to only one direction or alternate throughout the build [36]. With AM, the scanning direction can be changed after each layer or during each layer. The strategy used for scanning is shown to influence the material properties of the build. An alternating scanning direction is shown to affect the delamination in builds, as the border between melt pools overlap with alternating direction, making for stronger bonds [17, 25]. The alternating direction can, of course, be varied different angles and styles; some possibilities are shown in Fig. 6. When a print utilize a Checkerboard style hatch as in Fig. 6d the size of each square is commonly duped, *island size.*

2.3.6 Environment

As mentioned, a protective gas chamber is common in additive manufacturing, its job being protecting the sample from oxidation. While EBM processes prefer to vacuum, SLM commonly uses argon or helium gas [2]. In terms of Al-12Si, the effect of the atmosphere has been investigated and can be assumed to have an insignificant influence on the hardness of the build [37]. However, a helium environment produced samples with significantly lower Ultimate Tensile Strength

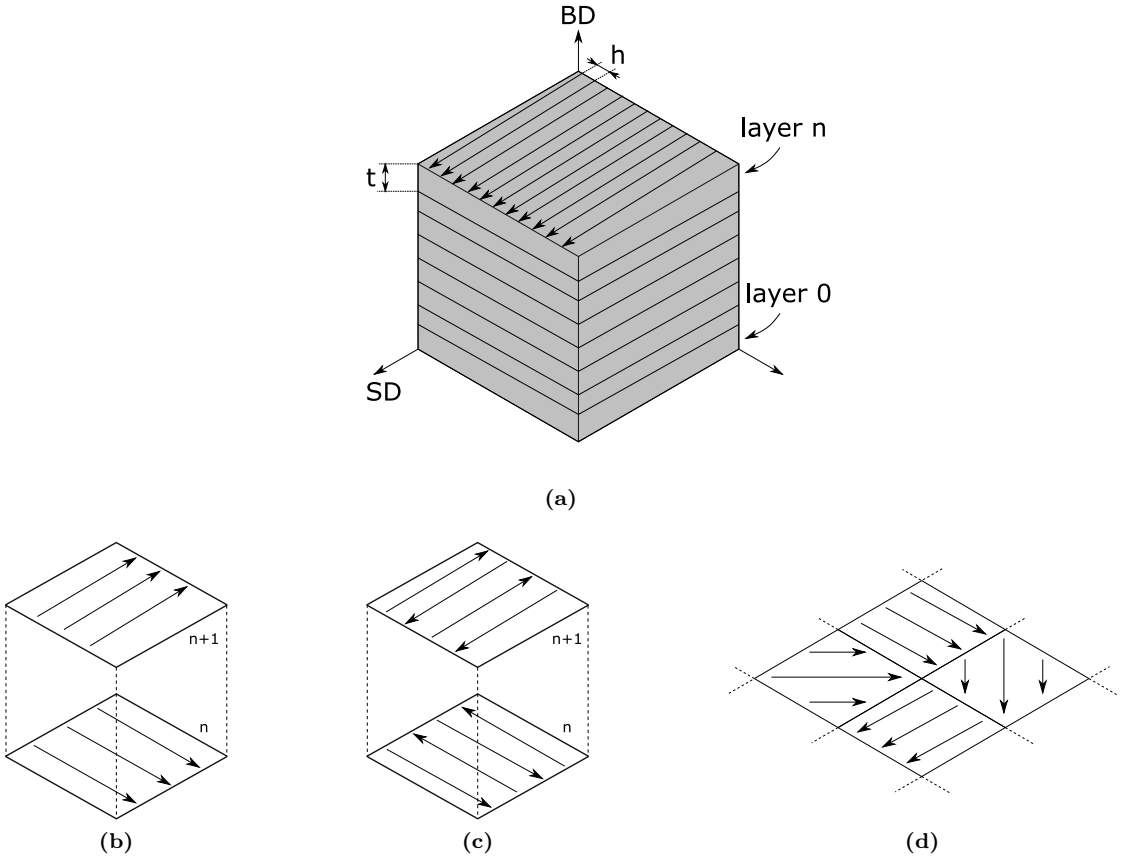

Figure 6: Examples of different types of hatching. (a) showing a complete build with a single scanning direction. (b) the next layer using scanning direction a scanning direction perpendicular to the last. (c) as (b) but using a continuous melt style. (d) A checkerboard style of hatching, with the melt pool moving in smaller squares, each square has a different angle.

(UTS) and elongation at failure. The effect is attributed to the presence of porosity clusters, which act as crack initiation sites [37].

2.4 Residual Stress in AM

Residual stresses are prevalent in parts produced by AM, likely due to the thermal gradients and rapid cooling rate present [16]. It is challenging to predict the residual stresses in AM produced parts; this is especially true for large-sized parts with complex geometry [2].

Residual stresses are stresses that are present in a material, often accumulated during manufacturing. The stresses are present when the part is at equilibrium with its environment and affects the parts strength to a significant degree [16]. If high tensile residual stresses are present, the material in a sense experience stress before tensile loading occurs, leading to reduced recorded strength. The opposite can be said for compressive residual stresses [38]. The residual stresses also promote crack propagation from the surface.

In SLM, the primary mechanism introducing stress is the temperature gradient associated with the melt pool. The rapid heating of the upper surface causes a difference in the strength of the area affected by the Laser and the surrounding area. Upon cooling a bending towards the Laser occurs and stresses propagate in the material. In SLM this effect also occurs in layers below the current, because the heat travels through previous layers. Fig. 7 illustrates this effect in a simplified schematic. If the residual stresses between layers in the build become too large, this can result in delamination between layers.

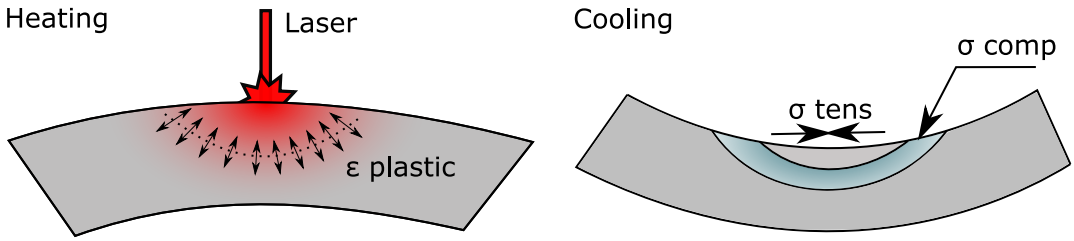

Figure 7: Temperature gradient inducing residual stresses [16].

Mercelis et al. [16] introduced a simplified analytical approach, as well as an experimental approach to investigate the mechanisms promoting residual stresses inAMas well as their distribution. Some of the conclusions drawn are presented here. A particularly exciting proposal is that the thickness of the plate should influence the amount of residual stress. During the constant heating and cooling, the base plate is expected to bend and deform differently than the part, in turn, affecting the part. A thin build plate should, therefore, promote more considerable residual stresses.

A summary of findings presented by Mercelis et al. [16] is,

- The residual stresses depend on the properties of the build plate to a large degree. This is due to a large difference in the stress field of the plate and the part.
- The more layers added in the build, the larger the final residual stress.
- A material with a high yield strength used in printing should result in higher residual stresses.
- Residual stresses appear in regions of the build. Below the upper surface, there is a region of tensile stress, followed by a region of compressive strength in the middle, and then another region of tensile stresses near the build plate. This distribution is presented in fig 8.

Siddique et al. [21] investigate the effect of base plate heating on residual stresses. A base plate heating of 200°C decreases residual stresses in AM produced Al-12Si specimens. The as-built parts residual stresses decreased from 36 MPa to 8 MPa, which is significant.

Residual stresses in AM produced parts are also investigated on the alloys Ti-6Al-4V, and IN 718 [26], where thin layers and a high E_d, are shown to reduce residual stresses. The residual stress distribution in the build direction shown in Fig. 8, is also found to be the case in this study. However, the magnitude decreases with an increasing amount of layers, contrary to what is suggested by Ref. [16].

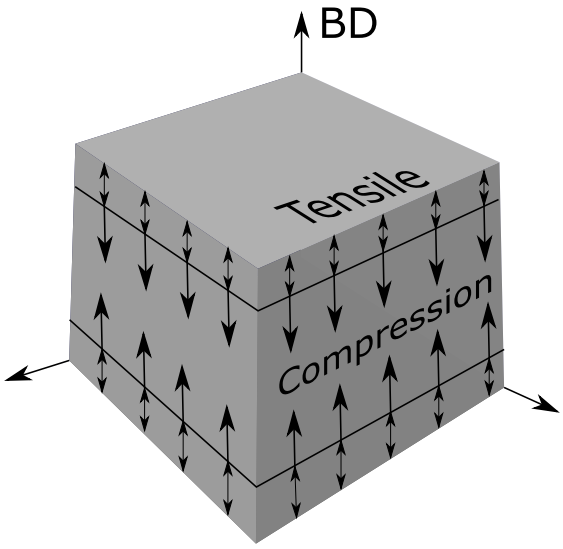

Figure 8: Proposed distribution of residual stresses in a cubic SLM part. The distribution is attributed to difference in stress field of part and build plate [16].

Residual stresses in AM is not something that necessarily is detrimental to strength. It is suggested that residual stresses may benefit tensile ductility or stable plasticity [39]. Study on residual stresses in AM produced parts remain a large area of interest for developing further understanding of the mechanical properties of a AM build.

3 Theoretical Background

The history of a material undergoing loading can in principle be divided into three sections, "elastic regime," "plastic regime," and "fracture." The theoretical background in the following section is divided into six sections, the first establish some basic formulas for the elastic regime, followed by an introduction to the Eshelby tensor, which further expands on the theory of elasticity. Next, a more comprehensive introduction to the plastic regime follows including an introduction the the normality flow rule. Fracture and failure of materials is also introduced.

The following sections are primarily based on the books, "Mechanical Behavior of Materials" by Hosford W.F. [40], "Mechanical Behavior of Materials" by Dowling N.E. [38], "Theory of Elasticity and Plasticity" by Westergaard H.M. [41], "Introduction to Computational Plasticity" by Dunne F. and Petrinic N. [42] and "Fracture Mechanics, Fundamentals and Applications" by Anderson T.L [43].

3.1 Theory of Elasticity

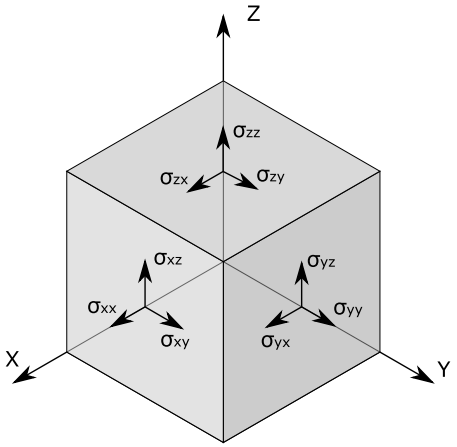

Figure 9: Cauchy stresses.

In describing the stress state of a body, the stresses are represented by a second-order tensor. This representation is commonly referred to as the Cauchy stress. The stress-components in the primary axis directions are the normal stresses, and the plane stresses are shear components. τ is commonly used for shearing stresses.

$$\boldsymbol{\sigma} = \begin{bmatrix} \sigma_{xx} & \sigma_{xy} & \sigma_{xz} \\ \sigma_{yx} & \sigma_{yy} & \sigma_{yx} \\ \sigma_{zx} & \sigma_{zy} & \sigma_{zz} \end{bmatrix} = \begin{bmatrix} \sigma_{11} & \sigma_{12} & \sigma_{13} \\ \sigma_{21} & \sigma_{22} & \sigma_{23} \\ \sigma_{31} & \sigma_{32} & \sigma_{33} \end{bmatrix} = \sigma_{ij} \tag{2}$$

The stresses can also be represented using Einstein's summing convention for shortening the expression. In this case the stresses can simply be duped σ_{ij} where both i and j run the interval $[1, 2, 3]$. Thus, all nine components are described. For the principal stresses, σ_{kk} is commonly used to differentiate. In this thesis the principal stresses are also seen written as σ_1, σ_2 and σ_3. By averaging the principal stresses, the hydrostatic stress also referred to as the mean normal stress, is achieved,

$$\sigma_h = \frac{\sigma_{kk}}{3} \tag{3}$$

A material responds to stress by deforming, the fractional change in length is called strain (ε) and is defined as,

$$\varepsilon = \frac{\Delta L}{L_0} \tag{4}$$

Where L_0 is the original length and ΔL is the current length subtracted by the original length. Strain can also be defined as a tensor, being the differential of displacement (u),

$$\varepsilon_{ij} = \frac{1}{2}(u_{i,j} + u_{j,i}) \tag{5}$$

In the elastic regime, the material assumes a linear stress-strain relationship. The material behaves much like a spring, in which all strain is recovered upon unloading. In this regime Hooke's law is applicable. In a unidirectional loading case the linearized Hooke's law can be expressed as,

$$\sigma = E\varepsilon. \tag{6}$$

Where the slope of the linear relationship, is the Young's Modulus E. Hooke's law in the generalized tensorial form is,

$$\sigma_{ij} = \boldsymbol{C}_{ijkl}\varepsilon_{kl}. \tag{7}$$

Where $\boldsymbol{C}_{ijkl}$ is the fourth order stiffness tensor. As the material is elongated in one direction, it also contracts in the perpendicular direction. The ratio of transverse to axial strain is called Poisson's ratio, ν. In three dimensions Hooke's law is expressed as [40],

$$\begin{aligned}
\varepsilon_x &= \frac{1}{E_x}[\sigma_x - \nu_x(\sigma_y + \sigma_z)], \\
\varepsilon_y &= \frac{1}{E_y}[\sigma_y - \nu_y(\sigma_x + \sigma_z)], \\
\varepsilon_z &= \frac{1}{E_z}[\sigma_z - \nu_z(\sigma_x + \sigma_y)].
\end{aligned} \tag{8}$$

Or in the generalized form,

$$\varepsilon_{ij} = \frac{1}{E}((1+\nu)\sigma_{ij} + \nu\delta_{ij}\sigma_{kk}) \tag{9}$$

Where δ_{ij} is the Kronecker delta, $(1\, for\, i = j)$, and $(0\, for\, i \neq j)$. For a state of pure shear, that is, stress only acts in one shear direction, the material's shear modulus in terms of E and ν may be evaluated as [40],

$$G = \frac{E}{2(1+\nu)}. \tag{10}$$

If a material inhabits the same behavior regardless of which direction it is loaded, it is called *isotropic*, i.e., $E_{11} = E_{22} = E_{33}$ and similarly for the Poisson's ratio, ν. Only two constants thus express the material's elastic properties. If a material is *orthotropic*, its properties are symmetric over three planes, in matrix form the elastic properties are expressed through nine elastic constants.

$$\begin{bmatrix} \varepsilon_{11} \\ \varepsilon_{22} \\ \varepsilon_{33} \\ \varepsilon_{12} \\ \varepsilon_{13} \\ \varepsilon_{23} \end{bmatrix} = \begin{bmatrix} \frac{1}{E_{11}} & -\frac{\nu_{21}}{E_{22}} & -\frac{\nu_{31}}{E_{33}} & 0 & 0 & 0 \\ -\frac{\nu_{12}}{E_{11}} & \frac{1}{E_{22}} & -\frac{\nu_{32}}{E_{33}} & 0 & 0 & 0 \\ -\frac{\nu_{13}}{E_{11}} & -\frac{\nu_{23}}{E_{22}} & \frac{1}{E_{33}} & 0 & 0 & 0 \\ 0 & 0 & 0 & \frac{1}{G_{12}} & 0 & 0 \\ 0 & 0 & 0 & 0 & \frac{1}{G_{13}} & 0 \\ 0 & 0 & 0 & 0 & 0 & \frac{1}{G_{23}} \end{bmatrix} \begin{bmatrix} \sigma_{11} \\ \sigma_{22} \\ \sigma_{33} \\ \sigma_{12} \\ \sigma_{13} \\ \sigma_{23} \end{bmatrix} \tag{11}$$

The matrix relating stresses and strain in Eq. (11), is C^{-1}_{ijkl}, and called the material compliance matrix. If a material has no planes of symmetry, i.e., different properties in all directions the material is called *anisotropic* and requires a maximum of 21 elastic constants.

When a material is stressed, small volume changes occur. The small change in volume to the original volume is called the volumetric strain, which is represented as [38, 41],

$$\varepsilon_v = \frac{3(1-2v)}{E}\sigma_h \tag{12}$$

Eq. (12) serves as a proof that ν, may never exceed 0.5, as this would lead to a negative ε_v, which corresponds to decreasing volume upon loading. The volumetric strain in metals is often so small that it can be considered negligible. Typical values for E and ν seen in many steels are, $E = 200GPa$ and $\nu = 0.3$, for this case, a hydrostatic strain of 100 MPa corresponds a volumetric strain of 0.1 %.

The simplest form of material physics is in the elastic regime, where stresses and strains are linearly dependent. As described by Westergaard [41], stresses in a body are not uniform; they are rather irregular due to micro- or macroscopic structures within the material. Modeling the behavior at such a small scale is not practical for most applications. The simplifications made to simulate the behavior without regarding these small scale factors, are the foundation of the field of *continuum mechanics*.

3.2 Ellipsoidal Inclusions in an Isotropic Elastic Material

For an ellipsoid, as illustrated in Fig. 10 it's shape may be represented in the Cartesian coordinate system as [44],

$$\left(\frac{x_1}{a_1}\right)^2 + \left(\frac{x_2}{a_2}\right)^2 + \left(\frac{x_3}{a_3}\right)^2 = 1 \tag{13}$$

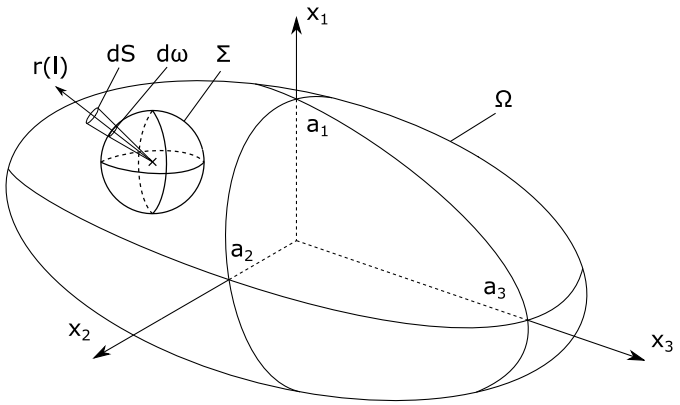

Figure 10: Three-dimensional ellipse with illustrated integration scheme used in the derivation of the Eshelby tensor.

As this ellipse is an inclusion in a solid, the question of a difference in, properties between the matrix material and the inclusion may affect the stress and strain distribution throughout the material. This problem was tackled by Eshelby, in 1957 [45]. The solutions presented in his paper have been widely adopted, and are still used today in the development of micromechanics models for strength assessment [46, 47].

A summary of the solution to this problem is presented here. A complete version may be found in Refs. [44, 48]. An inclusion will lead to concentrated stresses at the inclusion boundary. Eshelby's solution involves the operations of removing the ellipsoidal inclusion from the matrix, expanding it by uniform strains when inserted back into the matrix material, the matrix reach equilibrium through imposed tractions [47, 48].

From Green's functions $G(x - x')$, we have the equation for displacement as,

$$u_i(x) = \frac{-\varepsilon^*_{jk}}{8\pi(1-\nu)x} \int_\Omega g_{ijk}(\boldsymbol{l}) \frac{\mathrm{d}x'}{|x' - x|^2} \tag{14}$$

Which is solved by the relation,

$$\mathrm{d}\boldsymbol{x}' = \mathrm{d}r\mathrm{d}S = \mathrm{d}r r^2 \mathrm{d}\omega \tag{15}$$

By using a unit sphere centered at point x and integrating over the volume x'. ($\mathrm{d}x'$ being the volume element of the inclusion.) This unit sphere may be denoted Σ. The result is,

$$u_i(x) = \frac{-\varepsilon^*_{jk}}{8\pi(1-\nu)} \int_\Sigma r(\boldsymbol{l}) g_{ijk}(\boldsymbol{l}) \mathrm{d}\omega. \tag{16}$$

Where ω, is the area of the unit-sphere surface. After integrating this, (details found in Ref. [44]), the Eshelby tensor appears as a relation between strains and eigenstrains.

$$\varepsilon_{ij} = S_{ijkl} \varepsilon^*_{kl} \tag{17}$$

As a quick example, the Eshelby tensor may be expressed as a function of the aspect ratio of the ellipsoidal inclusion, $\alpha = {}^{a_1}/_{a_3}$. For a prolate spheroid such as that shown in Fig. 10 The Eshelby tensor is [49],

$$S_{1111} = \frac{1}{2(1-\nu_m)}\left[\frac{4\alpha^2-2}{\alpha^2-1} - 2\nu_m - g(\alpha)\left(a - 2\nu_m + \frac{3\alpha^2}{\alpha^2-1}\right)\right]. \tag{18}$$

Where ν_m is the matrix Poisson's ratio and $g(\alpha)$ is,

$$g(\alpha) = \frac{\alpha}{(\alpha^2-1)^{3/2}}[\cos^{-1}\alpha - \alpha(1-\alpha^2)^{1/2}]. \tag{19}$$

For other inclusion geometries, these equations take different forms, a variety of solutions of the Eshelby tensor can be found in Ref. [44].

The main result from Eshelby's solution is that "For an ellipsoidal inclusion in a homogeneous infinite matrix, the Eshelby tensor S_{ijkl} is a constant tensor. Hence the stress-strain fields inside the inclusion are uniform." [48].

3.3 Introduction to Yield and Plasticity

In the plastic regime, strains cause permanent deformation of the material. The yield stress σ_y is the threshold value for the onset of plasticity. After this point, the material deforms more non-linearly and acquire irreversible changes in shape. Commonly it is assumed no volume change as plasticity progress. An exception to this is in the case of porous materials, where void growth and nucleation cause macroscopic volume changes. Plasticity is also not considered explicitly time dependant [50].

In discussing plasticity, sources may use different subscripts, superscripts, or symbols to describe the same thing, each symbol should be explained, but for a complete guide, the reader is referred to the nomenclature.

For a stress-strain relationship, e.g., Fig. 12b, the strain can be separated into elastic strain and plastic strain,

$$\varepsilon = \varepsilon_e + \varepsilon_p. \tag{20}$$

This formulation is the classical additive decomposition of strain. For a small strain, one can denote the plastic strain as the strain minus that strain governed by linearized Hooke's law (Eq. (6)) if it would still apply. For a unidirectional tensile test, this translates to the material being relaxed by the slope of Young's modulus if unloading occurs before reaching the UTS. The behavior is illustrated in Fig. 11.

Stress and strain are related through the general concept,

$$\sigma = g(\varepsilon) \; or \; \varepsilon = h(\sigma) \tag{21}$$

Where g and h are arbitrarily chosen functions in this preliminary discussion. In an experimental tensile test without strain gauges or extensometers, one achieves load (F) and displacement (D).

The accuracy of stress calculated as $\sigma_{eng} = {}^{F}/_{A}$, (engineering stress) decreases as the load increases, and the cross-sectional area decreases. For strains, $\leq \varepsilon_y$ the engineering stress may be seen as true, as the difference achieved by accounting for cross-sectional area reduction is minuscule. However, as the material deforms plasticly the area-reduction could be significant, and the engineering stress is increasingly more innacurate. In this case one could make use of an approximation in order to achieve a more realistic stress-strain relationship. By assuming that strain described by Eq. (4) is only valid for a small portion of the length, integrate over the initial length L_0 to current length L and achieve [40],

$$\varepsilon_{true} = \ln \frac{L}{L_0} = \ln (1 + \varepsilon_{eng}) \tag{22}$$

True stress is obtained by,

$$\sigma_{true} = \sigma_{eng}(1 + \varepsilon_{eng}) = \sigma_{eng} \mathrm{e}^{\varepsilon_{true}} \tag{23}$$

These approximations require the cross-section to remain uniform throughout loading, as well as assuming the volume remains constant. Thus, they are not applicable after the UTS, is reached and necking initiates [40]. The valid regime for Eq. (22) and (23) corresponds to the region denoted as "plasticity" in Fig. 11, for an approximation of true stress and strain after this region other measures must be taken [51]. The phenomenon of necking is further described in Section 3.5. For the rest of this section, concerning the theory of plasticity, the material is assumed not to undergo necking.

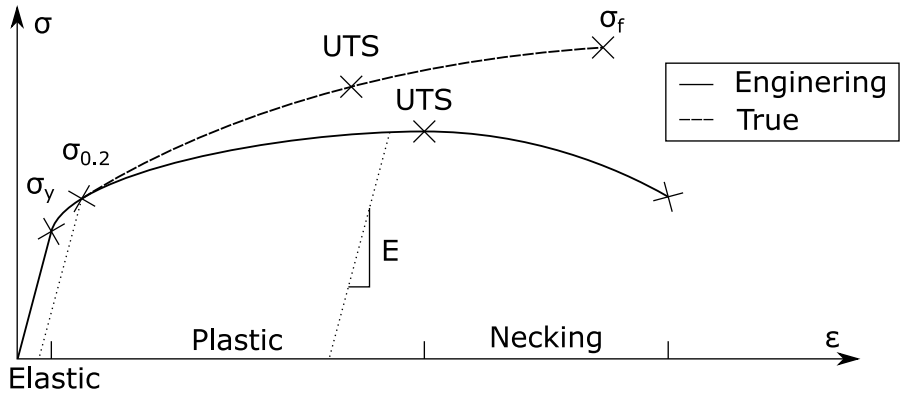

Figure 11: A representation of a typical Stress Strain curve for ductile metals. The true stress is higher than the engineering, as well as slightly shifted.

When σ_y is reached, each increment of further added stress, renew the material. That is, its properties change. For a unidirectional tensile test, one can determine the yield as a point. Translating this to two or three dimensions is done using what is known as a *yield criterion*. For theorems describing plasticity three aspects are considered.

A1: Satisfaction of a yield criterion. For an isotropic, homogeneous material, a yield criterion $f = 0$ would be true if,

$$f = \sigma - \sigma_y = 0 \tag{24}$$

Where σ_y is the material's yield stress and σ is the applied stress. From this, it can be said that $f \leq 0$ means the deformation has not caused yield, and $f = 0$ is the yield criterion.

A2: Satisfaction of equilibrium. A fundamental basis for all physics is that forces in a stable system must be in equilibrium. For plasticity in materials, this corresponds to a requirement of equilibrium between the internal forces in the body, and the external forces on the surface.

$$\sum F = 0 \implies \sigma_{external} = \sigma_{internal}. \tag{25}$$

A3: Collapse mechanism. A critical load will cause collapse in the structure, which governs a given mechanism.

A *lower bound plasticity theorem* states that if the applied load is less than the critical load, the system will not fail. The critical load is approached from a lower value, i.e., $F_{lower} \leq F_{collapse}$. Thus, A1 and A2 are satisfied

An *upper bound plasticity theorem* states that a set of internal forces can be identified which exceeds the given collapse load. This means we can approach the collapse load from above, i.e. $P_{upper} \geq P_{collapse}$. Upper Bound theorems does not satisfy the yield criterion but will be based on the collapse mechanism. Thus, A2 and A3 is satisfied.

The *uniqueness theorem* will be at the exact collapse load, and such satisfy equilibrium (A2), yield criterion (A1), and collapse (A3).

The difference between a lower bound theorem and an upper bound theorem is consequently; how one approach the collapse load. Detailes on the foundation of plasticity theorems can be found in Ref. [52].

The Tresca and von Mises yield criterions are the most common and well-known. *The Maximum Distortion Theorem* or von Mises Criterion states that for a two-dimensional stress case, the *Equivalent stress* is,

$$\sigma_{eq} = \frac{1}{\sqrt{2}}[(\sigma_1 - \sigma_2)^2 + \sigma_2^2 + \sigma_1^2]^{\frac{1}{2}}. \tag{26}$$

Substituting Eq. (26) into Eq. (24), with the equivalent stress being the applied, gives,

$$\sigma_1^2 + \sigma_2^2 - \sigma_1\sigma_2 = \sigma_y^2. \tag{27}$$

This results in the familiar von Mises ellipse for stress in two dimensions [42]. The elliptical yield criterion extends to a cylinder with its center axis along the $\sigma_1 + \sigma_2 + \sigma_3 = 0$ axis for three dimensions. The 2D ellipse in Eq. (27) is the cylinder cut by the $\sigma_3 = 0$ plane. For three dimensions the equivalent stress is given by,

$$\sigma_{eq} = \frac{1}{\sqrt{2}}\left[(\sigma_1 - \sigma_2)^2 + (\sigma_2 - \sigma_3)^2 + (\sigma_3 - \sigma_1)^2\right]^{\frac{1}{2}}. \tag{28}$$

Although an ellipse is not the only option for a yield criterion, the von Mises ellipse will be used to represent a yield surface in the following examples. A material loaded in some vector of direction 1 and 2 reach plasticity when the resultant vector equals the yield criterion. When the stress exceeds the radius of the ellipse, the material is in the plastic regime. Hooke's law no

longer applies, and more sophisticated methods are needed to describe the material behavior. There is, a vast number of different plastic behaviors, and such also a significant number of ways to represent the evolution of plastic strain and stress.

If the yield criterion is considered an ultimate limit of the load-bearing, that is, the stress can not exceed that of σ_y, the material is considered to experience *Perfect Plasticity*, this behavior is shown in Fig. 12a. Normally a material hardens when the stress exceeds its yield point, this attribute is called *strain hardening*. The property can be explained as a result of microstructural changes that are adapting to the loading condition. The plastic stress is commonly duped *Flow Stress* and is abbreviated $\bar{\sigma}$, the word "flow", acknowledging the irreversible changes in deformation. During hardening, the yield criterion changes and so Eq. (24) still holds. This feature is called the associated flow rule, some aspects related to this is further discussed in Section 3.4. For *Isotropic Hardening* the yield criterion expands in all directions during plastic deformation, i.e., the von Mises yield loci stays symmetric over $\sigma_1 = \sigma_2$, regardless of the direction it is loaded in, see Fig. 13. For this case, after plasticity is reached, the yield criterion is,

$$f(\sigma, \varepsilon_p) = \sigma_e - \sigma_y(\varepsilon_p) = 0 \tag{29}$$

Where ε_p is the plastic strain. And,

$$\sigma_y(\varepsilon_p) = original\, yield + hardening = \sigma_{y0} + r(\varepsilon_p) \tag{30}$$

$r(\varepsilon_p)$ is the parameter of interest in this preliminary discussion. What follows are a few examples of the shape this function can take depending on what hardening behavior the material undertakes during tensile stress. Note that as the material hardens during plastic deformation, the stress still needs to change in order for plasticity to continue. The forms of $r(\varepsilon_p)$ are adopted from Ref. [42].

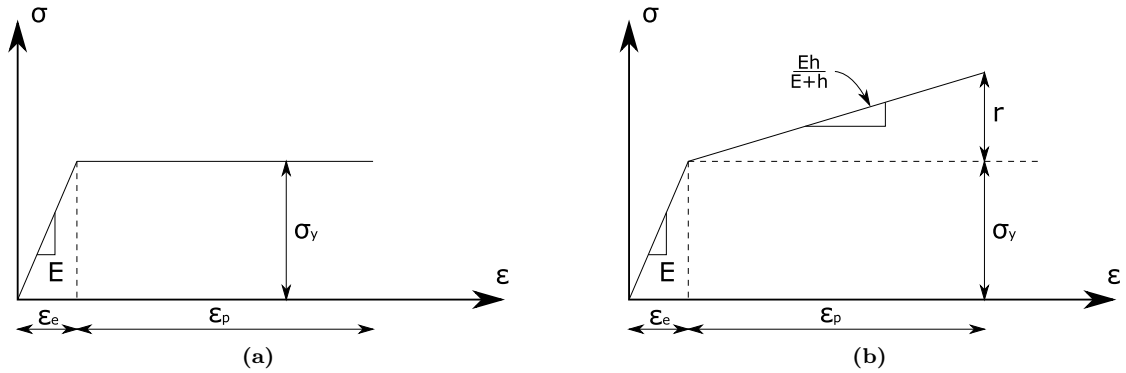

Figure 12: (a) Perfect Plasticity, (b) Linear Hardening.

The simplest form for a non-zero $r(\varepsilon_p)$ is that of linear hardening (See Fig. 12b). For this case, solve,

$$\mathrm{d}r(\varepsilon_p) = h\mathrm{d}p, \tag{31}$$

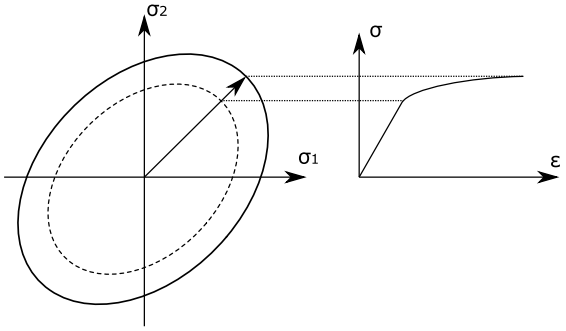

Figure 13: Isotropic hardening.

$$\mathrm{d}\varepsilon_e = \frac{\mathrm{d}\sigma}{E},\ \mathrm{d}\varepsilon_p = \frac{\mathrm{d}\sigma}{h}. \tag{32}$$

Substituting Eq. (32) into Eq. (20), gives,

$$\mathrm{d}\sigma = \frac{Eh}{E+h}\mathrm{d}\varepsilon. \tag{33}$$

This means the graph for a unidirectional tensile test, with linear isotropic hardening, can be determined with one additional material constant, h, which denotes the slope of the plastic deformation part of the material.

$$\sigma = \begin{cases} E\varepsilon & \text{if } \varepsilon \leq \varepsilon_p \\ \frac{Eh}{E+h}\varepsilon & \text{if } \varepsilon > \varepsilon_p \end{cases} \tag{34}$$

Another approach is that of non-linear isotropic hardening, see Fig. 13.

$$dr(\varepsilon_p) = b(Q - r(\varepsilon_p))d\varepsilon_p \tag{35}$$

Where b and Q are constants. Solving this differential equation with $r(0) = 0$,

$$\int \frac{\mathrm{d}r(\varepsilon_p)}{\mathrm{d}\varepsilon_p}\frac{1}{Q - r(\varepsilon_p)}\mathrm{d}\varepsilon_p = \int b\mathrm{d}\varepsilon_p, \tag{36}$$

$$r(\varepsilon_p) = Q(1 - \mathrm{e}^{-b\varepsilon_p}). \tag{37}$$

While isotropic hardening might be a satisfactory representation for some materials, a *kinematic hardening*, also called the *Bauschinger effect* [53] may take place. This means, that instead of expanding, the yield criterion moves in association with the applied stress beyond the plastic limit. If the direction of strain is reversed at some point after the plastic limit, the amount of reversed stress is $2\sigma_y$, see Fig. 14. Kinematic hardening is expressed through a kinematic hardening variable, x, which is a tensor in the stress space and relates to the movement of the yield criterion. For a uniaxial loading condition, the kinematic hardening exponent is,

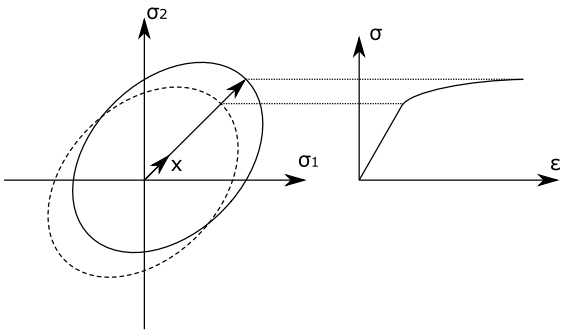

Figure 14: Kinematic hardening.

$$\mathrm{d}x = \frac{2}{3}c\mathrm{d}\varepsilon_p - \gamma x \mathrm{d}\varepsilon_p. \tag{38}$$

Where x is the stress above σ_y, c and γ are material constants. The uni-axial stress component is $^2/_3$ of the magnitude. Solving this equation gives,

$$\int \frac{\mathrm{d}x}{\mathrm{d}\varepsilon_p}\frac{1}{c-\gamma x}\mathrm{d}\varepsilon_p = \int \frac{c}{\gamma} - x\mathrm{d}\varepsilon_p \tag{39}$$

$$x = \frac{c}{\gamma}(1 - \mathrm{e}^{-\gamma\varepsilon_p}) \tag{40}$$

From Eq.(40) it is apparent that The hardening converges when reaching $\sigma_y + \frac{c}{\gamma}$.

Another possibility is to have both isotropic hardening and non-linear kinematic hardening. For this combination to be expressed Eq. (35) and (38) is combined. For a uni-axial loading, this results in,

$$\mathrm{d}\sigma = E(1 - \frac{E}{E + c - \gamma x + b(Q - r(\varepsilon_p))})\mathrm{d}\varepsilon \tag{41}$$

Defining the hardening as kinematic or isotropic has implications for the resulting *hysterisis loop* resulting from a tensile-compression cyclic loading condition.

Note that for some materials, the elastic strain is so small in comparison to the plastic strain that it is negligible, allowing for simplified graphical models. This can be expressed as,

$$when\, \varepsilon_p >> \varepsilon_e\,,\, \varepsilon = \varepsilon_p. \tag{42}$$

3.4 Requirements for a Yield Surface

Much of the early work on plasticity theory was done by Drucker [54]. Drucker contributed to the field of material science through, perhaps most famously, the *Normality Flow Rule*. Its implications on plasticity theorems and work-hardening will be briefly introduced in this section. Drucker also established the Drucker-Prager Criterion, which is commonly used for estimating

at which stress state a Rock, or brittle material, reach it's ultimate strength [55]. The criterion will not be presented in this thesis.

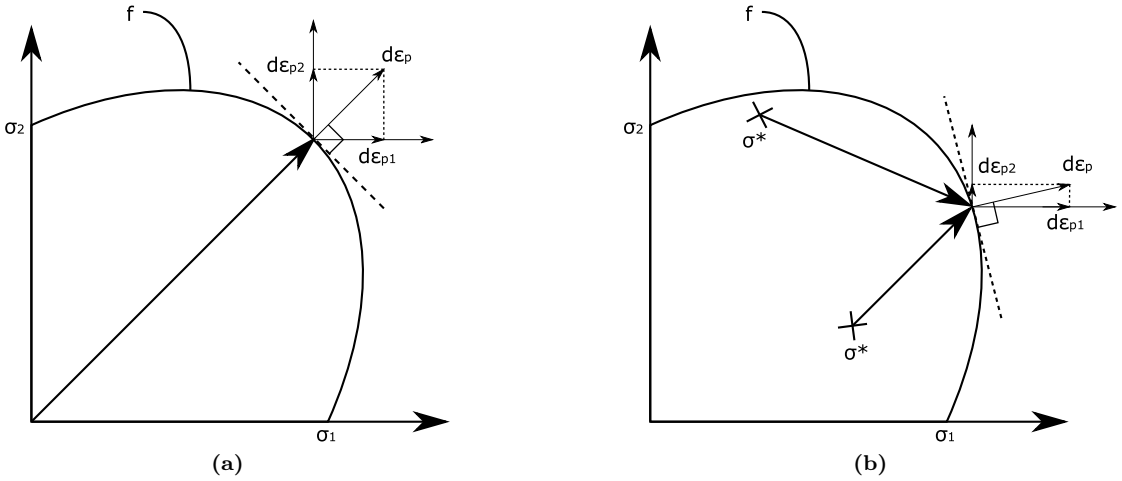

Figure 15: Example of plastic strain increment at yield surface. (a) biaxially loaded (b) arbitrarily loaded.

The normality flow rule regards the rate and mode of expansion of a yield surface when the stress state surpasses the yield criterion. Regardless of the initial loading case σ^* of a body, the direction of plastic strain increment at the yield surface is defined as proportional to the tangent of the yield surface. This is illustrated in Fig. 15 and mathematically described as,

$$\mathrm{d}\varepsilon_p = \mathrm{d}\lambda_f \frac{\partial f}{\partial \sigma} \tag{43}$$

Where f is the yield criterion, and λ_f is the magnitude of flow. Eq. (43) is an associated flow rule as long as it is associated to a defined yield criterion. An associated flow rule states that the Plastic potential (Φ) is equivalent to the yield surface, and so for the following discussion, $\Phi = f$. For the von Mises criterion where $\sigma_3 = 0$ the direction of plastic flow is given as,

$$\frac{\partial f}{\partial \sigma} = \frac{1}{2}(\sigma_1^2 - \sigma_1\sigma_2 + \sigma_1^2)^{-\frac{1}{2}}(2\sigma_1 - \sigma_2) \tag{44}$$

Drucker's postulate states that [54],

$$\mathrm{d}\sigma\mathrm{d}\varepsilon = \mathrm{d}\sigma(\mathrm{d}\varepsilon_e + \mathrm{d}\varepsilon_p), \tag{45}$$

is the work applied to a loaded body. And such,

$$\mathrm{d}\sigma_{ij}\mathrm{d}\varepsilon_{p\,ij} \geq 0 \tag{46}$$

Eq. (46) is known as Drucker's Inequality and can be interpreted as a requirement that the plastic strain rate may never oppose the the stress rate in work hardening materials. For work

softening, which is the decreasing stress upon further strain (see Fig. 11), the case is different. Plastic flow of material softening, will not be examined here. Druckers postulate gives,

$$(\sigma_{ij} - \sigma^*_{ij})\mathrm{d}\varepsilon^p_{ij} \geq 0, \tag{47}$$

which is the value of the plastic dissipation. This is equivalent to,

$$|\sigma_{ij} - \sigma^*_{ij}||\mathrm{d}\varepsilon^p_{ij}| \cos\theta \geq 0, \tag{48}$$

requiring,

$$\theta = [90\,\mathrm{deg}\ to\ -90\,\mathrm{deg}]. \tag{49}$$

This can be considered as a proof that for a yield function to have a unique solution for a given point on the surface, the function must indeed be convex. A special case of this is non-smooth yield surfaces, such as the Tresca criterion. The Tresca criterion is not uniquely defined in its corners. This is overcome in numerical applications by smoothing the corners slightly. A smooth yield criterion, such as the von Mises criterion, can be considered better as it is always defined. Note that the requirement lies in the convexity of the yield surface, not the yield function [56]. A discussion of constitutive inequalities related to elastic and plastic materials are given by Hill in Refs. [57, 58].

The vector of the plastic flow further relates to the rate of which the yield surface expands (isotropic hardening), or moves (kinematic hardening). For the special case of biaxial loading depicted in Fig. 15a, we notice that an isotropic material will have its plastic strain increment continue in the same biaxial direction. For this case we have $\mathrm{d}\varepsilon_{p1} = \mathrm{d}\varepsilon_{p2}$.

Plasticity and hardening behavior of metals is a subject that is much more far-reaching than the short introduction found in these sections. For the sake of exploring the material models in Section 5, this brief introduction should serve as significant.

It should be emphasized one more time for clarity that, *yield stress*, (σ_y) is the onset of plasticity, a *yield surface*, (f) defines this point for multiaxial loading conditions, and is in principle a phenomenological concept. *Flow stress*, $(\bar{\sigma})$ is the stress causing deformation in the plastic regime, and the *plastic potential*, (Φ) is a mathematical concept which represents the direction and magnitude of flow, and can be considered equal to the yield surface through the associated flow rule.

3.5 Fracture

If a weakness is introduced to a member, the area around this weakness will inevitably act as a stress raiser, i.e., the area around this weakness will be subjected to more significant amounts of stress than the homogeneous material. In mechanical testing, a member is notched to achieve this stress localization. In actual engineering applications, the fracture may occur in sharp edges as a result of geometry, welds, cracks, or smaller weaknesses in the surface as a result of the manufacturing process.

A material can fracture either in a brittle or ductile manner. A brittle fracture has low amounts of plastic deformation and can happen rapidly. This is often related to a load applied at high

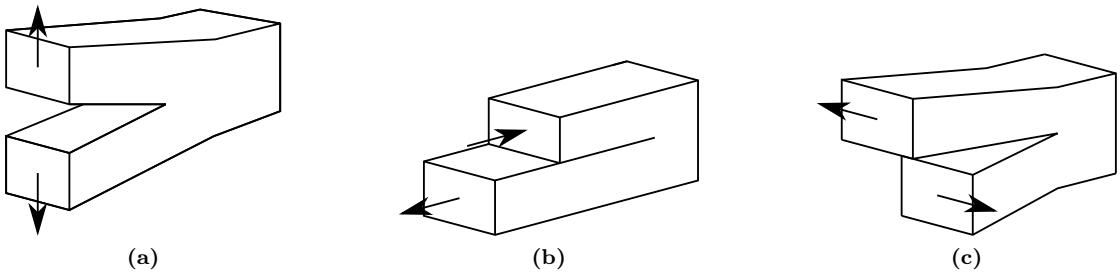

Figure 16: Three different modes of fracture. (a) Mode I, (b) Mode II and (c) Mode III

speed, brittle materials (e.g., ceramics, or low temperatures). A ductile fracture can happen more slowly and be accompanied by larger amounts of plastic deformations. It is common to differentiate fractures in three different modes. These are schematically illustrated in Fig. 16. For tensile stress applications, it is commonly assumed Mode I to be the governing fracture mechanic. Mode I is referred to as the opening mode. Mode II and III are governed by shear stresses and are not seen to occur as often as Mode I.

The crack geometry affects what amount of applied stress cause the member fails. An infinitely sharp crack, will serve as a singularity in the stress distribution, and result in infinite stress at the crack tip, which is not physically admissible as a stresses can exceed the yield limit. In real materials, however, a crack will always consist of a tip radius. A small tip will be more detrimental compared to a more rounded. In fracture mechanics, the severity of the crack is defined by the stress intensity factor K, which is expressed as [38],

$$K = Y\sigma\sqrt{\pi a}. \tag{50}$$

Where a represents the crack length and Y represents the geometry of the sample. A material will resist brittle fracture as long as the stress intensity factor in under the critical value of K_c. K_c represents the material's fracture toughness. The plane strain fracture toughness is commonly abbreviated as K_Ic. Plane strain fracture toughness is known to be sensitive to anisotropy as a result of microstructure. Grain growth direction and morphology affect crack growth in the way that a crack grows more quickly in the same plane as flattened grains. This leads to fracture toughness commonly needed to be tested in different directions.

For a sharp notch or crack, the stress is highest at the tip, and this region will yield first. When the area experiencing plasticity is relatively small, the crack growth is dominated by a more substantial area around the crack tip. If this is the case, Linear Elastic Fracture Mechanics (LEFM) is applicable, and simplified analytical/empirical models provide accurate estimations. With a larger plasticity zone, the fracture mechanics are more complex, and the use of LEFM may underestimate the severity of the crack.

3.6 Failure in Materials

The limit value UTS is the highest recorded value of stress in a tensile test. The point of UTS is commonly regarded as the onset of necking in ductile materials, and the point of ultimate failure in brittle materials. The common mechanisms of tensile failure are described in Fig. 17. After necking initiates, the cross-sectional area of a tensile specimen will reduce. For a pure material,

this reduction will last until the cross-sectional area reaches zero. However, in real materials, the nucleation of voids around inclusion particles, and void growth reduce the area more rapidly, and separation happens at an earlier stage. After necking initiates, the load-displacement curve will typically begin a downward slope. The stress has, in this case not been reduced, but the force needed to deform the specimen is less due to the dramatically reduced cross-sectional area. Correction methods such as the Bridgman correction can be used to evaluate the actual stress state in the necked region [40, Chapter 3].

The evolution of voids characterizes ductile fracture of specimens. The evolution may initiate at the center and eventually cause a shear slip in the circumference of the void formation, resulting in a cup-cone fracture surface. The void evolution is visible on the fracture surface of a specimen as small dimples. The dimples are commonly also associated with inclusion particles. Cleavage or intergranular fracture is common fracture mechanisms in more brittle materials; in these situations, voids are not allowed to form before a fracture finds its way through the material. Some multiphase materials will contain brittle second-phase materials along grain boundaries, and these may act as preferred paths for a fracture causing intergranular fracture [43].

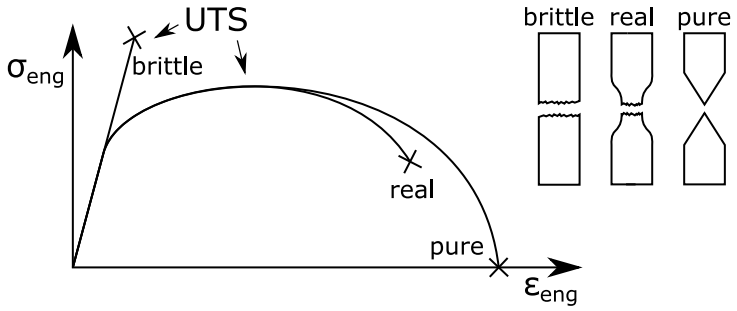

Figure 17: Tensile failure mechanisms.

4 Additively Manufactured Materials

A literature review on AM produced eutectic Al-Si alloys and 316L steel has been conducted. A summary of the common trends and fundamentals of these two materials are presented. Many of the trends are applicable to other materials commonly used in AM.

4.1 Aluminum-Silicon Alloys

Aluminium Silicon (Al-Si) alloys are among the most common aluminum alloys on the market [23], and its transition to AM is currently under development, with a seemingly increasing number of research papers concerning AM produced Al-Si alloys emerging over recent years. Improving the understanding of AM produced Al-Si may benefit industries such as automotive, aerospace, and aircraft primarily [12]. The Al-Si composition is beneficial due to silicon being completely solvable in liquid aluminum, the eutectic composition of Al-Si is at 12.6 wt%Si where the corresponding melting temperature is 577°C [59]. In AM, the most commonly investigated Aluminum silicon compositions are: the eutectic composition, (Al-12Si) [13, 17, 19, 21, 60–62], and the 10wt%Si version alloyed with small contents of magnesium (Al-10SiMg) [18, 27, 33, 34, 63–67]. Al-Si alloys are well suited for AM due to it's low melting temperature, leading the process to require lower laser powers than many other materials. The finished Al-Si build has a high strength to weight ratio, combined with high ductility [39]. A major challenge involved in AM of Al-Si alloys is the surface oxide film emerging naturally in aluminum, which can be difficult to avoid during SLM [12].

Aluminum is a typical ductile metal, while silicon is a typical brittle material [23]. Silicon precipitates in the Al-matrix result in the enhanced strength of Al-Si compared to pure Al. With casted Al-Si alloys, the Si usually forms in needlelike formations throughout the material [19, 23]. With AM produced Al-Si, there is observed a high concentration of silicon in the melt-pool borders, as well as a more uniform network of Si inside the melt pools [68]. Melt pool morphology in a as-built Al-Si10Mg alloy is schematically illustrated in Fig. 18, the build direction in this schematic is the Z-direction.

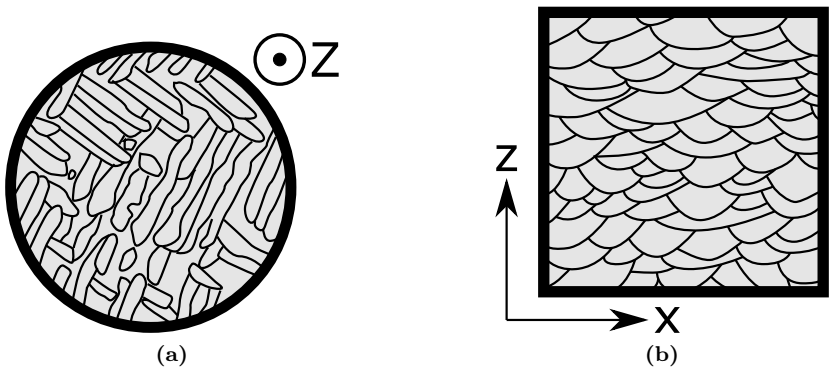

Figure 18: Schematic illustration of melt pool geometry in Al-Si10Mg built with SLM. (a) Above view and (b) side view. The sample is built with the axis perpendicular to the build-plate. Black lines signifies melt pool borders. The "fish-scale"-like geometry is caused by the semi-circular melt-pool. Adopted from [69].

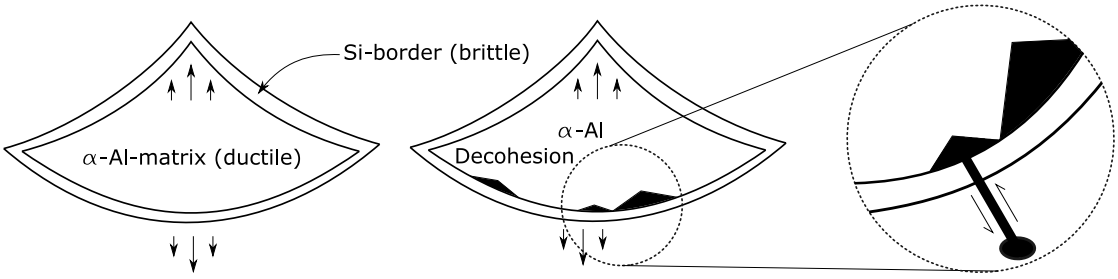

Figure 19: Schematic microstructure evolution during loading in Al-Si alloy produced by AM. Failure is suggested to occur at the border of residual melt pools in the material.

It is apparent that for Al-Si alloys produced by AM, the silicon borders around scan tracks may be a majorly influencing factor on the failure of the material [17, 19]. Melt pool borders may influence intergranular fracture, causing the crack propagation path to follow these borders. This behavior can be observed in both heat-treated and as-built specimens, even if the heat treatment makes the alloy more homogeneous, traces of scan tracks may still be present [19].

Plasticity starts in the ductile Al-matrix, but since Si-networks surround the matrix, one can expect the nucleation of voids as a result of debonding between the two phases. Eventually, these nucleated defects will coalesce and lead to fracture [17]. The effect is illustrated in Fig. 19. It is possible that this behavior is especially prominent in Al-Si due to the great difference in yield strength between the two alloying elements, 34 MPa for pure Al [70] and 165 MPa for Si [71].

Another influencing factor is that of porosities. The porosity content of AM produced Al-Si alloys varies throughout literature and is dependant on the parameters used in the printing process. Low porosity is desirable for achieving a homogeneous and strong material. Investigations regarding the effect of printing parameters and porosities in Al-Si10Mg show that porosity percentage can be modeled statistically through a response surface [65]. Read et al. [65] shows that the porosity percentage in AM produced Al-12Si can vary between the range of 29.9% porosity to 0.8%, for $P = 125$, $v = 1675$ and $P = 175$, $v = 1025$ respectively. The consensus found by investigating reports on porosities in Al-Si alloys is that the samples benefit from higher laser powers, and lower scanning speeds [12, 30, 65, 72]. However the effect becomes less significant after a certain point [65].

Porosities in Al-Si are found to have both spherical and crescent morphology; the morphology is suggested to depend on the interaction between successive melt pools, which is altered through laser power, scanning speed and hatch spacing. For a process with smaller melt pools, crescent or irregular morphology is suggested to be more common [62, 67]. With more crescent pores, one can expect a weaker material due to the possibly shorter crack evolution path [62, 73].

An extensive investigation on pore morphology in Al-Si10Mg by Maskery et al. [74] reveals that a majority of the pores have a diameter less than 50 µm. Still, there is a significantly uneven distribution of pore diameters, and smaller diameters are exponentially more frequent than larger. Further it is shown that only a small fraction of the observed pores may be classified as regular in shape, i.e., spherical. Elongated or irregular pores are seen to be more common than spherical [74]. This is likely due to pores not being the result of entrapment of gas, but rather keyhole porosities [30, 75]. Keyhole pores are significantly more common in samples built with low laser powers [22], and such the cause of these pores may be attributed to poorly melted powder, as the

power is not sufficient for achieving an evenly distributed melt. Heat treatment of Al-Si10Mg is shown to have a minimal effect of porosity content [74].

Suryawanshi et al. [17] considered SLM fabricated Al-12Si alloy with different types of laser movement and heat-treatments. Tensile, fatigue, and fracture properties are investigated. A primary result to be given attention is that the material produced by SLM is significantly more brittle than the casted equivalent, in fact, the ultimate tensile strength is increased by roughly 100 MPa, and the percent elongation at failure is reduced by strain percentages of 4.6 to 6.7 depending on the build orientation. With tests performed on specimens printed in different orientations, the anisotropy of AM produced Al-Si is present. While the variation in UTS is small, the ductility is more anisotropic. Specimens tested in the parallel direction experience more significant strains. I.e. Anisotropy is more significant in regards to strain than stress.

Prashant et al. [60] found that a Checkerboard Hatching style, as illustrated in Fig. 6d, during the manufacturing of Al-12Si provides higher yield strength and UTS (460 MPa), also with excellent ductility. In another study by Li et al. [39], Al-12Si produced through SLM is shown to achieve an ultra-fine microstructure, which is hard to achieve with traditional manufacturing methods. The high cooling rate is credited as the main factor contributing to this.

Heat treatment of Al-Si alloys produced by SLM increases the ductility at the cost of lower strength [19], providing a material whose properties are more similar to the cast alloy [17]. The microstructure promoting higher strength and lower ductility is homogenized [67]. Silicon particles in the Al matrix segregate to existing Si-particles, resulting in more extensive regions of pure Al, which is, of course, more ductile. The processes providing higher ductility during heat treatment is shown to stop after about two hours of heat treatment [39]. The effect on tensile properties regarding the temperature of heat-treatment is documented, showing that a more coarse microstructure appears with higher annealing temperatures [19]. Research conducted on heat treatment of Al-12Si produced through AM shows that the material can be tuned to inhabit a wide range of strength and ductility with appropriately altering its microstructure [19, 60]. The ability to alter the mechanical properties leads Al-12Si to be a versatile material that can be used for different applications.

For post-processing materials produced by AM Hot Isostatic Pressing (HIP) [76] may be a solution for reducing porosities. However, traces of the original pores may still be present, and high-temperature applications may affect the material such that pores are reopened [77]. HIP is shown to be an effective tool for closing pores in AM materials built using sub-optimal parameters, but surface connected pores may be left unaffected or worsened, leaving the possibility of residual pores still acting as stress raisers [78]. Furthermore, post-processing using HIP may alter the geometry of the part in question as well as adding further expenses related to the manufacturing. In a recent publication by Ngnekou et al. [34] T6 heat-treatment of AlSi10Mg is shown to increase fatigue resistance regardless of which orientation the specimen is printed in during AM.

The tensile properties found in a selection of studies concerning AM produced Al-12Si are summarized in Appendix B.

4.2 316L Steel

316L steel is an alloy of the main elements, iron, nickel, and chromium. It has excellent corrosion resistance and creep strength at elevated temperatures. Its applications range from biomedical implants to marine exterior [79]. Being one of the most used steels in the industry, it is of course also of great interest to improve AM of this material [80].

As previously described AM produced Al-Si alloys have high strengths, but sometimes less ductility than those processed by more traditional methods. AM produced 316L steel differentiates itself from other materials commonly used in AM in that it achieves high strength and elongation despite the defects induced by the manufacturing process [81]. The microstructure of AM produced 316L is characterized by solidified melt pool grains, which are also seen in Al-Si alloys (Fig. 18). Within these melt pools, randomly oriented, nano-sized needle-structures of the γ phase are observed [81–83]. The material is seen to be orientation dependant in the same fashion as Al-Si alloys, in that horizontal orientation provide higher strength than vertical [82]. Also similarly to Al-Si alloys, Laser power is the process parameter most influential on the strength of SLM produced 316L steel [84].

Lower laser powers combined with high scanning speeds are shown to induce significant porosities, and reduce the grain size in the build [85]. Porosities are mainly located between layers and attributed to a lack of fusion [86]. High scanning speeds effectively results in a decrease in melt-pool size, which cause an increase in porosity [32]. The porosity morphology is also seen to become more irregular and less spherical with lower laser powers, whereas the choice of scanning strategy is not shown to affect the amount of porosity significantly [81]. Even if the effect of scanning strategy is not as significant as laser power or scanning speed, a checkerboard scanning style such as that seen in Fig. 6d achieves fewer porosities than a single melt style, likely caused by the overlapping of scan tracks between successive layers [87]. On the topic of Checkerboard scanning in 316L steel, it is also observed that pores are distributed along the edge of each "island" on the Z-plane, while on the XY-plane pores are commonly aligned [88]. Voids in AM produced 316L steel are also thought to be associated with high residual stresses, which cause formation of cracks along melt pool boundaries, eventually leading to nucleating voids [84].

With optimal process parameters, the amount of porosity in AM produced 316L steel can be reduced to a very small volume fraction [84]. 0.61% porosity is achieved in one study [81], where the higher density naturally also improves the strength of the material. The mechanical properties of AM produced 316L with ideal process parameters are seen to be superior to that produced by more traditional methods [84]. With proper printing parameters, tensile tests of 316L can reach elongation of 30%, and yield stress can be improved by a significant amount, compared to its traditionally manufactured counterpart [89].

HIP treatment of AM 316L is shown to be effective in improving fatigue life [89], attributed to increased bonding between layers resulting from the HIP process as well as the closing of voids. The effect of heat-treatment on mechanical properties of SLM produced 316L steel is less documented throughout the literature. Kong et al. [90] investigated the microstructural effects of heat-treatment and found that heat treatment at 1050°C caused an increase in grain size, as well as improved corrosion resistance. Montero et al. [91] found that heat treatment at higher temperatures decreases the yield strength while improving elongation slightly. The dimpled structure in the fracture surface was also altered with heat-treated samples compared to as-built. The dimples became shallower and broader, attributed to lower toughness as opposed to the as-built and lower temperature heat treatments.

5 Material Models, A Review

Material models or Damage models are used for numerical analysis of material deformation in modeled structures. Numerous options for material modeling are available in numerical software (FEA). Some of the available, and not yet available, models will be presented in the following sections. Some of the presented models are not suited for applications in FEA, but are theoretical, and delevoped for prediction of properties without the need for FEA. The models are empirical or semi-analytical. Empirical, meaning that the model is based on fitting a curve or function to data from experimental results, through defining constants that are, in isolation, just numbers unrelated to any real physical attribute of the material. Semi-analytical, meaning that portions of the model are rooted in physical phenomena determining the deformation behavior of the material. All models involve constants that need to be identified, the accuracy of the defined constants are invaluable to the accuracy of the simulation [92, 93]. After having defined constants for a given material, a simulation can be utilized to evaluate or generate optimal designs for the application in question.

In this section, models are presented in the order,

- Some ways of expressing the flow stress $\bar{\sigma}$.
- Hill's yield surfaces for anisotropic materials.
- Defect based models for plastic potential.
- A miscellaneous selection of material models.

However, they should not require that the reader inspects them in order. A summary found in Section 6 discusses what may be the most appropriate model to be incorporated as a constitutive model for the characterization and prediction of mechanical behavior in AM produced materials.

5.1 Ramberg-Osgood Relationship

The Ramberg-Osgood relationship [94] is one of the simplest ways to express the resulting stress-strain relationship from a uniaxial tensile test [43, Chapter 3]. The expression reads,

$$\varepsilon = \frac{\sigma}{E} + B\left(\frac{\sigma}{E}\right)^n \tag{51}$$

This equation serves as a natural starting point due to it's simplicity. The equation has been widely adopted for fracture mechanics analysis of isotropic materials [95]. It's limitations lie in that no fracture criterion is defined, and that softening is not an option. It's strength is in the ability to model plastic behavior in FEA through relative ease. Many of the following models assume a similar type of power law hardening, but are indeed more complex than Eq. (51).

5.2 Johnson-Cook

The plasticity model known as Johnson-Cook (JC) was first presented in 1985 [96]. The model is purely empirical and based on experimental results. Due to its simplicity, the model has been widely adopted into FEA. Abaqus [97] enables the user to model plasticity by entering the

necessary JC parameters in the material definition, reducing the need for tabulated values. The JC-model is expressed as,

$$\bar{\sigma} = [A + B\varepsilon_p^n][1 + C\ln\dot{\varepsilon}^*][1 - T^{*m}]. \tag{52}$$

Evidently 5 material parameters are needed for this model, A, B, n, C, m. ε_p is plastic strain, $\dot{\varepsilon}^* = {}^{\dot{\varepsilon}}/_{\dot{\varepsilon}_0}$, is the dimensionless plastic strain rate with $\dot{\varepsilon}_0$ being the reference strain rate. T^* is the homologous temperature in kelvin,

$$T^* = \frac{T - T_r}{T_m - T_r}. \tag{53}$$

In Eq. (53) T is the active temperature, T_r is room temperature and T_m is the melting temperature. Eq. (52) enables taking into account isotropic hardening, kinematic hardening, temperature variation and variation in yield strength [98]. The three parts of Eq. (52) can be duped as *Elasto Plastic term*, *Viscosoty term* and *Thermal Softening term* respectively [99]. The model is well suited for modelling rate dependant large deformations and temperature dependant applications.

Through inspection, it is clear that the parameter A is related to the yield stress when $\varepsilon_p = 0$. The value of the offset yield stress is appropriate to assume, $A = \sigma_y$. The exponent m relates to the material's thermal softening and can be obtained if the onset of plasticity, σ_y is known for two different active temperatures, T_1 and T_2. If the onset of yield is hard to define, the 0.2 offset yield strength can be utilized.

B and n relates to the material's hardening and can be determined through tests where strain rates are low. That is, $\dot{\varepsilon}^* \approx 1$ resulting in the Viscosity term being equal to 1.

$$\bar{\sigma} = [A + B\varepsilon_p^n][1][1 - T^{*m}] \tag{54}$$

Then for two stresses and strains at the same temperature, $1 - T^{*m} = k$, one can determine B and n.

$$\begin{aligned} B &= \frac{{}^{\sigma_1}/_k - A}{\varepsilon_1^n}, \\ n &= \frac{\ln\left(\frac{\sigma_2 - Ak}{\sigma_1 - Ak}\right)}{\ln\left({}^{\varepsilon_2}/_{\varepsilon_1}\right)} \end{aligned} \tag{55}$$

Finally, C, related to the material's kinematic hardening, is determined in the same fashion as seen in Eq. (55) through tests with two different strain rates.

$$C = \frac{\frac{\sigma_2}{\sigma_1 - 1}}{\ln\left({}^{\dot{\varepsilon}_2}/_{\dot{\varepsilon}_2}\right)} - \sigma_2 \ln\left(\frac{{}^{\dot{\varepsilon}_2}/_{\dot{\varepsilon}_2}}{\sigma_1}\right) \tag{56}$$

The JC model is usually suitable for applications concerning high strain rates but is reported to underestimate stress for lower strain rates [100]. Terms in the JC-model can be removed in order to simplify further, say the temperature is not a parameter of interest, then the Thermal Softening term may be ignored. e.g., in a room temperature tensile test, a material will usually

neck before any adiabatic heat is exerted from the material [101], leaving the Thermal softening term redundant. The JC model in its original form assumes strain, strain rate, and temperature as mutually independent [102], causing non-ideal results in some situations.

5.3 Zerilli-Armstrong

Zerilli and Armstrong [103] presented a dislocation based constitutive relation which sought to further the capabilities of the JC model. The relation is, in contrast to JC, to some degree based on actual physical phenomenons. As Face Centered Cubic (FCC) and Body Centered Cubic (BCC) materials behave differently when stressed, two separate equations are presented. For FCC metals the Zerilli-Armstrong (ZA)-model reads,

$$\bar{\sigma} = \sigma_y + C_2 \varepsilon^{\frac{1}{2}} \mathrm{e}^{(-C_3 T + C_4 T \ln \dot{\varepsilon})}, \tag{57}$$

and for BCC metals,

$$\bar{\sigma} = \sigma_y + C_1 \mathrm{e}^{(-C_3 T + C_4 T \ln \dot{\varepsilon})} + C_5 \varepsilon^n \tag{58}$$

The background for this in the original literature is that BCC metals, (e.g., iron), have a stronger dependence on temperature and strain rate regarding yield stress. The simplification of writing the equation without strain is the consequence. FCC metals, (e.g., aluminum and copper), have a more considerable dependence on strain as the controlling deformation mechanism is considered the intersection of dislocations.

The ZA-model is incorporated in the FEA software Ansys [104]. Modifications to the original formulation has been proposed by numerous papers [102, 105–108].

5.4 Modified Johnson-Cook

Lin et al. [107, 109] combined JC and ZA for a model that incorporates coupled effects of strain rate-temperature-strain, i.e., the terms are not mutually independent. The formulation was presented in two separate forms. The power-law form,

$$\bar{\sigma} = (A_1 + B_1 \varepsilon^n) \mathrm{e}^{(-C_2 T + C_3 T \ln \dot{\varepsilon})}, \tag{59}$$

and the polynomial form,

$$\bar{\sigma} = (A_1 + B_1 \varepsilon + B_2 \varepsilon^2)(1 + C_1 \ln \dot{\varepsilon}) \mathrm{e}^{[(\lambda_1 + \lambda_2 \ln \dot{\varepsilon})(T - T_r)]}. \tag{60}$$

For details on the development of these equations the reader is referred to the original literature [107, 109]. The nomenclature is the same as that of the JC and ZA formulations. $A_1, B_1, C_1, C_2, C_3, \lambda_1, \lambda_2$ being constants. In a comparative study by He et al. [93] Eq. (60) is shown to improve the accuracy of strain rate dependence modeling significantly compared to both JC and ZA models.

5.5 Quadratic Hill Criterion

Hill has established three different yield criterions for anisotropic materials [110–112]. The first being an extension of the von Mises criterion, described in Eq. (27), in a quadratic form. This is known as *the quadratic Hill yield criterion*, and is expressed as,

$$\Phi(\sigma_{ij}) = F(\sigma_{22}-\sigma_{33})^2 + G(\sigma_{33}-\sigma_{11})^2 + H(\sigma_{11}-\sigma_{22})^2 + 2L\sigma_{23}^2 + 2M\sigma_{31}^2 + 2N\sigma_{12}^2 = \sigma_y^2. \quad (61)$$

Anisotropy is present if the material behavior is different in different directions. For a simple investigation into anisotropy, one can explore the yield strength in the three principal directions. However, as noted by Hill [110], the anisotropy is a microstructure dependant property, and such its behavior will vary from point to point in the material. In Eq. (61) F, G, H, L, M, N characterize the current state of anisotropy.

The constants for the principal stress portion are,

$$\begin{aligned} F &= \frac{1}{2}\left[\frac{1}{(\sigma_{y\,22})^2} + \frac{1}{(\sigma_{y\,33})^2} - \frac{1}{(\sigma_{y\,11})^2}\right], \\ G &= \frac{1}{2}\left[\frac{1}{(\sigma_{y\,33})^2} + \frac{1}{(\sigma_{y\,11})^2} - \frac{1}{(\sigma_{y\,22})^2}\right], \\ H &= \frac{1}{2}\left[\frac{1}{(\sigma_{y\,11})^2} + \frac{1}{(\sigma_{y\,22})^2} - \frac{1}{(\sigma_{y\,33})^2}\right]. \end{aligned} \quad (62)$$

For the shear stress constants, the constants are,

$$L = \frac{1}{2\sigma_{y\,23}^2},\ M = \frac{1}{2\sigma_{y\,31}^2},\ N = \frac{1}{2\sigma_{y\,12}^2}. \quad (63)$$

For the case in which the principal stress coincide with an axis of symmetry, i.e., the plane perpendicular to the loading has isotropic properties, Eq. (61) simplifies to [40],

$$(\sigma_2 2 - \sigma_3 3)^2 + (\sigma_3 3 - \sigma_1 1)^2 + R(\sigma_1 1 - \sigma_2 2)^2 = (R+1)\sigma_y \quad (64)$$

Where σ_y would be the yield stress of uniaxial tension. The constants in Hill's yield criterion should ideally be history-dependent, and be represented as a function of strain to capture a realistic anisotropic behavior accurately. Still valuing these as constants are also seen to provide accurate results. An identification procedure for anisotropic constants are found in Refs. [113, 114]

5.6 Generalized Hill Criterion

The second Hill criterion allows for an exponent m providing a non-quadratic option [111]. The background is that Eq. (61), often overestimates the effect of the constants, (or R in Eq. (64)). The modified equation is then,

$$\Phi(\sigma_{ij}) = F(\sigma_{22}-\sigma_{33})^m + G(\sigma_{33}-\sigma_{11})^m + H(\sigma_{11}-\sigma_{22})^m + 2L\sigma_{23}^m + 2M\sigma_{31}^m + 2N\sigma_{12}^m = \bar{\sigma}^2 \quad (65)$$

m can be much higher than 2, experimental results suggests $m \geq 6$ for many materials [40].

5.7 Hill's 1993 Criterion

The third Hill criterion [112] concerns plasticity in rolled sheet metals. That is, two principal stress directions are considered for a surface. The direction of rolling sheet metals induces anisotropic properties, as the grains are elongated in the rolling direction. The strength is then usually greatest in this direction [115, Chapter 9.4.3].

The Hill 1993 yield criterion is rather simple and user-friendly with only two material constants needed to be defined (in addition to directional yield stress). Hill makes use of constants, r_0 and r_{90} as the ratios of the transverse/through-thickness increments of logarithmic strain to establish a model for plastic response. σ_0 and σ_{90} are the yield stresses in its corresponding subscript direction. For uni-axial tension the ratio of incremental strain is,

$$\frac{\mathrm{d}\varepsilon_1}{\mathrm{d}\varepsilon_2} = -\frac{\mathrm{d}\sigma_2}{\mathrm{d}\sigma_1}, \quad (66)$$

$$\begin{aligned} \frac{r_0}{1+r_0} &= -\frac{\mathrm{d}\sigma_1}{\mathrm{d}\sigma_2}\, for\, \sigma = (\sigma_1, 0), \\ \frac{r_{90}}{1+r_{90}} &= -\frac{\mathrm{d}\sigma_1}{\mathrm{d}\sigma_2}\, for\, \sigma = (0, \sigma_2). \end{aligned} \quad (67)$$

The inverse tangent of these equations gives the angle of the loci relative to coordinate axes. The equation is thus given as,

$$\begin{aligned} \frac{r_0}{1+r_0} &= \tan\psi\, for\, \sigma = (\sigma_1, 0), \\ \frac{r_{90}}{1+r_{90}} &= \tan\psi\, for\, \sigma = (0, \sigma_2). \end{aligned} \quad (68)$$

The proposed yield function is then for uniaxial case where $\sigma_u = \sigma_0 = \sigma_{90}$,

$$\sigma_1^2 - \left(2 - \frac{\sigma_u^2}{\sigma_y^2}\right)\sigma_1\sigma_2 + \sigma_2^2 + \left[(p_h + q_h) - \frac{(p_h\sigma_1 + q_h\sigma_2)}{\sigma_b}\right]\sigma_1\sigma_2 = \sigma_u^2. \quad (69)$$

Where σ_b is the stress of the biaxial loading case. Transforming this to the case where $\sigma_0 \neq \sigma_{90}$,

$$\frac{\sigma_1^2}{\sigma_0^2} - \frac{c\sigma_1\sigma_2}{\sigma_0\sigma_{90}} + \frac{\sigma_2^2}{\sigma_{90}^2} + \left[(p_h + q_h) - \frac{(p_h\sigma_1 + q_h\sigma_2)}{\sigma_y}\right]\frac{\sigma_1\sigma_2}{\sigma_0\sigma_{90}} = 1. \quad (70)$$

Where p_h and q_h are constants, which can be positive or negative. Moreover, c may be expressed through,

$$\frac{c}{\sigma_0 \sigma_{90}} = \frac{1}{\sigma_0^2} + \frac{1}{\sigma_{90}^2} - \frac{1}{\sigma_b^2}. \tag{71}$$

What is ultimately achieved through these equations is a yield criterion in which the loci may be shifted to accommodate for the different yield strengths in the 1 and 2 direction. This locus can be exemplified as in Fig. 20.

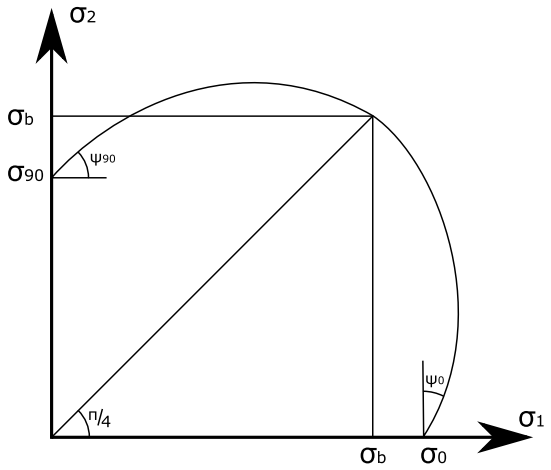

Figure 20: Hill's 1993 yield criterion.

5.8 Gurson and Modified Gurson (GTN)

The material model known as Gurson investigates the plastic flow of a porous material [43, Chapter 5]. Gurson [116] is an upper bound theorem, solved by analyzing deformation velocity fields in a material containing porosity, which evolves during plastic strain, such that it satisfies the boundary condition and strain rate conditions. Gurson originally considered an isolated void of spherical nature in a homogeneous, incompressible, rigid-plastic material obeying the von Mises criterion with a defined yield strength σ_y [117]. A flow potential for void growth in a plastic material was developed [116]. The plastic potential or yield surface is given as [116],

$$\Phi = \frac{\sigma_{eq}^2}{\sigma_y} + 2f\cosh\left(\frac{3\sigma_h}{2\sigma_y}\right) - 1 - f^2 = 0 \tag{72}$$

Gurson [116] first presented the model in 1977. The model was generalized by Tvergaard, Chu, and Needleman [118–120] where further material constants and a failure criterion was incorporated. The model considers three void mechanics as a result of loading, namely, (i) void growth, (ii) void nucleation, and (iii) void coalescence. Its now conventional form known as "Modified Gurson", GTN model, or "Porous Metal Plasticity" [97], is defined as,

$$\Phi = \frac{\sigma_{eq}^2}{\bar{\sigma}^2} + 2q_1 f^* \cosh\left(\frac{3q_2\sigma_h}{2\bar{\sigma}}\right) - 1 - (q_3 f^*)^2 = 0. \tag{73}$$

Here, f^* is Void Volume Fraction (VVF), $\sigma_h = \frac{1}{3}\sigma_{kk}$ is the hydrostatic stress, σ_{eq} is the equivalent von Mises stress, $\bar{\sigma}$ is the flow stress of the matrix material, which can be in any arbitrary form, for example, the second term of the Ramberg-Osgood Relationship Eq.(51). q_1, q_2, and q_3 are material constants, commonly $q_3 = q_1^2$ is used. [121]. The original postulation is achieved through setting these parameters as unity. With the GTN model the elevated stress resulting from voids are averaged throughout the material, and thus the material is considered continuous [43].

The behavior of porosities in the material is assumed such that the original VVF (f_0) is known. VVF increases with plastic deformation and its rate of increase is a result of the growth of existing voids as well as the nucleation of voids (Fig. 21). The change in VVF is,

$$\dot{f} = \dot{f}_{growth} + \dot{f}_{nucleation}. \tag{74}$$

When the VVF reaches a critical point, f_c, the stress carrying capacity decreases drastically. This drastic decrease in strength is modeled by altering f^* in Eq.(73). This point can be considered the onset of void coalescence, which is known to occur in the latter period of necking [40]. The ultimate VVF at failure is f_f. The evolution in VVF is thus expressed as,

$$f^* = \begin{cases} f & \text{if } f \leq f_c \\ f_c + \frac{(1/q_1)-f_c}{f_f-f_c}(f-f_c) & \text{if } f_c < f < f_f \end{cases} \tag{75}$$

The evolution of f due to void growth is not a particularly complex parameter to determine. It can be seen as the amount of non-porous volume fraction times the double dot product of macroscopic plastic strain with the unit matrix, i.e., the sum of the diagonal in the plastic strain,

$$\dot{f}_{growth} = (1-f)\dot{\varepsilon}_p : I = (1-f)\dot{\varepsilon}_{p\,kk}. \tag{76}$$

The evolution of void nucleation, on the other hand, is a more complicated process. Chu and Needleman suggested a statistical approach for this feature [122],

$$\dot{f}_{nucleation} = A\dot{\varepsilon_p} = \frac{f_N}{S_N\sqrt{2\pi}} \mathrm{e}^{-\frac{1}{2}(\frac{\varepsilon_p-\varepsilon_N}{S_N})^2}\,\dot{\varepsilon}_p. \tag{77}$$

Where S_N and ε_N are standard deviation and mean value of plastic strain. Tvergaard and Needleman suggested these to typically be fixed as $S_N = 0.1$ and $\varepsilon_N = 0.3$ [120]. While Eq.(77) shows the strain controlled $f_{nucleation}$, it can also be expressed as stress-controlled. The GTN model also contains a failure criterion. When the VVF reaches the failure value, f_f, ductile fracture occurs [43].

The equations involved in the GTN model have now been presented, and thus in total, the GTN model is expressed through a total of 10 parameters, in addition to an expression for the flow stress $\bar{\sigma}$ of the matrix material.

$$\phi = \phi(\sigma_y, \varepsilon_y, q1, q2, f_0, f_c, f_f, f_n, \varepsilon_N, S_N). \tag{78}$$

With all these parameters established, a yield criterion is defined with Eq.(73) equaling zero. This criterion can be further expanded to account for kinematic hardening behavior [123], ductile

fracture [124], and shear failure [125]. Some extensions of the GTN model that account for anisotropic behavior is presented in the following sections.

5.9 Rousselier Model

Rousselier [126, 127] developed a model for ductile damage in porous metal plasticity. The development of the model is, contrary to the GTN model, not developed by considering any form of geometric scenario. It is rather described using thermodynamics and potentials The basis of the rousselier model lies in four main hypothesis: H1, the Principle of simplicity, the simplest possible configuration is the chosen one. H2, The material is isotropic. H3, The energy potential is expressed through external factors (deformation ϵ^e) and internal factors, the internal factors are further divided into a hardening variable p^i and a damage variable, B^i. This means the energy potential should be expressed as,

$$\phi = \phi_e(\varepsilon^e) + \phi_p(p^i) + \phi_B(\beta^i). \tag{79}$$

The fourth hypothesis, H4, reads that the plastic potential should be,

$$F = F_1(\sigma_{eq}, P) + F_2(\sigma_h, B). \tag{80}$$

Where,

$$F_1 = \sigma_{eq} + P(p^i), \tag{81}$$

$$F_2 = B(\beta^i)g(\sigma_h). \tag{82}$$

Here $P(p^i)$ represents the function of the potential due on the internal variables and $B(\beta^i)$ due to damage. For further expansion of these hypothesizes, the reader is referred to the original literature [127]. Following relatively few steps, Rousselier arrives at a point in which parts of the equation is analogous to that of Rice and Tracey's [128] approximation for the growth of a single spherical void,

$$\frac{\dot{R}}{R} = 0.283\dot{\varepsilon}_p \mathrm{e}^{3\sigma_h/2\sigma_y}. \tag{83}$$

Where R is the void radius, $\dot{R}$ its derivative, and $\dot{\varepsilon}_p$ is the plastic strain rate. By assuming,

$$\frac{\dot{R}}{R} = \frac{1}{3}\beta^i \varepsilon_p \mathrm{e}^{\sigma_h/p^i\sigma_y}. \tag{84}$$

The equation for the yield surface and plastic potential due to Rousselier is thus defined as,

$$\Phi = \frac{\sigma_{eq}}{1-f} + Df\sigma_k \mathrm{e}^{\frac{\sigma_h}{\sigma_k(1-f)}} - \bar{\sigma} = 0. \tag{85}$$

Where D and σ_k are parameters. f is, as in the GTN model, VVF with the initial value of f_0. D is suggested to be between 1.5 and 2. σ_k affects the point at failure and can be assumed through comparison with experimental results.

The model has two constants that need defining, neglecting eventual variables within the expression for f.

5.10 Hammi and Horstemeyer's Void Based Damage Model

Hammi and Horstemeyer [129] developed an anisotropic tensorial based model which is in some ways similar to the GTN model.

As mentioned, the three main mechanisms of voids in a porous medium is that of void growth, nucleation, and coalescence. The coalescence of voids may happen in two ways, either dominated by a strain localization between voids ("void sheet mechanism") or that voids grow into each other ("natural void growth") [118, 129], see Fig. 21. Note that all these mechanisms may occur simultaneously but at different rates. A note here is that smaller voids are shown to grow more rapidly [130]. Note also that with a given material one mechanism of coalescence is usually preferred [129].

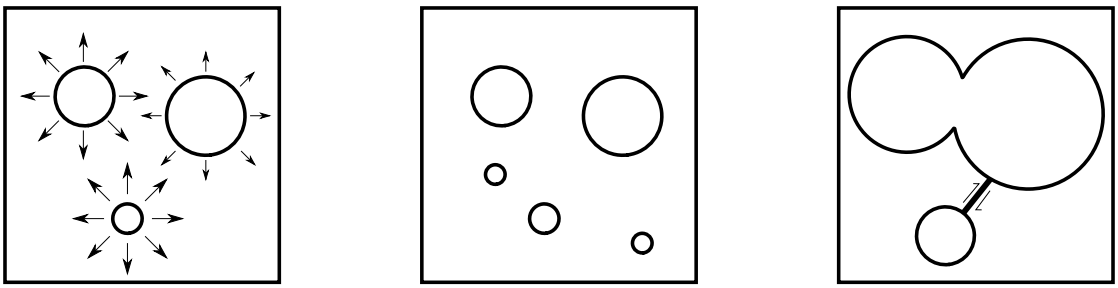

Figure 21: Void behavior during loading. (a) growth, (b) nucleation, (c) coalescense of voids with natural growth and sheet mechanism.

The purpose of an anisotropic representation lies in the fact that void morphology or orientation may be a significant factor in inducing anisotropic behavior. While the voids in Fig. 21 are represented as spheres, an elliptical shape favoring one orientation is commonly observed, and often dependant on the manufacturing process. The matrix material itself may also have anisotropy, which is non-negligible and must indeed be accounted for in a model for accurate predictions to be made.

The total damage model presented in Ref. [129] is as follows,

$$\dot{\boldsymbol{\phi}} = \dot{\boldsymbol{\eta}} + \dot{v}\boldsymbol{I} + \dot{\boldsymbol{c}}. \tag{86}$$

Where $\dot{\boldsymbol{\phi}} = 0$ denominates the undamaged material and $\dot{\boldsymbol{\phi}} = 1$ corresponds to total failure. In Eq.(86) $\dot{\boldsymbol{\eta}}$ is the function for void nucleation rate, $\dot{\boldsymbol{v}}$ is void growth rate and $\dot{\boldsymbol{c}}$ is a coalescence evolution. For the derivation of these equations the reader is referred to the original source [129]. The damage tensor $\boldsymbol{\phi}$ is written in six independent components. Void nucleation and coalescence

follow anisotropic evolution while growth is assumed isotropic. The total damage rate is written as,

$$\dot{\boldsymbol{\phi}} = \dot{\boldsymbol{\phi}}_{\boldsymbol{\eta}} + \dot{\boldsymbol{\phi}}_{\boldsymbol{v}} + \dot{\boldsymbol{\phi}}_{\boldsymbol{c}} \tag{87}$$

Where $\dot{\boldsymbol{\phi}}_{\boldsymbol{\eta}}$, $\dot{\boldsymbol{\phi}}_{\boldsymbol{v}}$ and $\dot{\boldsymbol{\phi}}_{\boldsymbol{c}}$ are damage rate due to void nucleation, growth and coalescence respectively. Each of these are seen to occur simultaneously, and the total damage in its expanded form is expressed as,

$$\begin{aligned} \dot{\boldsymbol{\phi}} = \dot{\lambda}_p \frac{d^{1/2} f_N}{K_{IC}} f_0^{1/3} \left[\frac{Y^*}{S_{ntemp}}\right]^{S_N} \boldsymbol{P} : \left|\frac{\mathrm{d}\varepsilon_p}{\mathrm{d}\lambda}\right| \\ +\dot{\lambda}_p a_v \langle \phi_h - \phi_c \rangle \exp\left[\frac{3\langle\sigma_h\rangle}{2\sigma_{eq}}\right] \frac{1}{(1-\phi_h)^m} \boldsymbol{I} + \dot{\lambda}_p \left[\frac{Y^*}{S_c}\right]^{S_c} \boldsymbol{Q} : \left|\frac{\mathrm{d}\varepsilon_p}{\mathrm{d}\lambda}\right| \end{aligned} \tag{88}$$

Here $\dot{\lambda}_p$ is the Lagrange multiplier, S_{Ntemp} refers to temperature dependant ductility, K_{IC} is the material fracture toughness, f_N is related to void nucleating particles. The model builds on the work of several classical void evolution formulations, including Gurson [116] and Rice and Tracey [128]. The model achieves a good fit with experimental results, with mostly experimentally identifiable parameters, in addition to only a few material constants.

5.11 Nagaki's Anisotropic Damage model

Nagaki et al. [131, 132] presented a damage model for anisotropic materials, which incorporates into the GTN-model. The anisotropy is achieved by expressing variable spacing of voids along each coordinate axis, as well as void morphology in terms of an ellipsoid. The model can account for ellipsoidal voids by expressing the volume fraction as in Fig. 22. The area of the ellipse in Fig. 22b is expressed as,

$$A_{ellipse} = \frac{\pi a_i a_j}{4}. \tag{89}$$

The reduced area is represented in damage tensors,

$$\boldsymbol{\Omega}_{\boldsymbol{k}} = \frac{\pi a_i a_j}{4 L_i L_j} \tag{90}$$

Where $k = [1, 2, 3]$, $i = [2, 3, 1]$ and $j = [3, 1, 2]$. This tensor relates to a damage effect given by,

$$\boldsymbol{\Phi} = (1 - c\boldsymbol{\Omega})^{-1}. \tag{91}$$

The scalar parameter c is a constant which may be used to represent the effect of stress concentration, but can in principle be valued as unity. The new stress tensor for the voided material is then,

$$\boldsymbol{S} = \frac{1}{2}(\boldsymbol{\sigma\Phi} + \boldsymbol{\Phi\sigma}). \tag{92}$$

For a simplified investigation of the equations, Nagaki et al. [131] assume a plate ($\sigma_3 = 0$) with even hole distribution in two directions, distance between holes in the 1, and 2-direction are L_1 and L_2. Each hole is circular with a diameter d. Substituting the Cauchy stress in Gursons original postulation in Eq. (72), for the new stress tensor, $\boldsymbol{S}$. The combination of equivalent stress σ_{eq} and hydrostatic stress σ_h is,

$$\sigma_{eq}^2 = S_{eq}^2 = (\sigma_1 \boldsymbol{phi}_1)^2 - \sigma_1\sigma_2\boldsymbol{\Phi}_1\boldsymbol{\Phi}_2 + (\sigma_2\boldsymbol{\phi}_2)^2. \tag{93}$$

$$\sigma_h = \boldsymbol{S}_h = \frac{\sigma_1\boldsymbol{\Phi}_1 + \sigma_2\boldsymbol{\Phi}_2}{3} \tag{94}$$

What is achieved is a formulation of the Gurson model, where the difference between spacing in voids alters the angle of the yield loci. The effect is such that a tighter spacing of holes in the 1 direction rotates the loci toward the 1 axis, making the material stronger in this direction compared to 2. This function effectively allows for anisotropic representation through a simple altering of the equivalent stress equation. The model has been compared to FEA results in Ref. [132], and shows good agreement in regards to a biaxially stretched porous plate, but not as well with a uniaxially stretched porous solid.

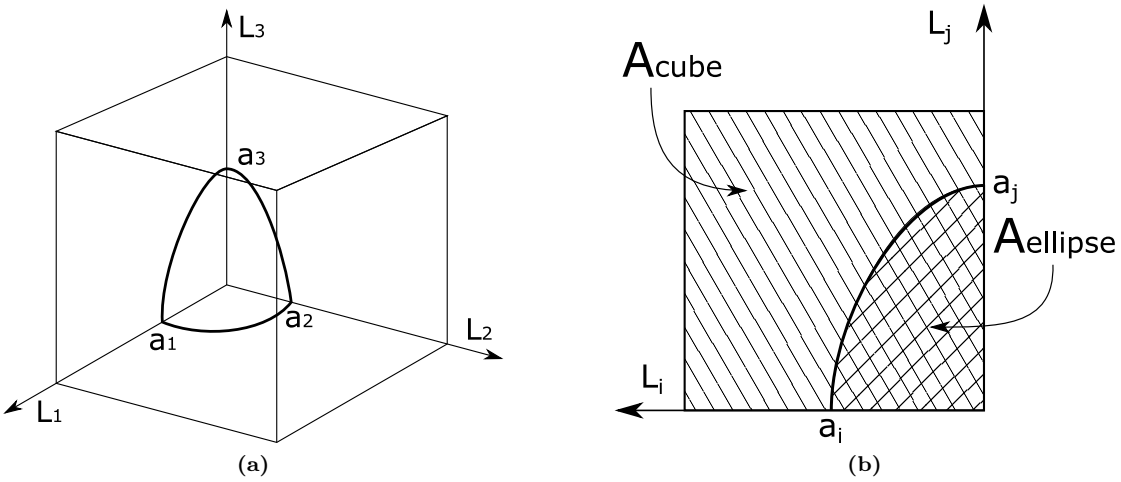

Figure 22: Assumption for unit cube in Ref. [131]. Damage is represented not only with VVF, but also size and distribution of voids.

5.12 GTN-Hill Model

An anisotropic material model, which accounts for void behavior, is achieved through combining the GTN model and Hill's quadratic anisotropic potential [110]. GTN assumes isotropy of the

plastic material, to alter the GTN model to account for anisotropy one approach is to apply Hill's expression for equivalent stress, as seen in Eq. (61), as σ_{eq} in Eq. (73).

Kami et al. [133] applied the combination to predict fracture of metallic sheets. The anisotropic expression provides accurate results when compared to the modeled experiment, in terms of fracture mode and Force-Displacement relationship. Chen and Dong [134] compared the GTN-Hill model to the isotropic GTN expression using von Mises equivalent stress. It is found that GTN-Hill is well suited for sheet metal forming processes.

For the anisotropic parameters in Eq. (61), Chen and Dong [134] suugests applying sheet roller parameters r_0, r_{90} and r_{45}, introduced in Eq. (67) and (68), to evaluate the values for the anisotropic parameters in the Hill formulation [110]. For the case where $L = M = N$ in Eq. (63), the anisotropic parameters may be expressed as,

$$F = \frac{r_0}{r_{90}(r_0+1)},\ G = \frac{1}{r_0+1},\ H = \frac{r_0}{r_0+1},\ N = \frac{(r_0+r_{90})(1+r_{45})}{2r_{90}(1+r_0)}. \tag{95}$$

Thus, by combining Eq. (95), (61) and (73) the effect of anisotropy and porosity in a metallic rolled sheet is expressed.

5.13 Mori Tanaka Model

The model presented by Mori and Tanaka in 1973 [46], has a basis of stress evaluation of a matrix material subjected to several uniformly distributed inclusions. The model is analytical and has seen most of its applications for composite materials, that is, materials consisting of more than one phase [135]. The Mori-Tanaka (MT) model has also been adopted for obtaining values for elastic properties in porous materials [135, 136].

A foundation for the MT model is the Eshelby tensor, which was previously discussed in Section 3.2. The MT relation can be expressed as [135],

$$\boldsymbol{C}^c = \sum_{i=1}^{n} f_i \boldsymbol{C}^i : \boldsymbol{A}^{\boldsymbol{i}}. \tag{96}$$

Where, n is the number of phases in a material, and correlates the volume fraction (f_i), stiffness tensor (C^i) and strain concentration (A^i) for phase i, in order to achieve the stiffness tensor of the composite material (C^c) [135]. The strain concentration of phase i is,

$$\boldsymbol{A}^i = \boldsymbol{L}^i : \left\{ \sum_{i=1}^{n} f_i \boldsymbol{L}^i \right\}^{-1} \tag{97}$$

where,

$$\boldsymbol{L}^i = \{\boldsymbol{I} + \boldsymbol{S}^i : (\boldsymbol{C}^m)^{-1} : (\boldsymbol{C}^i - \boldsymbol{C}^m)\}^{-1},\ i = 1, 2, ..., n \tag{98}$$

In which $\boldsymbol{I}$ is the identity tensor, $\boldsymbol{C}$ with the superscripts i and m are the compliance tensors for the inclusion and matrix respectively and $\boldsymbol{S}$ is the Eshelby tensor of phase i [45, 135].

For porous material application, one considers a composite material of two phases. Phase a being the matrix material with a given stiffness tensor, and phase b being the pore phase with corresponding zero stiffness. With VVF expressed as p, the corresponding fractions and compliance matrices are [135],

$$\begin{aligned} f_b &= p, \\ f_a &= 1 - p, \\ \boldsymbol{C}^b &= \boldsymbol{0}, \\ \boldsymbol{C}^a &= \boldsymbol{C}_m. \end{aligned} \tag{99}$$

Eq. (96) then becomes,

$$\boldsymbol{C} = (1-p)\boldsymbol{C}_m[p(\boldsymbol{I} - \boldsymbol{S}^p)^{-1} + (1-p)\boldsymbol{I}]^{-1}. \tag{100}$$

The MT model may be a suitable approach for highly porous materials, the model is reported to be applicable to be up to 30% VVF, but prediction accuracy may decrease if pores are highly overlapping or of non-spherical morphology [135]. The output from the analytical MT model is the compliance matrix of the voided material, and thus express elastic properties.

5.14 Modeling of Fatigue Resistance, Function of Defect Size

The fatigue performance of AM produced materials is a topic that is of great interest, due to AM being a suitable manufacturing method for fatigue sensitive applications such as aerospace industry [137]. The fatigue performance in AM produced materials is mostly dependant on local surface defects [138]. Significant variation in defects also subsequently lead to scattering in data [139]. A popular way to represent this relationship is through Kitagawa type diagrams. The concept was initially investigated for short cracks near the surface, and the initial result was that the fatigue threshold would not be compromised if the initial crack was below a specific size (l_0), this effect is schematically represented in Fig. 23.

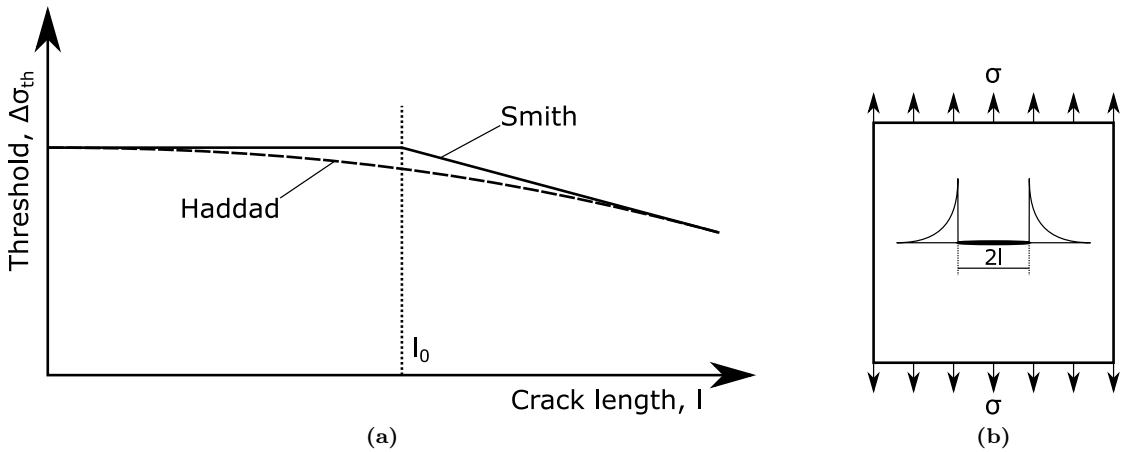

Figure 23: (a) Typical Kitagawa-type diagram adopted from [139]. (b) Example of fractured specimen in two-dimensions.

The relationship has been expressed and expanded upon by several contributors. El Haddad [140] formulated the stress threshold (σ_{th}) as a function of the stress intensity factor, and crack length (l),

$$\Delta\sigma_{th} = \frac{\Delta K_{th\,Ic}}{\sqrt{\pi(l + l_0)}}. \tag{101}$$

Where $K_{th\,Ic}$ is the threshold value for plane strain fracture toughness. For short crack lengths ($l \leq l_0$), σ_{th} is approximately equal to the materials fatigue limit, and then decrease more rapidly as $l > l_0$. A simpler approach for modeling the Kitagawa relationship was presented by Smith [141], where the relationship is expressed as two straight lines. Murakami et al. [139] reviewed existing models at the time of publishing (1993), including the two previously mentioned models. Further, Murakami developed an empirical model for a Kitagawa diagram which accounts for two-dimensional and three-dimensional defects, called the $\sqrt{area}$ Parameter Model. This model is expressed [139],

$$\sigma_{th}^n \sqrt{area} = C, where\, n \approx 6. \tag{102}$$

Where C is a definable constant, $\sqrt{area}$ is a parameter defined by projecting a surface defect to the plane perpendicular to the loading direction and evaluating the square root of this area. The size of the defect this function is applicable for is dependant on the material in question. C and n may be estimated through fatigue tests. Empirical estimations for C using the material Vickers hardness are suggested by Murakami et al. [139].

The $\sqrt{area}$ Parameter Model is in no small extent on the side of the focus of this thesis. Still, it is included, as it is considered a valuable approach for predicting the fatigue life of AM produced materials, as they are seen to inhabit significant surface defects, which are likely to influence fatigue life [142].

5.15 Multiscale Modeling

Multiscale modeling is a relatively new field of study and has seen developments with more accessible computational power [143]. The concept is to relate properties at different scales to a model, ensuring a more detailed and comprehensive analysis of a structure. Note that this field is indeed interdisciplinary, materials science is just one. In Horstemeyer's review on multiscale modeling [143], various benefits of multiscale modeling are presented. Among these benefits are, reducing the need for extensive large scale experiments and aiding in the development of new materials. The main goal of multiscale modeling may be addressed as predicting behavior at the structural scale without disregarding the effects of features at smaller scales.

The previously mentioned work by Eshelby (see Section 3.2) is an example of "micro-mechanics," where the continuity of the material is related to a smaller defect within. Hill [111] neologized the term Representative Volume Element (RVE) in the context of plasticity in textured aggregates. RVEs are meant to represent the geometry at the subscale. The chosen size of an RVE depends on the application and should be the smallest volume element that may accurately represent the properties at the structural scale. An illustration of this idea is seen in Fig. 24.

The defects apparent at the subscale may be modeled and analyzed as piece-wise continuous, and then related to the properties at the macro-scale [143]. "Micro-mechanics" and "multiscale"

are perhaps intertwined terms. Establishing a difference between them is necessary. In this thesis, multiscale modeling is generalized as the use of FEA to relate microstructural details to mechanical properties. The practice of utilizing FEA to explore properties at the subscale has seen interest in the evaluation of composites due to the inherently repeated non-homogenous structure throughout the material [144].

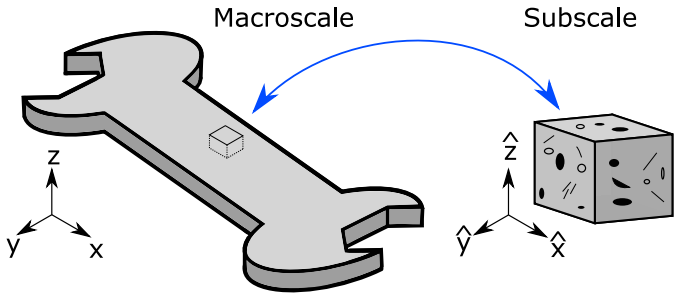

Figure 24: For illustrational purpose of the multiscale. Discrete microstructural features are related to a continuous medium at a structural scale. Figure inspired by [143]

A selection of reviewed articles utilizing multiscale modeling for porous metals are summarized:

Soro et al. [136] evaluated Young's Modulus for porous RVEs with spherical and spheroidal inclusions, the material in question was titanium and a prediction for young's modulus as compared to the MT-model. A similar study was done by Shen et al. [145], where porous titanium RVEs was developed in 2D and 3D, the results indicate that 3D-RVEs should be the area of concern for further development, as the 2D models require larger sized RVEs and that 2D-models may overestimate localization of high von Mises stresses.

Another material that has seen attention in this field is ceramics, which may be fabricated with initial porosity. Experimental data for Young's modulus and porosity was achieved for the nuclear ceramic $U0_2$, as well as a comparison with various analytical estimates and FEA [146]. As for pore morphology, Gatt et al. [146] claim that FEA should account for elliptical morphologies in voids, in order to achieve improved agreement between FEA and experimental results, as void morphology is a factor that influences Young's modulus to a more considerable degree. A modification to the Mori-Tanaka scheme that accounts for connected voids was presented in Ref. [135], this is accompanied by FEA results for validation. A reasonable agreement was achieved between the FEA and a modified Mori-Tanaka scheme. Chan et al. [147] performed FEA of RVEs with different void morphology and VVF and investigated the effect in terms of σ_y and UTS. With a multiscale approach where a representative RVE represents the largest pores observed in the material, simulations showed good agreement with experimental results.

6 Summary of Models, Mechanical Behavior Prediction

In this section, the models introduced in Section 5 is compared and discussed. Table 1 shows what the models are suited for describing accompanied by other information that could be of interest to the reader. A discussion of which models may be best suited for modeling AM produced materials follows.

Table 1: Summary of reviewed Material Models.

Model	Reference	Empirical	Semi-Analytical	Plasticity	Elasticity	Strain Rate	Temperature	Defect-Based	Anisotropy	Available in FEA	Fatigue
Ramberg-Osgood	[94]	x		x	x					x	
Johnson-Cook	[96]	x		x		x	x			x	
Zerilli-Armstrong	[103]		x	x		x	x			x	
Modified Johnson-Cook	[107]	x		x		x	x				
Quadratic Hill	[110]		x	x					x	x	
Generalized Hill	[111]		x	x					x	x	
Hill 1993	[112]		x	x					x		
GTN	[120]		x	x		x		x		x	
Rousselier	[127]		x	x		x		x		x	
Hammi Tensorial	[129]		x	x		x		x	x		
GTN-Nagaki	[131]		x	x		x		x	x		
GTN-Hill	[134]		x	x		x		x	x	x	
Mori-Tanaka	[46]		x		x			x	x		
$\sqrt{area}$ model	[139]	x						x			x

Smith et al. [6] summarized the challenges related to linking the process parameters and mechanical properties of AM produced materials (Process Parameter Mechanical behavior Model (PPMM)). For the computational characterization of mechanical behavior, it is suggested that a phenomenological model for this purpose may not be robust enough to be widely adopted. Instead, it is suggested that a link between the AM process and properties should be rooted in the actual physics of the induced microstructure. The GTN model incorporates this analytical factor and could be suited for establishing a PPMM for AM. Because of the large number of factors influencing the properties of AM materials, it seems highly likely that some phenomenological simplifications to the PPMM model are needed and practical.

Among all the models mentioned earlier, the GTN model stands out as a functional and straightforward model to continue investigating. The model is implemented in the FEA software Abaqus [148], which speaks for its recognition as a powerful tool for strength prediction. As will be apparent in the following section, the model may have its limitations. However, by being rooted in the physics of void behavior during loading, some aspects of the model can be characterized by non-destructive observation methods. The GTN model, in its original form, cannot model ductile fracture accurately as it does not calculate void growth or damage during shear loading conditions [149]. Still, the GTN model has the benefit of being researched, and expanded upon heavily [121, 123–125, 131, 134], even extended to fatigue life prediction [150]. How different process parameters in AM influence the values of the constants is a matter of future research. Knowing that the porosity of AM produced materials are related directly to printing parameters [22, 62, 74], it is not unreasonable to expect analytical or phenomenological estimations of the finished builds porosity to become more precise in the future. Porosity as a function of laser power and scanning speed has already been investigated with good results [28, 65, 151]. Incorporating other factors, such as hatch spacing, layer thickness, and scanning strategy into a more complicated model would be beneficial, as these parameters also affect the resulting strength.

By assuming porosity as one of the most influencing defects in AM produced materials, the GTN model [116, 120] is given increased attention for the subsequent investigations. For the Elasticity in AM produced materials, another approach is needed. The Mori Tanaka model [46] may be a practical and straightforward method for estimating the compliance matrix of porous metals, but the possibilities within Multiscale modeling [143, Chapter 4] should not be underestimated. Through Monte Carlo simulations of randomly oriented voids in a RVE representing an AM produced material, FEA may yield approximated values for Elastic properties for a large variety of different porous metals.

While the case of applying GTN might be the most interesting, it would also be beneficial to acquire constants for a simple phenomenological model, such as the Johnson-Cook Model, for AM produced materials tested at different strain rates and temperatures. By performing the necessary experiments to establish these constants for materials printed with optimal printing parameters. One can effectively model the plastic behavior of these materials in FEA and perform accurate simulations of engineering applications.

As AM materials are often seen to inhabit anisotropic behavior [3], Hill's quadratic model [110] could be considered as a model to represent this factor. The number of constants for representing the Effective stress due to Hill may be reduced by establishing directions of symmetry in mechanical behavior, or directions in which the anisotropy is negligible. A defect based model would enable the user to evaluate anisotropy using non-destructive image processing techniques such as Computed Tomography (CT), and represent the anisotropy as a function of defect aspect ratio or uneven distribution of voids. Therefore it is of interest to consider the suitability of implementing Nagaki's [131] anisotropic yield function for AM materials. A challenge related to the

modeling of the anisotropy is to express the increased anisotropy in regards to strain compared to stress [17]. If the anisotropic formulations presented can accurately model this behavior will be an interesting topic to investigate.

However, the work presented in this thesis assumes materials as isotropic. The models that are the primary subject for further research in this work is the GTN model for plasticity and multiscale modeling for elastic properties.

7 GTN Parameter Study for Highly Porous 316L

In this section, the procedure for implementation of the GTN-model in Abaqus is presented. The results are discussed and compared with that of experimental values found in the literature. The motivation behind this is that there are no established parameters for this highly porous material. A further investigation of the GTN model will be presented in Section 9.8. Consider this an introduction to the Abaqus setup procedure and as the section title suggests, an initial parameter study.

7.1 Comparison between Gurson and GTN Model, Effect of VVF

Gurson's original postulation [116] is achieved through setting $q1 = q2 = q3 = 1$ in Eq. (73), further, one can see that with $f^* = 0$ the model reduces to the classical isotropic hardening known as the von Mises criterion. To investigate the effect of f^* on the GTN model, the equation has been simplified as,

$$\phi = a^2 + 2q_1 f^* \cosh\left(\frac{3q_2}{2}b\right) - 1 - (q_3 f^*)^2 = 0 \tag{103}$$

where,

$$a = \frac{\sigma_{eq}}{\bar{\sigma}}\,,\; b = \frac{\sigma_h}{\bar{\sigma}}. \tag{104}$$

a and b are normalized equivalent stress and normalized hydrostatic stress, respectively.

Fig. 25 shows the sensitivity in regards to f for the GTN model, the curves are symmetric over $\sigma_h = 0$. A small increase of f effectively reduces σ_{eq} significantly. For higher values of σ_h, the difference is increasing faster. It seems reasonable that the equivalent force should be lower with a larger amount of porosity. An investigation of the effects of q_1 and q_3 has been performed in the same fashion. These values do not have a large effect on the normalized equation, leading to the assumption that it is most important to have accurate values for the Void constants, (f_0, f_N, f_c, f_f), in order to achieve a realistic fit for the model. Similar results are found in other studies [152, 153].

7.2 Procedure for Application of the GTN Model

From a tensile test simulation, GTN parameters may be established through trial and error in FEM software [121, 152]. The experiment should be replicated in the software, and different

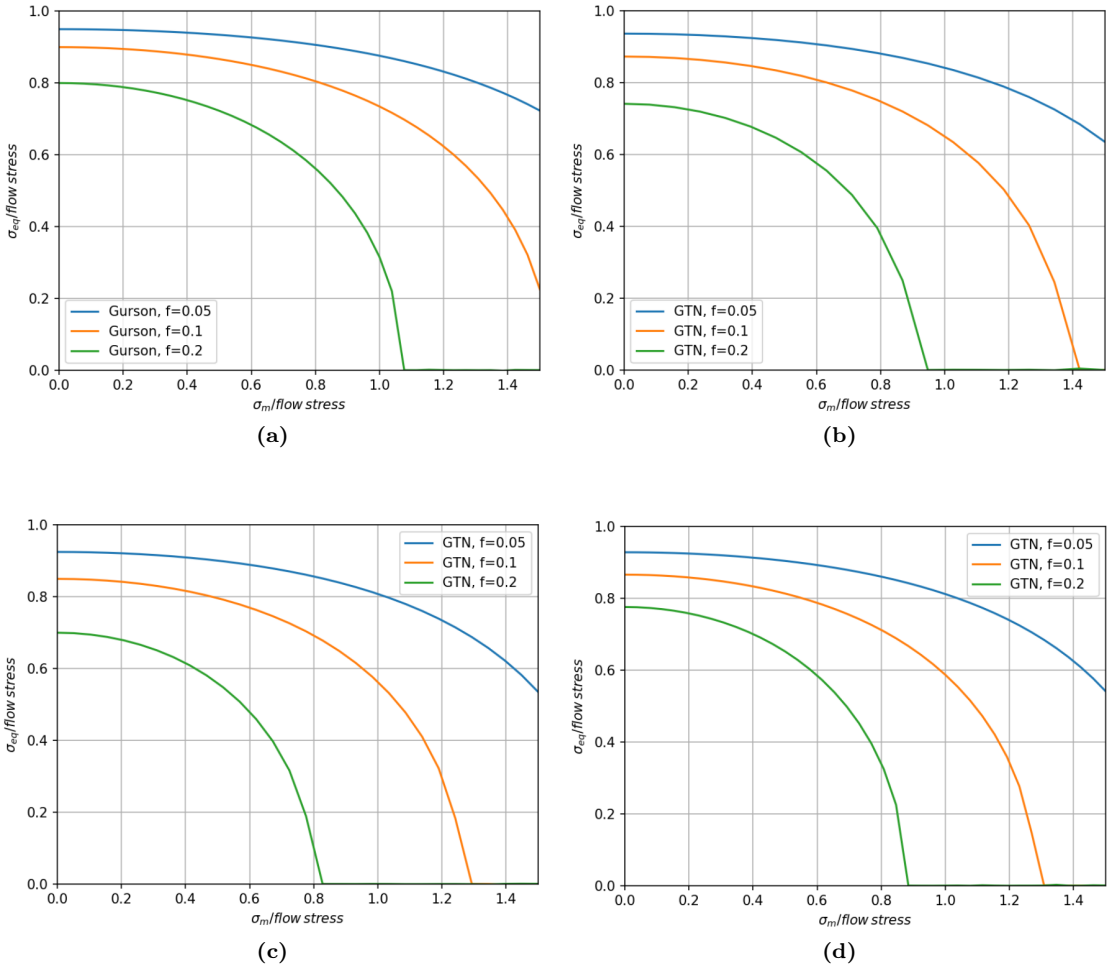

Figure 25: Normalized equivalent stress versus normalized hydrostatic stress with different VVFs for (a) Gurson's original formulation (q_1, q_2, $q_3 = 1$), (b) GTN model with, $q_1 = 1.25$, $q_2 = 1$, $q_3 = q_1$ (c) $q_1 = 1.5$, $q_2 = 1$, $q_3 = q_1$ and (d) $q_1 = 1.5$, $q_2 = 1$, $q_3 = q_1^2$

parameters in the GTN model implemented in said software could be changed in each iteration until a stress-strain curve fitting the experimental results is replicated. The original VVF should be determined for the material. Experiments should also establish Young's modulus and Poisson's ratio. The hardening of the solid material is used as a reference. The solid material's hardening could be expressed through tabulated values or an expression for the hardening as a function (e.g., power-law) [121]. By applying the GTN model, the strain hardening is softened [152].

The determination of the constants in the GTN model through experimental testing and direct measurements are difficult [92]. Therefore a comparison between numerical results and material response is often the most viable method.

7.3 Experimental Data From Literature

Falkowska et al. [154, 155] used a model for predicting fatigue strength of sintered 316L steel. The article investigates the mechanical properties of the solid steel as well as that of 26, 33, and 41 % VVF. The porosities are results of sintering pressure of 200, 400, and 600 MPa. These high amounts of porosity significantly reduce mechanical properties. The stress-strain curves and microstructure of the material are shown in Fig. 26.

Well defined mechanical properties make the data in this report suitable for this initial investigation. Relevant properties are found in Table 2. The porosity effectively reduces both elongation at failure (ε_f), yield stress,(σ_y), Young's module and UTS.

Table 2: Experimental tensile properties for sintered 316L steel, with corresponding porosity [154].

VVF	$\sigma_{0.2}$, (MPa)	UTS, (MPa)	E, (GPa)	ε_f, (%)
0	235	592	196.2	53.1
0.26	93.5	177.7	80.0	8.3
0.33	75.6	113.1	52.1	4.26
0.41	42.2	60.0	29.7	2.36

7.4 GTN Parameters

A tensile test in Abaqus is performed. Parameters are changed iteratively in order to achieve a good fit for the curves. The values for $q1$, $q2$, $q3$, S_N, ε_N are chosen as found in the literature. The values for σ_y and ε_y are provided through the S-S curve of the fully dense material in Ref. [154]. f_0 is the original void volume fraction, which is kept constant at 0.26, 0.33, and 0.41. The remaining parameters to determine are f_c, f_f and f_N. The void-parameters are critical for the values at fracture and UTS. As seen by the engineering S-S curves in Fig. 26b, there is no strain-softening present. This leaves the assumption in the analysis that failure happens at the UTS, i.e., when the VVF reaches the specified value of f_c, and coalescence initiates. Thus, the value of f_f will not affect the results significantly. A schematic for how the void-parameters affect the stress of the material is shown in Fig. 27.

In a parametric study on the function f_N by Slimane et Al. [117] it is shown that f_N only has a significant role in the fracture region. The parameters q_1 and q_2 show a large influence on void growth fraction.

7.5 Geometry and Mesh

A tensile specimen is modeled after the geometries used in Refs. [154] and [155], see Fig. 28. The model is of rectangular cross-section. The mesh was created using C3D8R elements from the explicit element library, which is an 8-node linear brick, using reduced integration and hourglass control. The kinematic split is set to orthogonal. The GTN model is only applicable to Abaqus Explicit, likely due to the high non-linearity and time-step dependent behavior.

The GTN model is shown not to be particularly sensitive to mesh-size [117]. The mesh is therefore made relatively coarse. Due to uncertainty related to the position of the first failing elements, the mesh is refined around the thinner part of the specimen [152]. The total number of elements

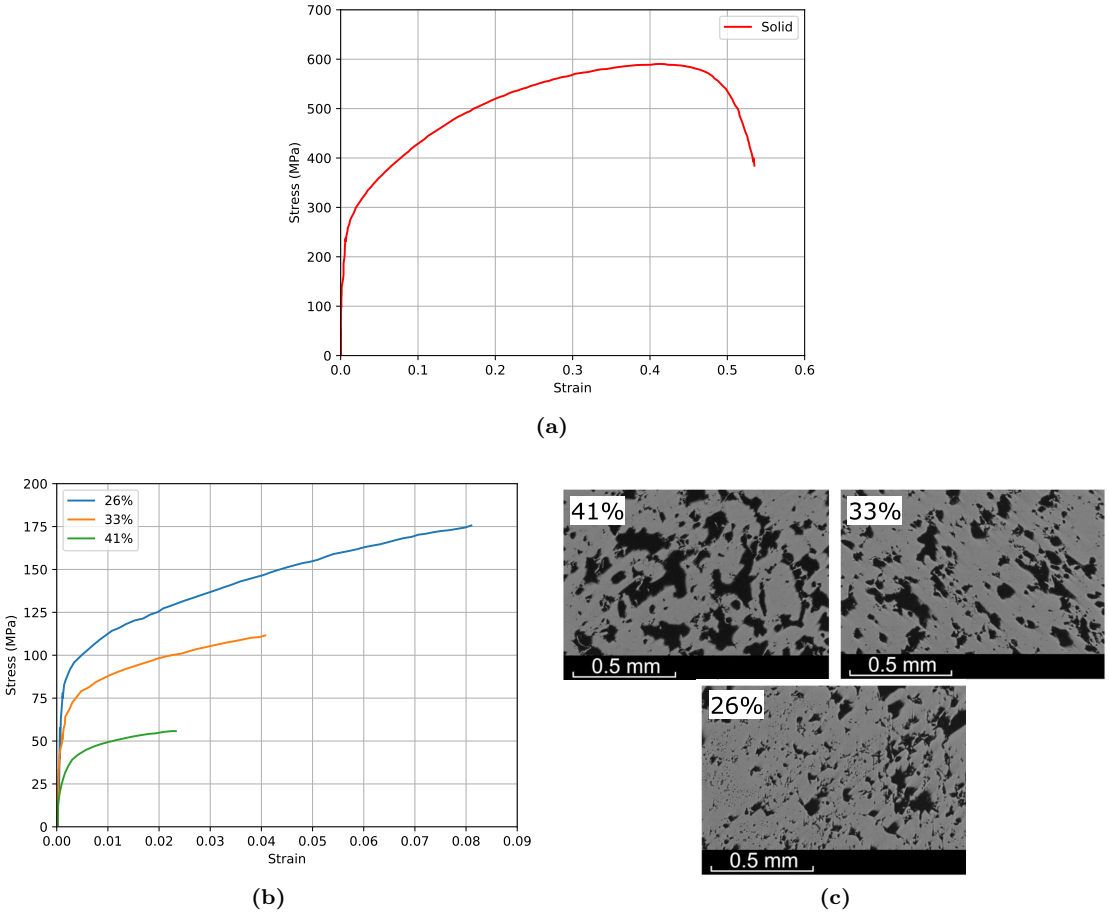

Figure 26: Stress-Strain curve for (a) Solid material, (b) Porous material, and (c) corresponding section view showing porosities. [154]

Table 3: Material constants used in parameter study.

q_1	q_2	q_3	S_N	f_N	ε_N	σ_y, (MPa)	E, (GPa)	f_0
1.6	1	q_1^2	0.1	0.3	0.1	235 MPa	196.2	f_0

for the uncut model is 1470. As the model is symmetric over each plane, the model may be reduced to lessen the computational time. Since the analysis did not require long computational time, the full geometry was used for all simulations.

7.6 Defining Material

The unit-less interface in Abaqus has been considered, and care is taken in order to have consistent units throughout the analysis. The dense material's hardening behavior is defined using tabulated plasticity values of the true stress and strain, which is achieved through evaluated by using, Eq.

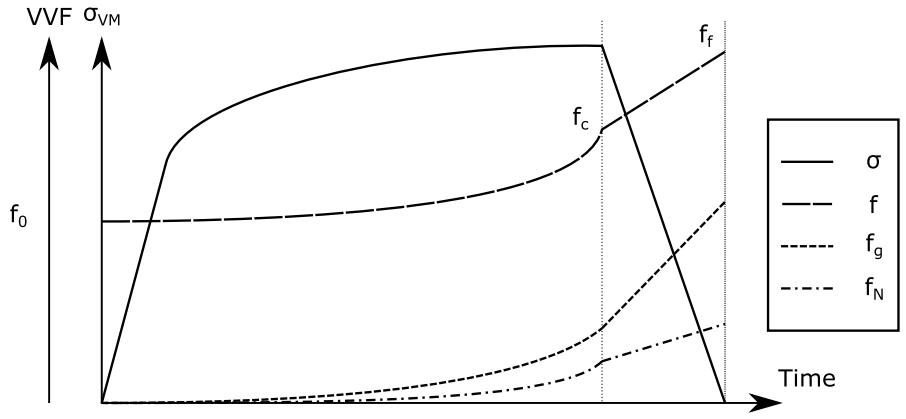

Figure 27: Schematic illustration of the effect of f_0, f_c and f_f for the GTN model in Abaqus. Not in scale.

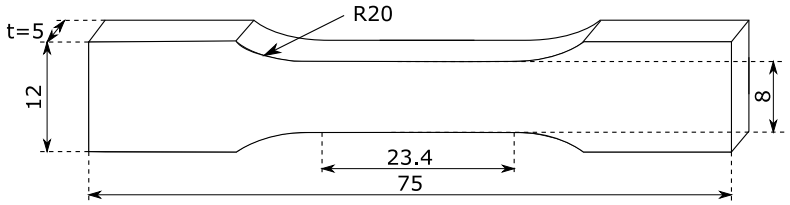

Figure 28: Geometry used in Abaqus simulations. [154]

(22) and (23, for the data in Fig. 26a. Porous Metal Plasticity (GTN) is applied with the constants in Table 3, as well as those that are iteratively changed (f_N, f_c, f_f). The values q_1, q_2, q_3 are within the recommended range specified by the Abaqus user manual [97, Porous Metal Plasticity]. An attempt at using the model with a higher q_1 than that recommended in the Abaqus user model was carried out, and this caused problems with convergence. f_0 is constant at 0.26, 0.33 and 0.41.

7.7 Boundary Conditions

The fixed boundary condition is applied to one end, while the other is given a forced displacement in the X-direction. The applied displacement must be sufficiently large to capture the particular strain for each percentage of VVF. The amount of displacement is changed between the different tests such that the maximum strain is higher than ε_f as seen in Fig. 26b.

7.8 Results and Discussion

First, a simulation without any GTN parameters modeled is applied, the simulation runs fast and provides almost the same result as the experimental data. Applying the GTN equation to the material makes the model run significantly slower; this is due to the additional calculations needed to be performed for each increment. A subroutine flow chart for the GTN model can be found in Refs. [134, 156]

The first result to be given attention is that of the GTN model's prediction of the onset of plasticity. The onset of plasticity is completely dependant on the initial VVF, f_0. The model failed at predicting the onset of plasticity from the experiments in Ref. [154]. Fig. 29 shows this difference.

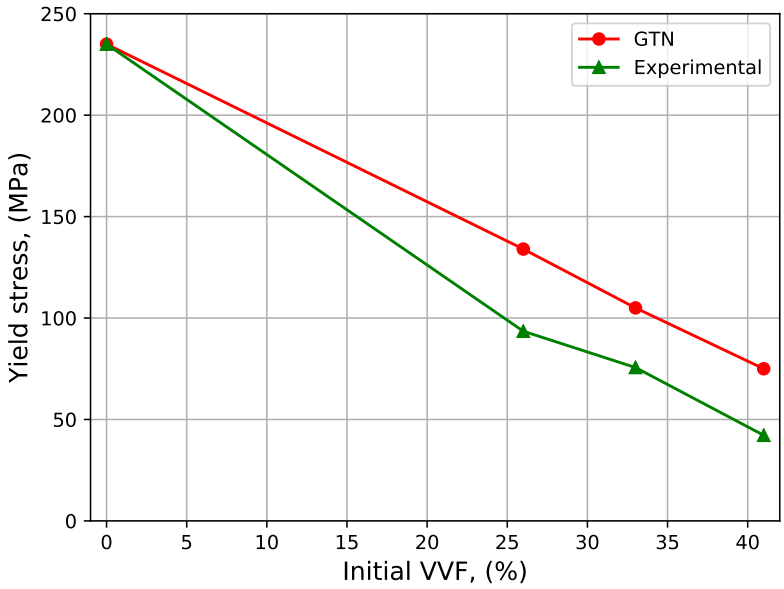

Figure 29: Yield stress and Initial VVF from the Abaqus simulations and data from Falkowska et al. [154]

This means it was not achievable to accurately predict the reduced strength using the GTN model. Thus the procedure presented overestimates the strength of the porous material. The Tvergaard constants fail to reduce the strength sufficiently when compared to the experimental results. The inability to acquire realistic values for yield strength could be attributed to the assumed average size and spacing between voids in the GTN model (continuous averaged stress). In highly porous materials, voids are rarely spherical, but rather in large conglomerate formations which cause more considerable local stresses. Some modifications to the model are necessary in order to achieve accurate results.

The reduced hardening, due to void growth and nucleation, was however quite accurately predicted by the GTN model. This is shown in Fig. 30a, where the Equivalent Plastic Strain (PEEQ) is plotted against the von Mises stress. Values are averaged over the whole range of failing elements.

A suggested approach that could aid the prediction accuracy of the plastic behavior by using GTN is to introduce a correction factor post-analysis.

$$\sigma_{corrected} = K(f_0)\sigma_{GTN} \tag{105}$$

If we correct using only the difference in yield stress, ($K = \sigma_{y\,experiment}/\sigma_{y\,numerical}$) we have,

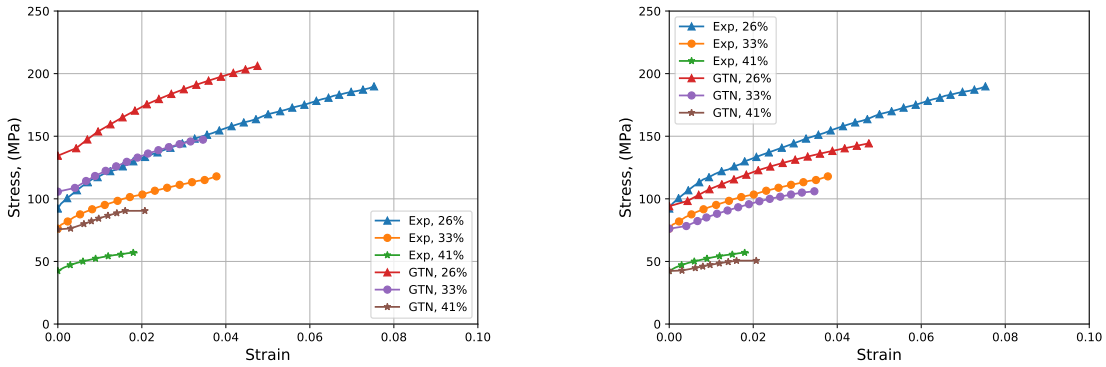

Figure 30: PEEQ and von Mises stress for the simulations in Abaqus compared to true stress-strain curves from Falkowska et al. [154]. (a) without correction and (b) with correction for σ_y.

$K(0.26) = 0.7$, $K(0.33) = 0.72$ and $K(0.41) = 0.56$. The results after having utilized this correction is shown in Fig. 30b.

This study was primarily concerned with the setup for applying the GTN model in Abaqus [97]. Therefore, attention to achieving the correct point of fracture was not prioritized. As seen in Fig. 30, correct failure was not obtained for the 26 % VVF analysis. Failure was, however, accurately predicted for the two other VVFs. GTN void parameters that achieved the fits visualized in Fig. 30 are given in Table 4.

Table 4: GTN void constants for the highly porous 316L-steel. A good approximation was not achieved with $f_0 = VVF$.

f_0	f_f	f_c	f_n
0.26	0.305	0.275	0.1
0.33	0.375	0.365	0.1
0.41	0.450	0.420	0.1

8 Multiscale Modeling Study

This section consists of two independent studies. Both regard the utilization of multiscale modeling to explore mechanical properties in the elastic regime for porous materials.

In the first study, an approach on how to generate porous cubes using Mote3D [157] is explored. The analysis is limited to the generation of unit cubes and exploring the necessary considerations needed in order to achieve a desirable amount of porosity in a RVE.

Secondly, a newly published Abaqus [97] extension called EasyPBC [158] is utilized to generate compliance matrices for unit cubes containing a single spheroidal void.

8.1 Young's Modulus of Porous Materials

Simple empirical equations for estimating Young's modulus of porous materials are presented throughout the literature [159–162]. Generally, it is common to express Young's modulus of the porous material (E_p) as a function of Young's modulus of the solid material (E_0) and the porosity fraction (p). It may be tempting to assume a linear dependence between the increase in VVF and Young's modulus,

$$E_p = E_0(1-p), \tag{106}$$

or with a correction factor [163],

$$E_p = E_0(1-c_1 p). \tag{107}$$

A linear dependence is likely within short porosity-ranges ($p \leq 0.05$) [163]. For a larger range, the experimental publications show a more nonlinear relationship to be closer to reality. A few empirical or semi-empirical expressions commonly used are [159],

$$E_p = E_0 \mathrm{e}^{-q_1 p}, \tag{108}$$

$$E_p = E_0(1-q_2 p)^{r_1}, \tag{109}$$

$$E_p = E_0\left(\frac{1-p}{c_2+q_3 p}\right), \tag{110}$$

$$E_p = E_0\left(\frac{(1-p)^2}{1+{}^{p}/_{(c_3-1)}}\right). \tag{111}$$

With c, r and q representing material constants. Another idea presented is to evaluate the porosity fraction at which Young's modulus is zero and fit the curve to this value. One function that accommodates this effect is [164],

$$E_p = E_0\left(1-\frac{p}{p_c}\right)^{r_2}. \tag{112}$$

Where p_c is the porosity fraction where $E = 0$. Thus this relation only holds for the range $p = [0, p_c]$. An interesting side note to Eq. (112) is that r_2 tends towards 2.1 as the matrix material is of infinite size, however it is seen as much lower (1.1 - 1.7) in experiments. Thus, one can assume the universality of r_2 to be limited by specimen size [164].

The empirical equations listed above differ from the Mori-Tanaka scheme (Section 5.13) in that they are not based on tensors. They may be used as a rule of thumb to estimate Young's modulus of a porous material, but require accurate material parameters in order to make accurate predictions, even if some are semi-empirical.

8.2 Relative Density of Porous Materials

There has been a wish to investigate how to model randomly generated spheroids in a unit cube. These cubes can be modeled as RVEs for a porous material, and by applying loads or displacements in FEA software for estimations to how porosities affect mechanical properties [136]. Before generating cubes, a simple analysis of the effect of pore diameter (d) and the number of inclusions (n) is presented. The relative density of a porous RVE of non-overlapping voids with uniform diameter may be represented as,

$$R_d = V_{cube} - V_{pores} = V_{cube} - \frac{4}{3}\frac{d^3}{8}\pi n. \tag{113}$$

Where d is the void diameter, and n is the number of voids. Eq. (113) provides a guide to how possible arrangements of d and n, could be in order to achieve a desired relative density. For a series of completely uniform non-overlapping voids, a 3D plot showing the relative density of a unit cube with varying n and d is shown in Fig. 31. For a specific VVF p the Eq. (113) can be translated to,

$$d^3 = \frac{p\frac{3}{4}8}{n\pi}. \tag{114}$$

The required diameter of spherical voids, with respect to the porosity levels presented in Fig. 26 (26, 33 and 41 %), for an RVE of unit volume, is investigated using Eq. (114). The results are found in Fig. 32. This equation, assumes all voids to be spherical and completely contained within the domain of the RVE.

Naturally, the Relative Density decrease rapidly with increasing numbers, n and diameters, d. However, as seen by the contours in Fig. 31 many arrangements can give the desired VVF in an RVE. Whether one chooses to have fewer voids with larger diameters or vice versa might affect the results. Generally, a higher number of voids lead to less deviation in the calculated Young's modulus [49, 136].

8.3 Randomly Generated Voids

Mote3D [157] is an open-source tool made to simulate sintered materials. Through a script in Octave GUI [165] spheres are generated within a cube of desired size, Ω_{cube}. The spheres may be used as solids or voids. For this investigation, the aim is to generate cubes that represent the

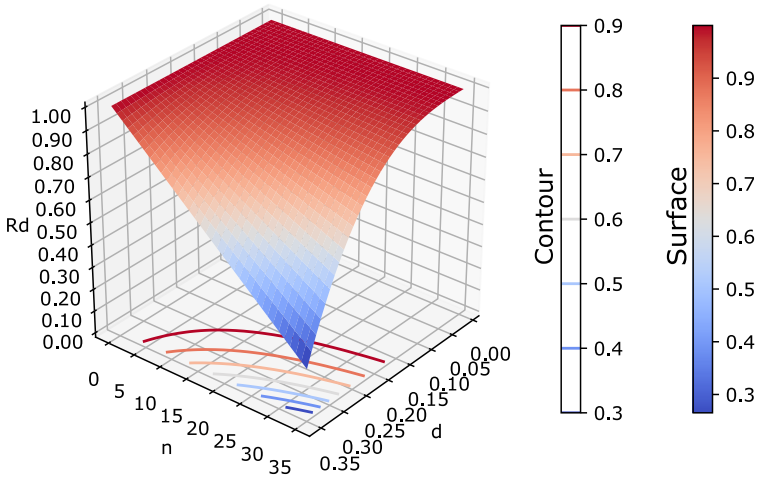

Figure 31: A 3D plot showing how the relative density, (R_d) decreases as the number, (n) and diameter, (d) of spherical voids increase.

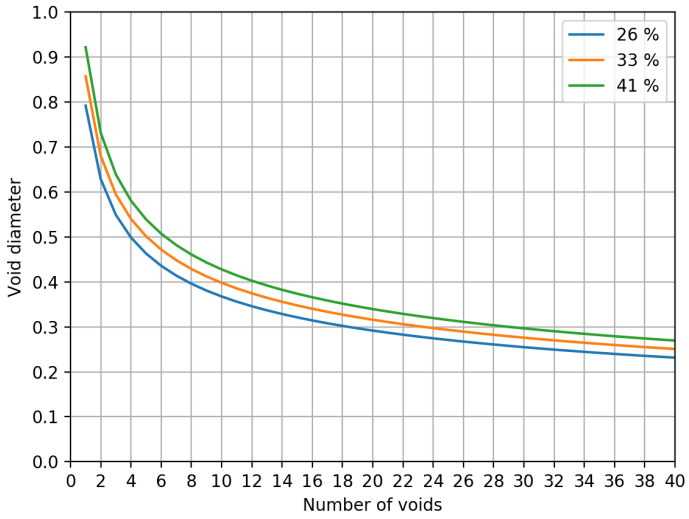

Figure 32: Required diameter of voids for the desired VVFs.

microstructure of that given in Ref. [154]. With VVFs approximately equal to what is presented in Fig. 26.

For this investigation, unit cubes will be generated to consist of the volume fractions presented in the previously investigated data for sintered 316L steel [154] in Section 7.3. The reduction of Elastic properties will be left to calculate in future work.

8.3.1 RVE Modeling Procedure

Mote3D prompts the user for the following input parameters [157],

- Edge length L of the cubical domain Ω_{cube}.
- Number of spheres within Ω_{cube}, n.
- Mean diameter of spheres, d_{mean}.
- Standard deviation in diameter, S_d
- Overlap factor for the spheres, c_{lap}. c_{lap} must be within 0 to 1, where 0 is allowing full overlap, while 1 allows no overlaps.
- Maximum number of trials to position spheres
- If the list of spheres should be sorted
- If the generated microstructure should be plotted in Octave.
- If the output model should be in the form of an Abaqus Input script or Voxel mesh.

The output after an iteration of Mote3D is thus, either a model input script or a voxel mesh input script. The model input script generates a 3D-CAD model of the spheres, which can then be used to cut a cube of the same edge length as specified in order to achieve a porous cube. The voxel mesh input script discretizes spheres as hexahedral elements of specified size within Ω_{cube} [157].

Eq. (114) is used to estimate approximate values of d and n. Still, a sufficient amount of deviation in diameter is applied to simulate the stochastic voids in the material.

Table 5: Input parameters in Mote3D.

L	d	n	S_d	c_{lap}	Output
1	d	n	(1/8)d	1	Model Input Script

For the cubes generated, input parameters are as defined in Table 5. The standard deviation, S_d of the particles is defined arbitrarily as 12.5% of the mean diameter, d. This provides some randomness in the sphere sizes but still ensures a manageable deviation in terms of volume.

Here, three runs of each volume with n set to 12, 25, and 38 sphere inclusions are considered. The VVF of each model generated is recorded. Fig. 33 shows three models for a target VVF of 0.33.

8.3.2 Accuracy of Volume

Table 6 shows the resulting volumes of RVEs with a stochastic distribution of voids, the average volume of the three iterations, and the deviation from the targeted VVF (Error, (%)). Fig. 34a shows how the error decrease by increasing the number of voids in the model. Fig. 34b indicates that the higher the target VVF, the larger the error. This makes sense, as with a higher VVF but a constant number of inclusions, the diameter must increase, leading to a more significant loss of volume if the cubic domain cuts one sphere.

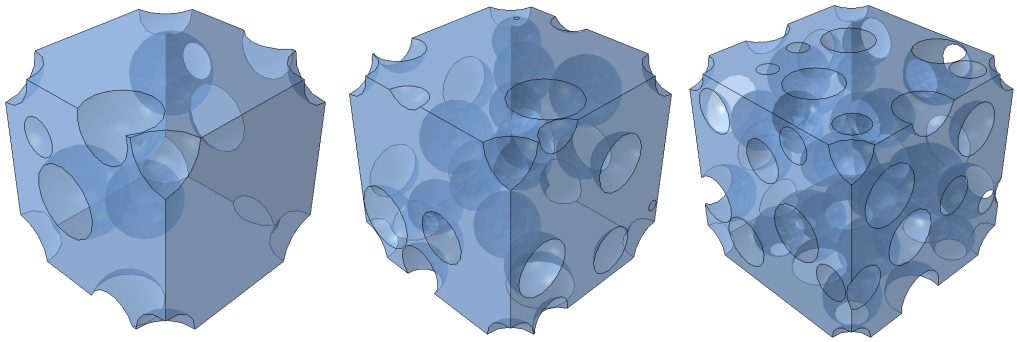

(a) **(b)** **(c)**

Figure 33: Porous cubes with spherical voids generated using Mote3D. (a) 12 voids, (b) 25 voids and (c) 38 voids.

Table 6: Void Volume fraction of generated RVEs.

	Target VVF	0.26	0.33	0.41
$n = 12$	d	0.346	0.374	0.403
	S_d	0.043	0.047	0.050
	VVF It.1	0.119	0.170	0.172
	VVF It.2	0.108	0.189	0.151
	VVF It.3	0.124	0.160	0.174
	Average	0.117	0.173	0.166
	Error, (%)	55.0	47.6	59.6
$n = 25$	d	0.271	0.293	0.315
	S_d	0.034	0.037	0.039
	VVF It.1	0.209	0.279	0.298
	VVF It.2	0.208	0.267	0.311
	VVF It.3	0.193	0.230	0.274
	Average	0.203	0.259	0.294
	Error, (%)	21.8	21.6	28.2
$n = 38$	d	0.236	0.255	0.274
	S_d	0.029	0.032	0.034
	VVF It.1	0.250	0.316	0.351
	VVF It.2	0.227	0.309	0.340
	VVF It.3	0.213	0.294	0.344
	Average	0.230	0.306	0.345
	Error, (%)	11.5	7.2	15.9

8.3.3 Discussion, Modeling of Random Spherical Voids

The larger error in volume on the cubes modeled with few voids is attributed to the increased loss of volume from cut spheres. Eq. (114) was not sufficiently accurate to estimate the amount

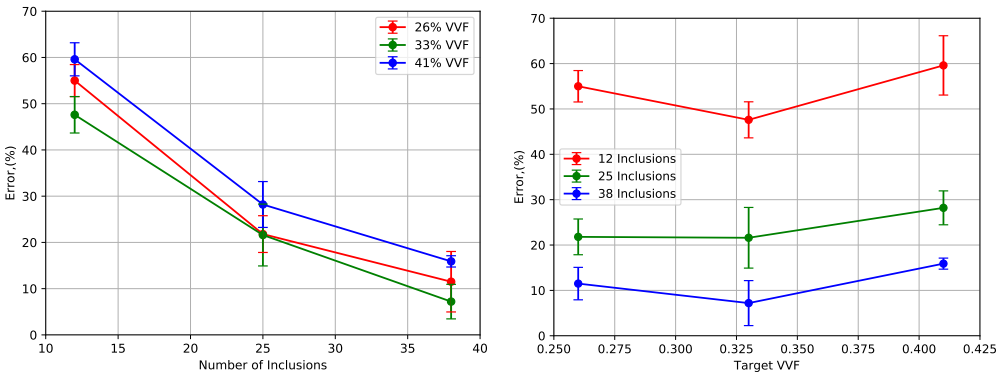

(a) **(b)**

Figure 34: Error in volume as function of, (a) number of inclusions and (b) Target VVF.

of, and size of voids. It serves as a rule of thumb in generating cubes, but not much else. A more sophisticated equation should be used for accurate predictions. The current version of Mote3D used in this investigation fixes 8 of the sphere centers to the corners of the cubic domain, resulting in a loss of 87.5 % of volume for these eight voids, this was not combated in this investigation. Other RVE generating software's are available, a few of them are, Combs [166], OpenPM [167] and Netgen [168].

Another weakness of Mote3D in the application of modeling RVEs for AM produced materials is that all voids are spherical. While this behavior may be satisfying for some applications, the observed voids resulting from AM are more often elliptical. For appropriate simulations of RVEs, this effect should be accounted for, Netgen [168] provides more freedom in the modeling and could be an exciting application to explore further for AM produced materials.

Due to the lack of comparability to the RVEs with random voids and that of the microstructure seen in the materials in question in both AM produced materials and Ref. [154], the compliance matrix or Young's modulus was not evaluated. The mesh needs to be very small in order to perform a successful FEA, and the computational time required to estimate the elastic properties were too significant to be incorporated in this thesis. The success of using randomly generated voids to predict material properties of AM produced materials were not evaluated in this work.

A microstructure cannot be modeled in its entirety. The variation in void size and shape means the mesh would need to be almost infinitely small. What is suggested as a possible way to combat all this is to focus on the largest pores observed in the material. An approach on how to do this, and what results to expect is presented in the next section.

8.4 Single Spheroidal Void

The following section will evaluate the effectiveness of an RVE approach for estimating the decreasing material strength as a result of spheroid voids. For this investigation, Abaqus [97] was used to model the simple geometries as well as performing FEAs. The relatively new Abaqus

plugin EasyPBC [158] is used to determine the effective Young's modulus in each principal direction as well as shear modes. EasyPBC automatically generates the necessary Periodic Boundary Conditions (PBC) and averages stress and strain in all elements to calculate the mechanical properties of an RVE [158].

8.4.1 Preliminary Discussion

Jana investigated the Elastic-plastic behavior of a single ellipsoidal inclusions [169]. Here it is found that the results from an Abaqus simulation compare excellently with the semi-analytical Eshelby formulation [45] for ellipsoidal inclusions, which was previously discussed in Section 3.2. The investigation is only done for one size ellipsoid. Chan et al. [147] considered single voids of different morphology in RVEs in order to achieve a mechanical behavior prediction for microvoids in a metal. The models were incorporated in a larger size model and placed in coordinates which represented a CT scan of the material. The investigation is focused on the UTS as a result of void shape. Other numerical investigations on spheroidal inclusions are lacking in the literature. The investigation presented in the following sections is primarily meant as a description of the steps used for achieving Elastic properties, as an effect of voids through a multiscale approach.

8.4.2 Modeling Procedure

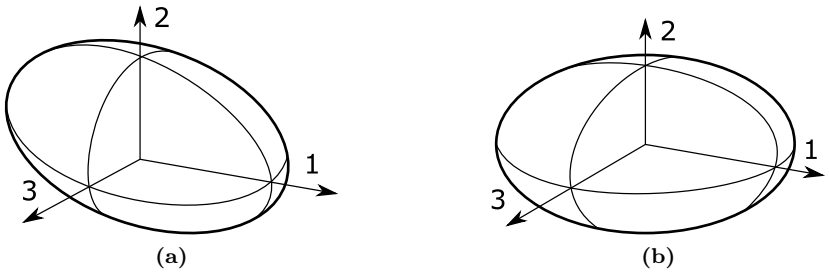

Figure 35: (a) Prolate spheroid (b) oblate spheroid

For the investigation presented in the present work, material properties are chosen arbitrarily as $E_0 = 200\text{GPa}$ and $\nu_0 = 0.3$. The material is fully isotropic, and the investigation does not consider plastic behavior. RVE cubes have a volume of $0.001\,\text{mm}^3$. Two types of ellipsoids are investigated. A prolate and oblate spheroid. Their shape is defined with an aspect ratio of 0.5, by considering,

$$\alpha = \frac{Smallest\,Dimension}{Largest\,Dimension}. \tag{115}$$

Where α is the aspect ratio. As illustrated by Fig. 10, ellipsoids have dimensions a_1, a_2, and a_3. For the prolate ellipsoid, $a_2 = a_3$ and $a_1 = 2a_2$. For the oblate ellipsoid $a_1 = a_3$ and $a_2 = 0.5a_1$. The volume of an ellipsoid is,

$$V_{ellipse} = \frac{4}{3}\pi a_1 a_2 a_3. \tag{116}$$

By $\alpha = 0.5$ and setting $V_{ellipse}$ as 1, 2.5 and 5% of the RVE volume. The dimensions for both ellipses are found for each representative volume fraction and then modeled in Abaqus as described by Fig. 36. The geometry is validated using the query option "mass properties". All RVEs achieve the desired R_d. The mesh is made from C3D8R elements, which is an 8-node linear brick, reduced integration, and hourglass control is applied. The mesh is refined around the inclusion as this region will be the most stressed. Fig. 37 shows a section cut of the meshed geometry.

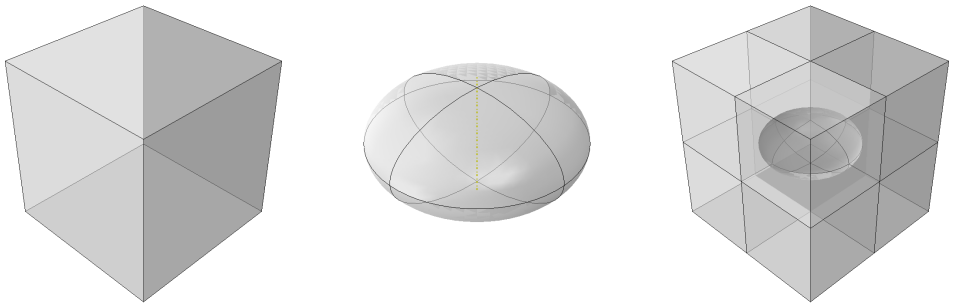

(a) **(b)** **(c)**

Figure 36: Modeling procedure in Abaqus. (a) Unit cube generated, (b) spheroid (oblate or prolate) $\alpha = 0.5$ with desired volume, (c) cut the unit cube using the ellipsoid. The geometry is partitioned to enable local seeds for the mesh.

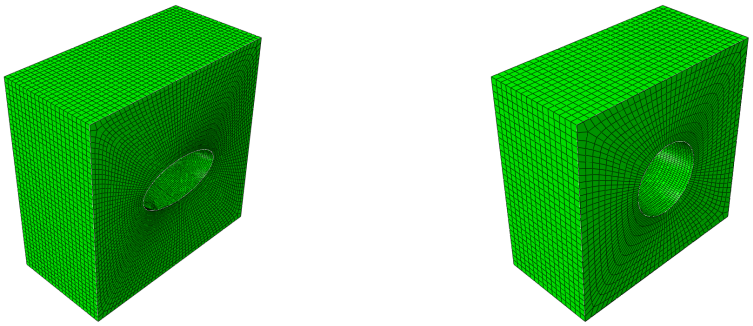

(a) **(b)**

Figure 37: Meshed geometries for the 5% VVF spheroids. (a) Oblate and (b) Prolate.

After all six RVEs are modeled. EasyPBC [158] is applied to all principal axis as well as shear modes to and results are processed. A projection of one RVE stretched in the principal axis is seen in Fig. 38a.

8.4.3 Results RVE with Single Spheroidal Void

The modeled cubes are in principal orthotropic and the elastic properties may be expressed by a compliance matrix of the same form in Eq. (11). Table 7 shows the resulting elastic properties for each RVE from the EasyPBC analysis. Due to the additional symmetry present in the

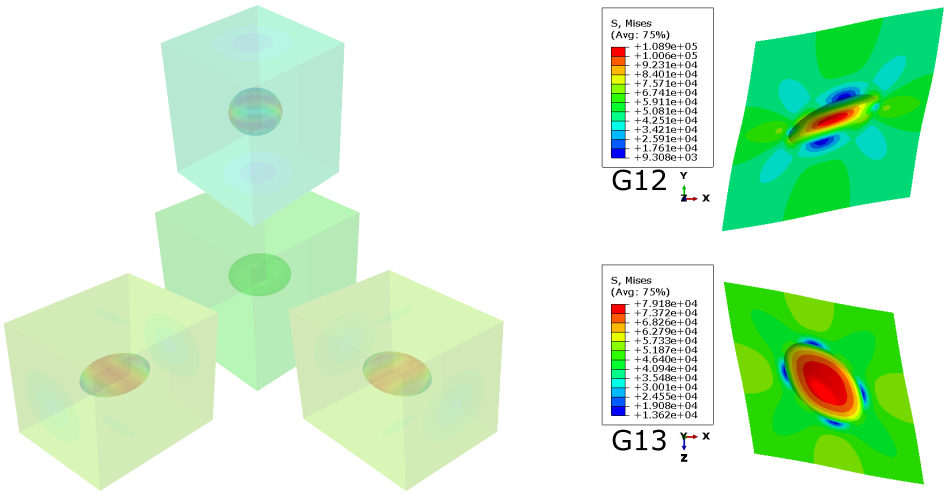

(a) **(b)**

Figure 38: RVE with 2.5 % VVF. Oblate ellipsoid of $\alpha = 0.5$, (a) stretched in principal axis for calculation of E_{ii}. And (b) stress distribution over the same RVE in two shear modes.

Table 7: Elastic properties for two shapes of spheroidal voids in an RVE. Abaqus and EasyPBC [158] are used. Stress units are GPa.

Shape	-	Prolate			Oblate		
VVF(%)	0	1	2.5	5	1	2.5	5
E11	200,00	197,183,6	193,13	186,83	196,85	192,23	185,10
V12	0,3	0,29980	0,29937	0,29842	0,30017	0,30039	0,29993
V13	0,3	0,29980	0,29937	0,29842	0,29901	0,29739	0,29477
E22	200,00	195,382,87	188,79	178,64	194,06	185,27	172,33
V21	0,3	0,29706	0,29265	0,28534	0,29592	0,28951	0,27924
V23	0,3	0,29880	0,29680	0,29289	0,29592	0,28951	0,27924
E33	200,00	195,382,90	188,79	178,64	196,85	192,23	185,10
V31	0,3	0,29706	0,29265	0,28538	0,29901	0,29739	0,29477
V32	0,3	0,29880	0,29680	0,29289	0,30012	0,30039	0,29993
G12	76,923	75,522,42	73,418	69,933	75,197	72,513	68,135
G13	76,923	75,522,42	73,418	69,933	75,739	73,954	71,026
G23	76,923	75,163,53	72,509	68,080	75,197	72,513	68,135

investigated shapes there are only two unique principal axis for each ellipsoid shape. For the prolate, we have $E_{22} = E_{33}$, $\nu_{12} = \nu_{13}$, $\nu_{21} = \nu_{31}$ and $\nu_{23} = \nu_{32}$ which yields $G_{12} = G_{13}$. For the oblate, $E_{11} = E_{33}$, $\nu_{12} = \nu_{32}$, $\nu_{13} = \nu_{31}$ and $\nu_{21} = \nu_{23}$ which yields $G_{12} = G_{23}$. This means RVEs with a single, centered spheroid void has 5 unique constants in its compliance matrix.

The damage related to the void may be evaluated as the decrease in Young's Modulus compared to the fully dense RVE [170]. The damage D in percent is expressed as,

$$D = (1 - \frac{E_p}{E_0})100\%. \tag{117}$$

Which translates to the stress-strain relationship for the voided RVE,

$$\varepsilon_p = \frac{\sigma_p}{E_0(1-D)}. \tag{118}$$

Using Eq. (117) the damage in direction 1 and 2 (x and y) is calculated. The results are shown in Fig. 39. Damage in direction 3 (D_{33}) is not shown in Fig. 39 as it is is equal to D_{22} for the prolate spheroid and D_{11} for the oblate spheroid.

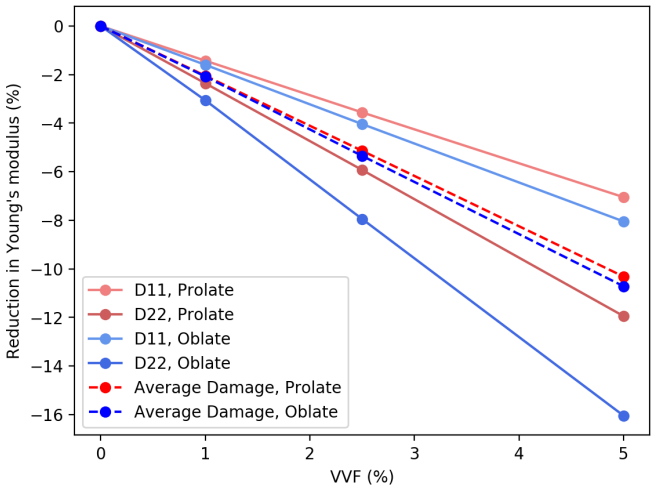

Figure 39: Damage for RVE's with different type of void shapes.

8.4.4 Discussion, RVE with Single Spheroidal Void

The evidence suggests that even as the volume fraction of each void is equal, the oblate ellipsoid gives the highest damage. This translates to the scenario described in Fig. 40. The cause of this is likely the fact that the cross-sectional area is reduced more for the oblate ellipsoid. For example, for the RVE in Fig. 40b the RVE with oblate spheroid has 75 % cross-sectional area compared to the RVE in Fig. 40a. This is independent of the applied VVF. The average damage found in each shape, however, is seen to be approximately equal. Thus, one can assume the VVF to be the primary factor in applications where void shape and orientations are highly heterogeneous. If the voids have a preferred orientation with respect to shape, the material is likely more anisotropic.

Further it is seen that the damage increases approximately linearly with the VVF for all principal directions. This means that for a spheroid of aspect ratio, $\alpha = 0.5$ as described above. The average reduction in Young's modulus may be approximated by a linear relationship such as Eq. (107). For this equation we have $c_1 = 1.86$ for the prolate spheroid and $c_1 = 1.91$ for the oblate spheroid. A c_1 around 2 is also seen in some experimental studies [161]. For Eq. (107) There is a theoretical prediction for the constant c_1 for $p \leq 0.05$ [163],

$$c_1 = \frac{1}{18}(29 + 11\nu_0). \tag{119}$$

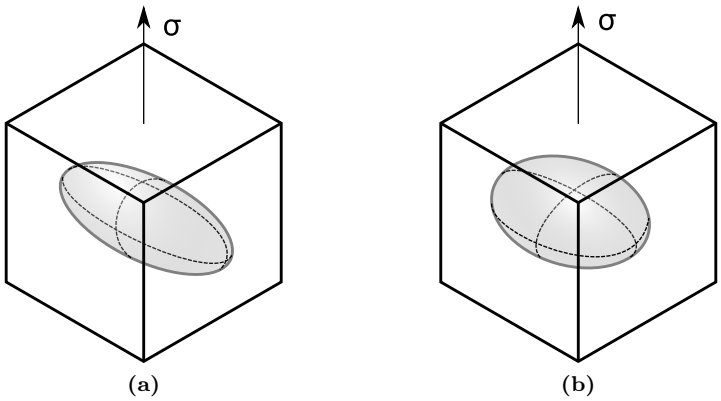

Figure 40: Void inclusion in RVE. (a) has lower damage than (b) in the loaded direction.

Where ν_0 is the Poisson's ratio of the dense material, for $\nu_0 = 0.3$ as is employed in this investigation, the prediction yields $c_1 = 1.794$, which is very much comparable to that found through the numerical investigation.

As far as the practicality of the RVE approach, it could be said that by using EasyPBC [158] to calculate the elastic properties, the procedure is relatively straight forward and quick. However, still perhaps more time-consuming than analytical approaches which also provide accurate results [169]. For cases where the voids are of substantial size, and irregular shapes, a multiscale approach, where RVEs of this type are placed within a larger body, could be a helpful tool in predicting elastic properties.

It should also be mentioned that void modeling is perhaps not sufficient as the elastic properties may also be affected by other factors induced by the manufacturing process. What is found in this section is considered, and further discussed in Section 10.

9 Experimental Work

In this section, a static test of AM produced 316L steel is described. Solberg et al. [171] investigated the fatigue behavior of the same material. This investigation concerns the elastic and plastic behavior. The material shows unusual tensile strength behavior, which is attributed to the high amount of porosity and lack of fusion defects. The testing procedure is described in detail. The results are fitted to a Voce model, Power-law, and GTN model. A discussion on the validity of the results and observations concludes this section.

9.1 Geometry

The tests were performed on three specimens of identical dog-bone geometry corresponding to ASTM E466-15 [172]. The geometry is described in Fig. 41.

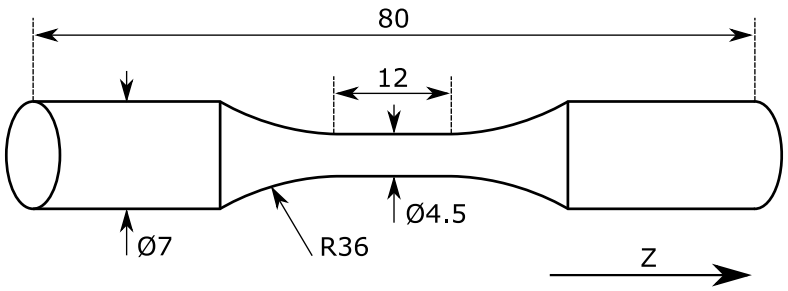

Figure 41: Test specimen geometry, values in millimeters

9.2 Printing Parameters

Table 8: Printing parameters used in the tested specimens

t, (μm)	h, (μm)	v, $(^{mm}/_{s})$	t, (W)	E_d, $(^{W}/_{mm^3})$
50	100	2400	320	26.7

The hatch style for the inside is of continuous style with an alternation of 90 degrees for each layer. A contour consisting of three circumferential scans are also utilized. The build direction is parallel to the loading direction. Additional process parameters are found in Table 8. A detailed description of the material is found in Ref. [171]. The Energy density, (E_d) is calculated using Eq. (1).

9.3 Methodology

The surface of the specimens was manually polished using sandpaper in order to create a surface for the strain gauges. The surface was not polished completely smooth. Residual dust from the polishing was removed using ethanol. Strain gauges from Tokyo Measuring Instruments were carefully attached using a strong adhesive. The wires were separated sufficiently to avoid

an eventual short circuit. Tensile tests were performed using a servohydraulic MTS system with a 50 kN load cell. The applied displacement rate was 0.2 $^{\text{mm}}/_{\text{min}}$ for all specimens. Room temperature remained at 25°C.

The three specimens were given number identifications as 21, 22, and 23. These labels may be used to correlate fracture surfaces and stress-strain curves if significant differences are observed. The strain gauges detach at a certain point in the loading process. After this, the data is not usable. The relevant regime for the Strain Gauge data is therefore limited.

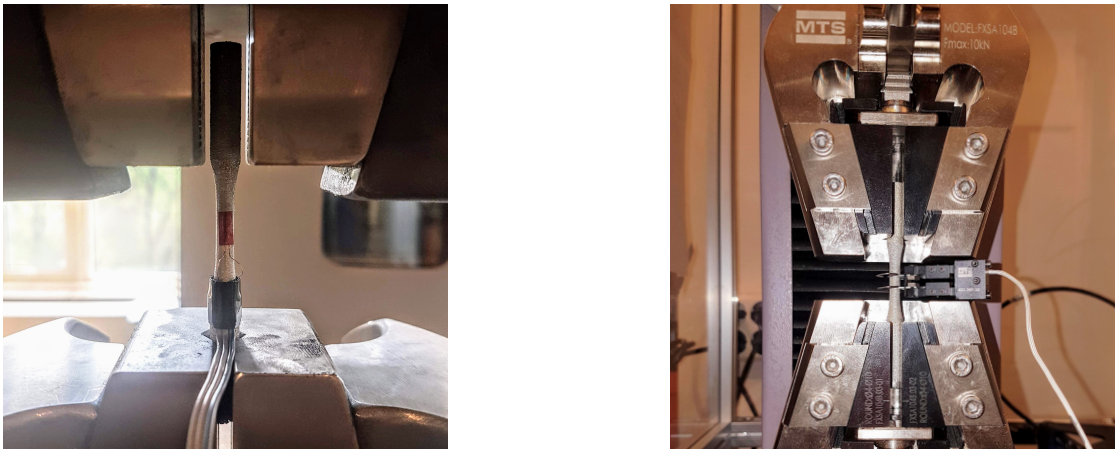

(a) **(b)**

Figure 42: (a) Tensile tests until failure using strain gauges. (b) Tensile test using extensometer at low strain.

A fourth sample was tested using an extensometer. This was done to validate the result from the strain gauges. This test was only performed for a low strain ($\varepsilon = 0.0035$). The extensometer was carefully attached to the thinnest part of the specimen before loading was initiated.

For correlating the curve fits with the experimental data, a simple difference calculation was done. For a given value of strain, stress was measured for the fit and the experimental data. The total agreement is given by,

$$Agreement = \left(1 - \frac{1}{N}\sum_{i=1}^{N}\left|\frac{\sigma_{exp}^{i} - \sigma_{num}^{i}}{\sigma_{exp}^{i}}\right|\right) 100\%. \tag{120}$$

9.4 Results From Static Test

The material shows ductile behavior. The stress-strain relationship is highly non-linear, and thus, there is no definitive Young's module or specific yield point. From SEM images of the fracture surface, and observation during the test, it is apparent that because of the highly porous and defected inside, local yielding initiates at an extremely early stage. As the specimen yields locally, voids may grow and nucleate in the center, furthering the local yielding inside. After a certain stress level, the increase in stress is slowed but keeps increasing until the highest engineering stress recorded is reached. The recorded UTS is approximately 437 MPa. At this point, the fracture

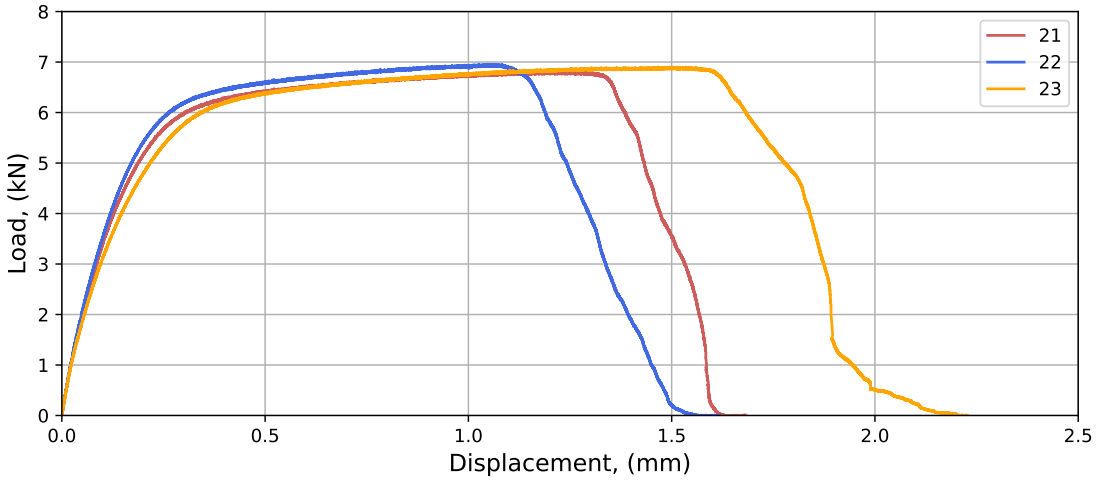

Figure 43: Load displacement data from static test.

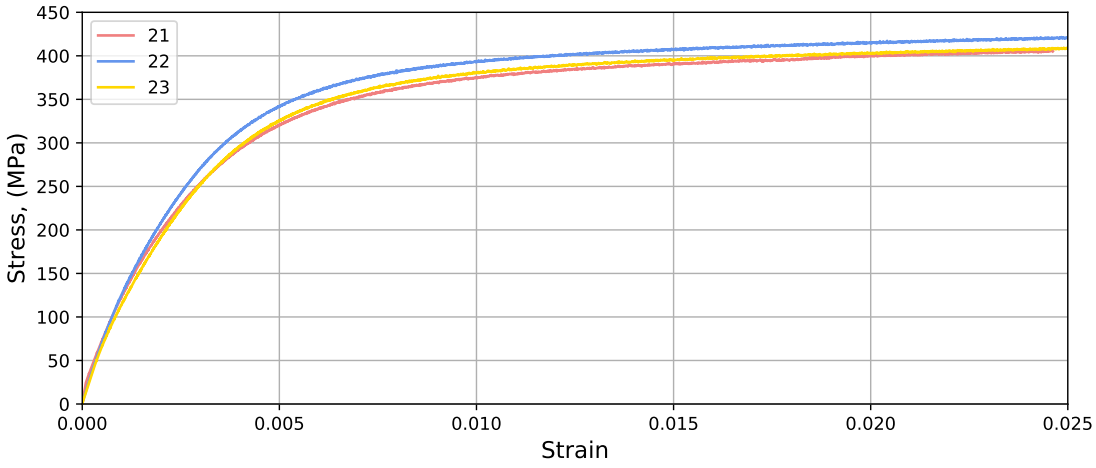

Figure 44: Stress-strain relationship recorded by the strain gauges. The data is limited to the initial part of loading.

of the contour initiates. The material shows an extremely ductile fracture process, attributed to the contours ability to stretch further due to the lack of defects in this region.

The onset of plasticity has been estimated using the offset yield strength. The strain gauge data from specimen 22 was used to estimate this value. The initial linear portion is observed to be approximately $\varepsilon \leq 0.001$, by constructing a line from the origin to the stress at this value (125 MPa), and further offsetting this straight line to intersect $\varepsilon = 0.002$, an offset yield strength is estimated to be approximately 350 MPa. For the remainder of this section, this value is utilized as the onset of plasticity.

In order to obtain a stress-strain relationship for the entire test, the load-displacement curves in Fig. 43 has been corrected for stress and strain by forcing equality in the region where strain

gauges are recording correctly ($\varepsilon \leq 0.025$). Hence the assumption is that strain gauges only capture small deformations accurately, and a correction based on the initial slope of the strain gauges are made. In tensile tests some uncertainty is to be expected [173, 174]. By force-fitting the load-displacement data by multiplying displacement with a factor of 0.027, an acceptable correlation between the strain gauge data and load-displacement data is achieved. This gives that the material should fail at approximately 3-4.2 % elongation. The resulting stress-strain data is given in Fig. 45. The validity of the purposed Stress-strain relationship is discussed in Section 9.11. These values are used for curve fitting in the following sections.

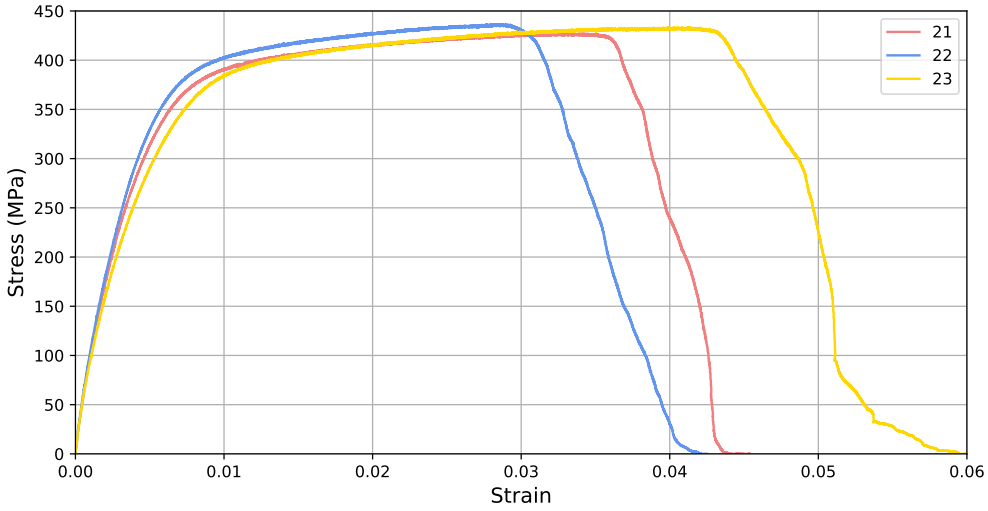

Figure 45: Corrected Stress-Strain Curve used for modeling plasticity.

From plotting time versus strain, information as to how constant the strain rate remained throughout the tests is obtained. The values used for strain are those directly achieved from the strain gauge (Fig. 44). From Fig. 46 it is apparent that the strain rate has indeed not remained constant throughout the testing regime for the region where strain gauges were attached. It is also observed that there is some lack of continuity for the first two specimens, whereas specimen 23 remains continuous throughout. The cause of this may be the loosening of strain gauges after the deformations become sufficiently large. To estimate the strain rate of these samples the values for test specimen 23 are used, after 120 s, with the following relation of derivative,

$$\dot{\varepsilon} = \frac{\varepsilon_2 - \varepsilon_1}{t_2 - t_1}. \tag{121}$$

The resulting strain rate is estimated to be approximately $0.003\,32\,\mathrm{s}^{-1}$ for the plastic part.

9.5 Young's Modulus

There has been an attempt to estimate Young's modulus of the material. Note that this is a crude approximation, as the elastic part is practically non-existent for the material in question. However, for an FEA, there needs to be established elastic properties for the material.

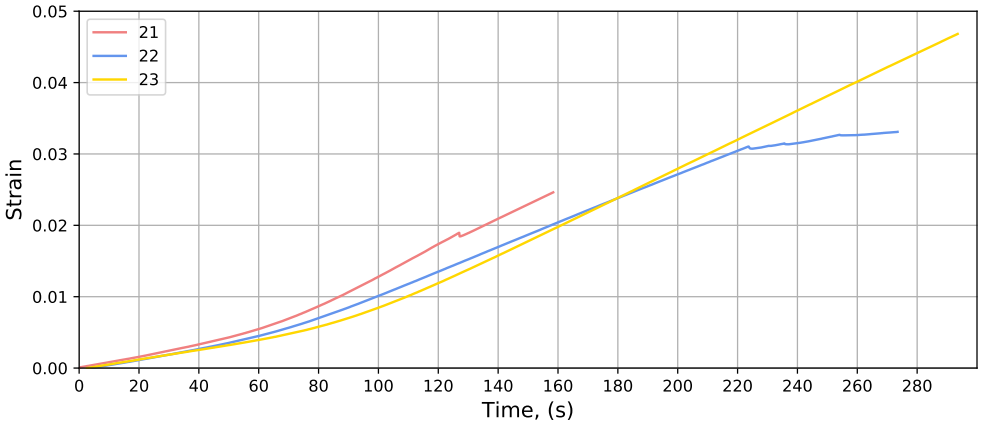

Figure 46: Time versus strain plot for the strain gauge data.

Three Young's moduli have been estimated. By, $\sigma = E\varepsilon$, for the strain gauge data. $E_1 = 64.6GPa$ is obtained, by drawing a linear line from the origin to the suggested yield point, $\sigma_y = 350MPa$ at $\varepsilon = 0.0054$, (see Fig. 47a). For the extensometer data the same approach, be it for the latest recorded point at the stress-strain curve, gives $E_2 = 77.6GPa$. A least-square fit for the part exhibiting the most linear behavior in the extensometer data gives, $E_3 = 58.5GPa$, (See Fig. 47b). The results are shown in Table 9.

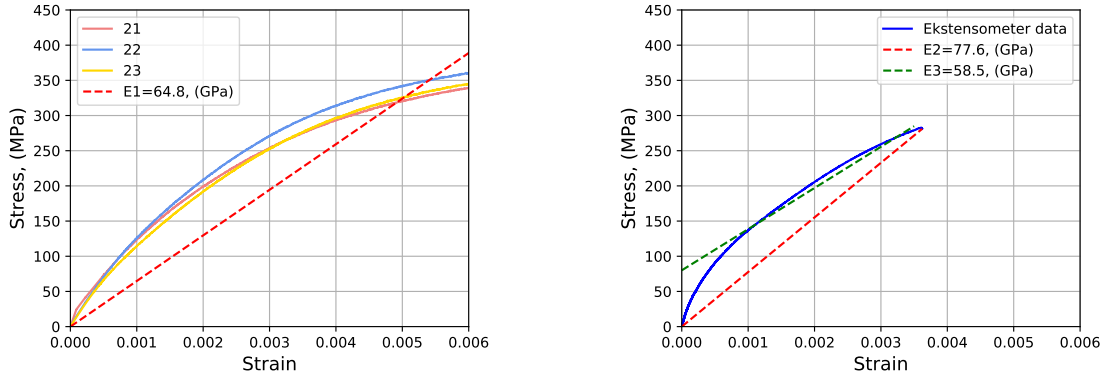

(a) **(b)**

Figure 47: Young's modulus fit (a) for the region before the defined yield point using strain gauge data. (b) using extensometer data.

Table 9: Young's modulus estimations.

E_1, (GPa)	E_2, (GPa)	E_3, (GPa)
64.8	77.6	58.5

The above estimation of Young's modulus does not show an ideal estimation. The highly porous

material is too non-linear as a result of a large number of porosities. Similar observations regarding the lack of linear elastic response at low stresses for SLM produced 316L are found in another study [82]. The suggested Young's moduli are given to provide an estimate of the strength of the material, but mostly to enable the material to be implemented in FEA. For a simulation of the material, E_1 should be utilized to achieve a realistic onset of yield in the simulation.

9.6 Johnson-Cook Parameters for Plasticity

Because the material is so highly ductile, the onset of plasticity is hard to define. The yield strength of 350 MPa is used for this investigation. The data is then shifted such that the plastic strain starts at 0 with the stress of 350 MPa. A simplified variation of the JC expression, seen in Eq. (52) is employed. As specimens are only tested for one temperature and one strain rate, i.e., the strain rate is equal to the reference strain rate the two latter terms are disregarded. Thus the JC expression is reduced to a simple power-law,

$$\sigma = [A + B\varepsilon_p^n]. \tag{122}$$

A python script is used for finding the optimal constants; the regression method used is the default built-in least square method in SciPy [175]. The best-fit power-law parameters for specimen 22 are given in Table 10. The power-law achieves a reasonable fit for the plastic behavior of the material. For a FEA of AM produced 316L steel, these parameters may be used for a decent behavior prediction of the elastic regime.

Table 10: Parameters used for Power law curve fitting of plastic part of tensile data using Eq. (122)

Specimen	A, (MPa)	B	n	Agreement, (%)
22	350	340.33	0.35238	99.4

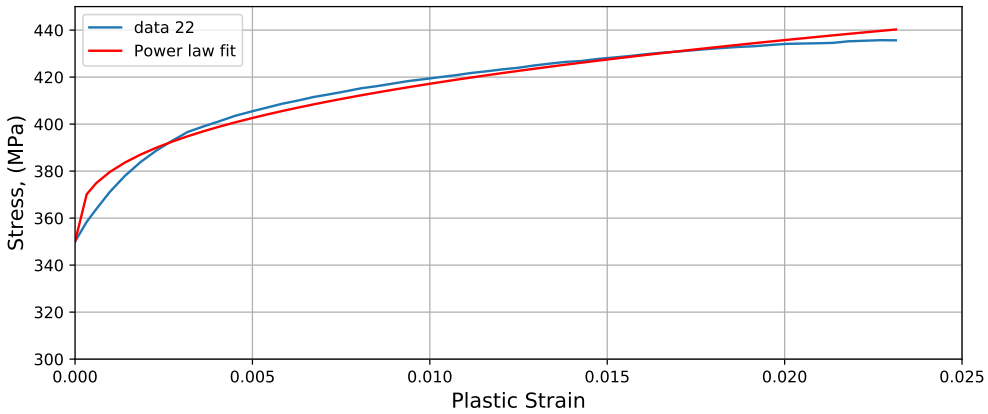

Figure 48: Curve fit for plastic stress-strain for specimen 22 up until fracture, using Eq. (122)

9.7 Voce Model Parameters for Engineering Stress-Strain

The curves in Fig. 44 Have not been corrected to true stress and true strain. The reduction in area at the "neck" of the specimens is not significantly large, this is due to the initiating fracture of the inside and the stronger outer contour being able to withstand more stress. Such one can say that the outer surface does not change significantly during increased loading, even as the cross-sectional area is reduced as the inside deteriorates. For another simplification of the material behavior, one may model the material behavior as a linear viscous dash-pot, also referred to as the Voce-model [176],

$$\sigma = T\left(1 - e^{-\frac{\varepsilon}{h}}\right). \tag{123}$$

By attempting to fit this curve to the data pre-fracture, a very good fit is achieved for the first part of the curve, and a reasonable one for the latter part, see Fig. 49. The optimal parameters for the fit using Eq. (123) and the corresponding agreement using Eq. (120) in percentage are given in Table 11. The agreement is calculated to be lower than for the power-law fit. A 95 % agreement is still acceptable considering this is for a larger spectrum of stress-strain values than only for the plastic part.

Table 11: Parameters used for exponent curve fitting of tensile data using Eq. (123).

Specimen	T	h	Tot. Agreement, (%)	Pl. Agreement, (%)	El. Agreement, (%)
22	430.11	0.00355	95.84	90.32	99.02

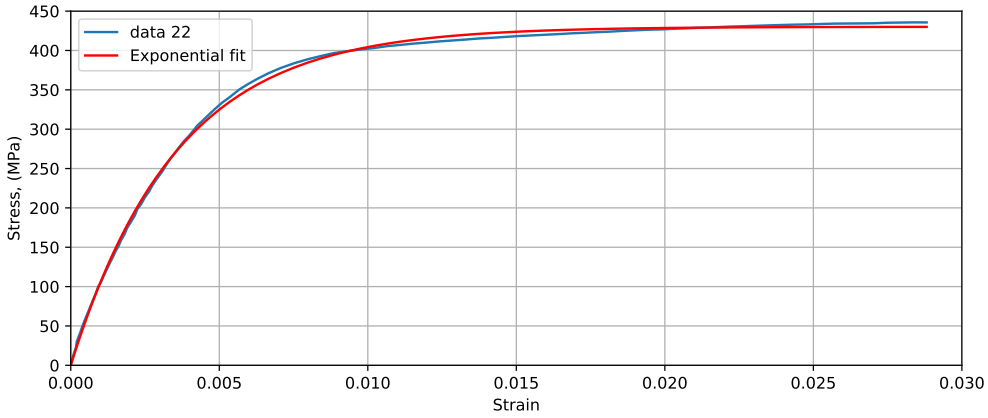

Figure 49: Curve fit for engineering stress-strain for specimen 22 up until fracture, using a Voce model, Eq. (123).

This model could be used as a function for modeling materials with lacking linearity, but results in a perfect plasticity type situation as the function reaches an asymptote towards the T value. The model is commonly used to describe polymers but is rarely used for metals, although it is reported to be reasonable for ductile metals such as Aluminium alloys [40, Chapter 4]. For FEA of specific applications, this model may be used in cooperation with some fracture description. The suitability is still questionable as the material behavior recorded in these tests could be

heavily dependant on the contour and matrix defects, which can produce a high variance in results.

9.8 GTN-Model Application

The GTN-model earlier discussed in Sections 5.8 and 7 is more complicated to implement for the experimental data. First, some plastic properties for a reference fully dense material need to be established. JC parameters for 316L from 4 sources are presented by Umbrello et al. [177], here the values from Tousini et al. [178] are giving accurate results in the context of machining FEA. Chandreskan et al. [179] also evaluated JC parameters for AISI 316L steel and achieved two sets of parameters. The first set was obtained using a continuous chip model, the second with a chip serration model for strain and strain rate. JC parameters obtained in these studies are found in Table 12. Stress-strain data for fully dense 316L due to Falkowska et al. [154] is found in Section 7.

Table 12: Johnson-Cook material parameters for dense 316L [177].

Ref.	E, (GPa)	A	B	C	n	m	$\dot{\varepsilon_0}$, (s^{-1})	T,(°C)
[178]	210.3	514	514	0.042	0.508	0.533	0.001	20
[179] (1)	210.3	305	1161	0.01	0.61	0.517	1	20
[179] (2)	210.3	305	441	0.057	0.1	1.041	1	20
This work	64.8	350	108.55	-	0.32755	-	0.003	25

Incorporating strain rate dependence of the material was of interest, however, as the GTN model may only be used with Abaqus [97] explicit, the time-step is dependant on the most critical elements. Trying to run the same strain rate as the tensile tests performed for this study, therefore, required far too many steps for it to be feasible with the available computational power. As a simplification, the hardening was therefore assumed to be strain rate in-dependant.

CT-scans performed for the same material subject to the present investigation are presented in Ref. [171]. CT-scans revealed an initial VVF of approximately 5.4 %. However, as the mechanical properties are so heavily reduced compared to other studies on the same material [81, 82], it is a reason to believe that the actual porosity may be significantly higher. At least, the GTN model would require a higher initial VVF than 5.4 % in order to achieve an accurate fit. Using the preliminary parameter study in Section 7, reasonable Void-constants for the GTN model are estimated.

For this investigation, the setup remained the same as in Section 7.5. With a difference in geometry and elements. The geometry was reduced to a single cylindrical specimen with radius 2.25 mm and length of 12 mm, i.e., the middle section of the geometry described in Fig. 41. The model was meshed with 320 axial elements of the type CAX4R.

There has been performed analysis using GTN of all four reference materials (Table 12 and 26a). The plasticity described by Tousini et al. [178] gave the most accurate results. From Abaqus the Plastic Equivalent Strain (PEEQ) is plotted against σ_{eq}. The resulting stress-strain relationship of the GTN model is compared to the experimental results in Fig. 51. GTN constants for the analysis are found in Table. 13.

The volume fraction of void nucleating particles, f_N, is estimated for AM produced austenitic stainless steel as 0.012 for steels with a Initial VVF of 0.034 [180]. An estimated f_N for this

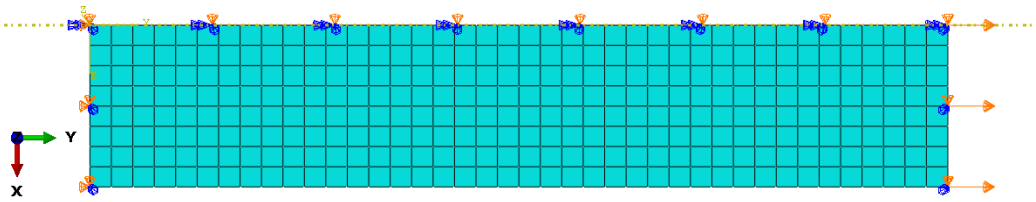

Figure 50: Mesh and boundary conditions.

Table 13: GTN parameters used to model the most conservative specimen.

E, (GPa)	ν	q_1	q_2	q_3	ε_m	S_n	f_N	f_f	f_c	f_0
64.8	0.3	1.6	1	2.56	0.3	0.1	0.02	0.2144	0.1774	0.1750

material is thought to be slightly higher. Thus, $f_N = 0.02$ is chosen for this analysis, although the GTN analysis does not allow Void nucleation to play a significant role as the VVF is not to reach high values. Fig. 52 shows the distribution and evolution of VVF in the Abaqus simulation; grey color signals failed elements.

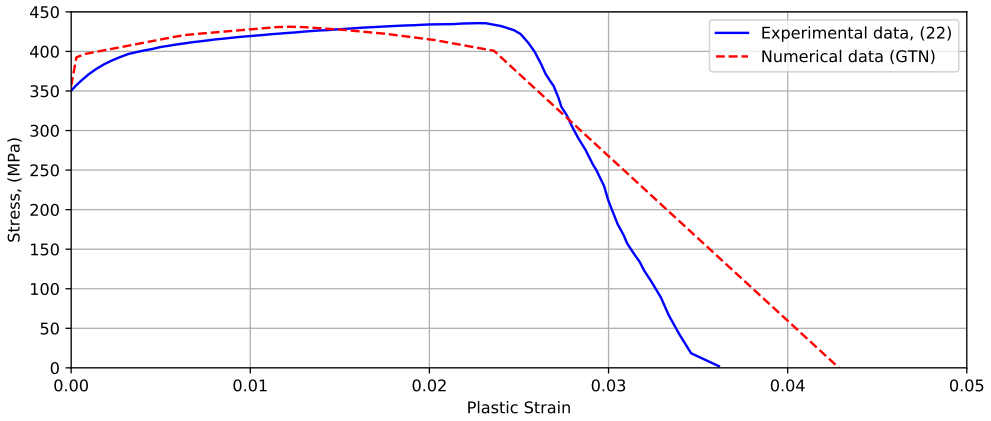

Figure 51: Best obtained GTN model fit for plastic part of specimen 22. Using JC-plasticity data obtained by Tousini et al. [178].

9.9 Stress Distribution in Test Specimen

There has been performed a simple stress distribution analysis on the geometry of the specimen. Abaqus [97] was used to model the geometry described in Fig. 41. One end was fixed in all directions, while the other end was applied a forced displacement of 2 mm. The material was defined as elastic with arbitrarily chosen E-module, (200 GPa) and Poisson's ratio, (0.3). Static, General analysis shows the stress distribution of the strained geometry. The stress is plotted along an edge path of the entire section, where the diameter is less than 7 mm. Fig. 53 shows the stress as a percentage of the highest stress recorded. One can expect the stress at the end of the narrowed area to be roughly 40% that of the uniform middle section.

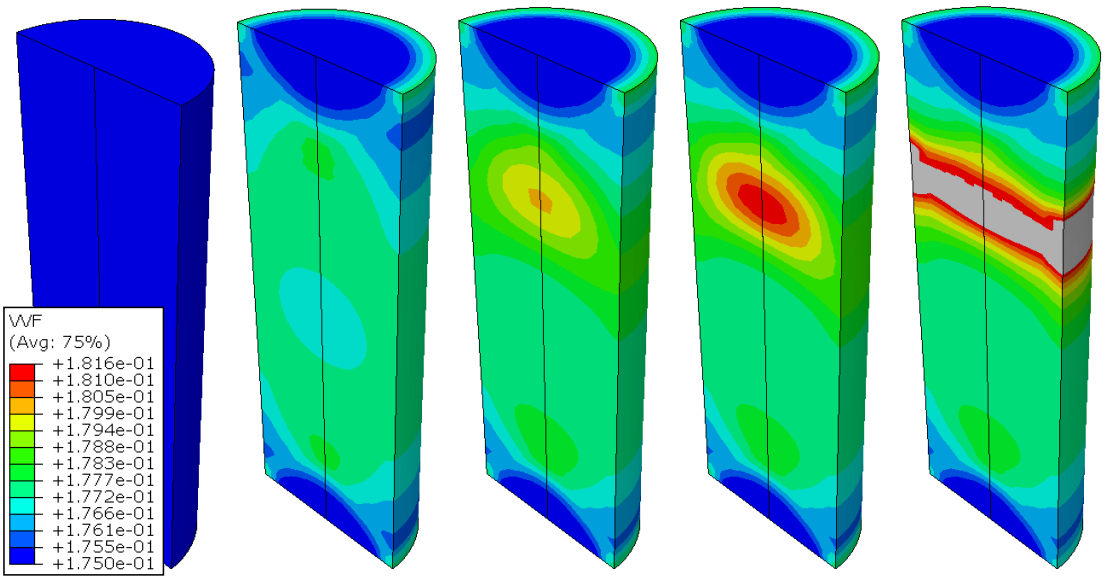

Figure 52: VVF distribution and evolution in Abaqus simulation. The model is of axial elements revolved 180 degrees.

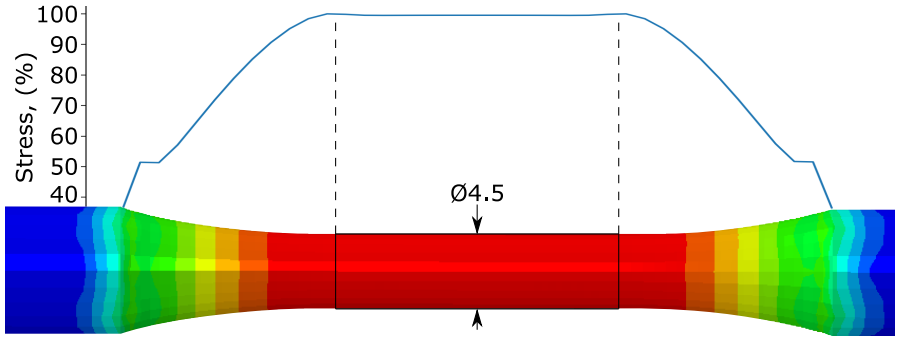

Figure 53: Stress distribution over narrowed section. The von Mises stress is measured along the path of the surface elements and the maximum value is used to evaluate the percentage.

This may be sufficient to cause local yielding in this region, resulting in the assumption that deformation does not happen exclusively over the thinnest part of the specimen. A significant amount of strain in this region makes correcting the load-displacement data to fit the strain gauge data a difficult task. Strain recorded for the strain gauge may not be comparable to the strain of the entire geometry. Using the entire length of the narrowed part (30.4 mm) will also not be accurate.

9.10 Analysis of Fracture Surface

The fracture surfaces of two of the specimens, 21 and 23, were observed using Scanning Electron Microscope (SEM). The results are shown in Fig. 54. The low magnification image (Fig. 54a) clearly shows the difference between the contour and inside of the specimen. While the contour

remains "constant" post-fracture, the inside shows a large cavity resulting from evolving voids in the matrix. Red arrows indicate unmelted particles of various sizes in Fig. 54b. These unmelted particles are likely to act as void nucleation sites. The specimen shows small dimpled structures on the fracture surface. These are visible in Fig. 54c and 54d. The dimples correspond to the typical behavior of ductile fracture as a result of tensile overloading, leading to void nucleations in the material [40]. The dimples are small, (approximately 1 µm), which is comparable to other studies on the same material [82], but smaller than that observed with the same material manufactured through other methods [181]. Some brittle fracture surfaces are present. These may be attributed to the sheet mechanism illustrated in Fig. 21. Significantly sized voids are observed, likely as a result of a lack of fusion resulting from poor printing parameters. In Fig. 54e and 54f a rather large void is seen with unmelted particles inside, in agreement with observations made in other studies [84, 182].

Zhong et al. [182], suggested the size of the dimples observed on the fracture surface, to be attributed to the size of intergranular cells in the built material. Process parameters during manufacturing affect this size.

Considering the high amount of voids and defects present, the material is able to withstand a relatively high amount of stress. The high number of defects observed in the material is the likely cause of the three specimens fracturing at different strains, and the lack of definitive linear-elastic portion of the stress-strain curves. The heterogeneity in microstructure cause failure prediction to be challenging.

9.11 Discussion and Comparison

The 316L stainless steel presented in the previous sections shows a significantly lower strength performance than that of other studies. In a comprehensive study of the tensile strength of SLM produced stainless steel by Qiu et al. [81], the initial stress-strain response is much more linear and steeper than that observed in the present work. Ultimate tensile strength is also merely 60 % of that presented by Qiu et al. [81]. It is thereby confirmed that the printing parameters are significantly affecting the strength. A large number of defects in the tested material cause yielding at an early stage

Previously, in Section 8.1 Young's modulus of porous media was investigated. If we assume a linear relationship between porosity and Young's modulus as in Eq. (107) for the samples investigated above, with assuming the dense material's Young's Modulus as that reported by Falkowska et al. [154] ($E_0 = 196.2$), and porosity content as that evaluated from CT scans for the same material [171] ($p = 0.05$). The resulting constant is, $C_1 = 14.03$ for E_3 and $C_1 = 12.09$ for E_2 which is 7 and 6 times the reported common values for c_1 respectively. Thus, it is suggested that either the porosity-content is much higher than that observed through the CT scans, or that other factors reduce the Youngs modulus. Voids of low sphericity are observed in the material [171]. These voids cause local plasticity at an earlier stage than spherical ones if oriented perpendicular to the loading direction. A large number of this type of voids may be the reason for the extremely reduced Young's modulus.

A comment on the validity of the corrected stress-strain relationship seen in Fig. 45 is required. During the work of factoring the load-displacement curve to achieve engineering stress-strain, the conventional displacement-strain relationship in Eq. (124) was attempted.

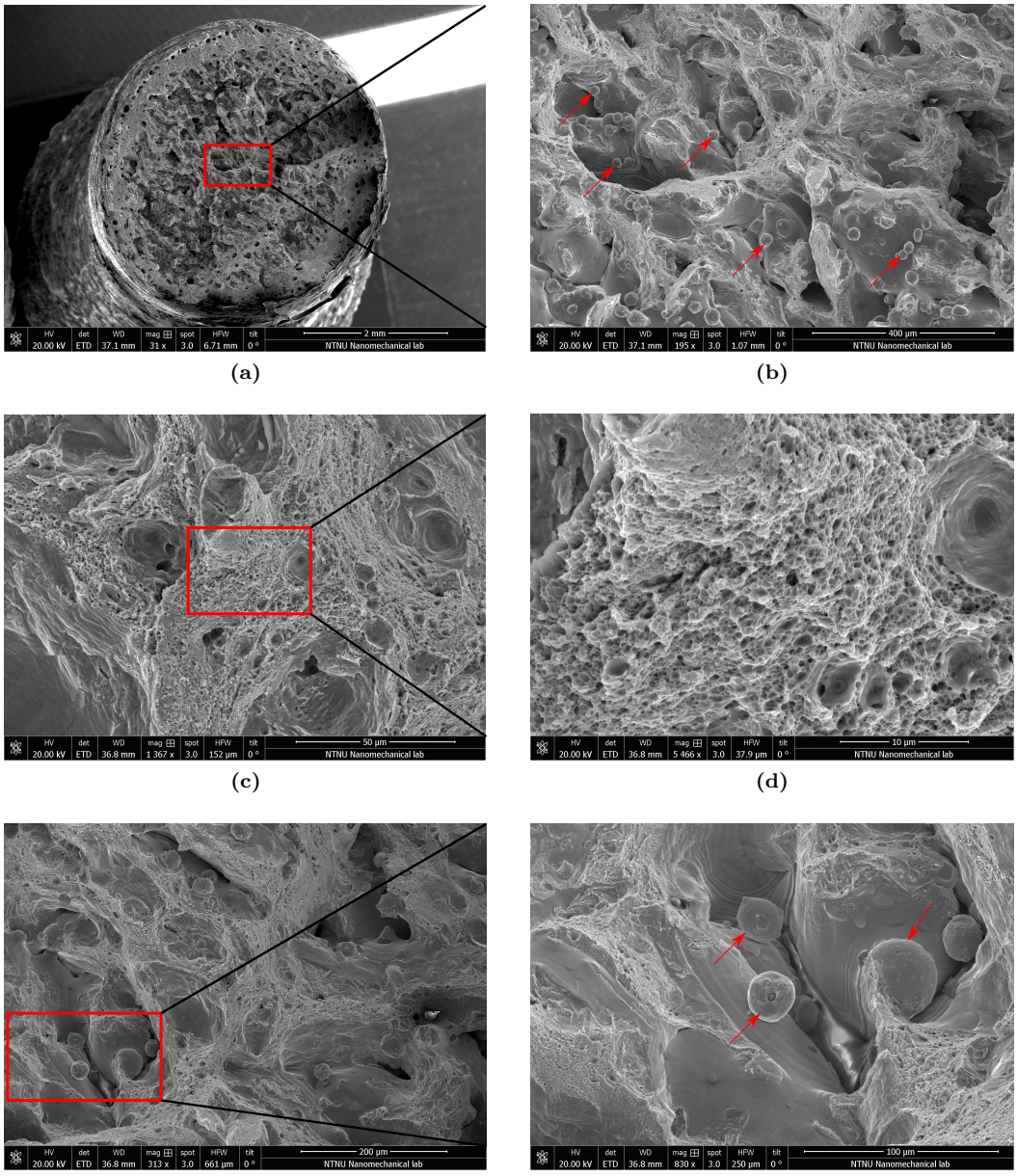

Figure 54: SEM micrographs of fracture surface in tensile tested specimen. (a) Low magnification of fracture surface. (b) Unmelted particles are present throughout the entirety of the surface. (c) and (d) dimpled structure characteristic of ductile fracture. (e) and (f), larger void (200 μm) void containing unmelted particles.

$$\varepsilon = \frac{l - l_0}{l_0}. \tag{124}$$

However, by using $l_0 = 12\,mm$ (Fig. 41) the data from Fig. 44 is vastly different, thus it is assumed that the deforming region of the test specimens must be greater than the thin part of the dogbone, as discussed in Section 9.9. The value of $l_0 = 30.8$, i.e., the distance of the narrowed section, gives more reasonable results corresponding to percent elongation at failure between 5 and 3%. However, the corrected curve still deviated significantly from the Strain gauge data. It is reasonable to question the quality of tensile tests performed on this geometry, as even using the cross-sectional diameter of 4.5 mm for calculating stress, may be faulted. Due to the high number of porosities and the hatch contour, the stress is thought to be distributed unevenly throughout the cross-section. Future investigations could be improved if a geometry more suited for tensile tests are utilized. Alternatively, more sophisticated methods for measurements of strain could be attempted. By probing strain gauges at different points on the specimen the strain distribution could be more accurately predicted.

A true stress-strain relationship for the material was a topic of interest; however, as the contour remains intact until complete failure initiates, the reduction in area is hard to define.

As for the GTN model fit, there is achieved an acceptable correlation between experimental data. However, as the analysis assumes a uniform distribution of voids, and a homogeneous material, the data must be interpreted with caution. The contour is assumed to serve as a significant part of the load-bearing in the specimens, leading the cross-section to be non-uniform. The current analysis does not capture this. Further, the previously described problem regarding stress distribution may cause the Void Parameters in the applied GTN model not to represent the actual case of the material. There is also reason to doubt the result from the part of the Numerical data similar to that of ductile fracture. No ductile fracture criterion is applied to Abaqus, leading this part of the curve to be heavily time-step dependant. Zhang et al. [124] purposed a method for incorporating ductile fracture in the GTN model. Further investigation of AM produced ductile metals, could evaluate the ductile fracture process much more accurately and reliably than here.

A more fruitful estimation for the GTN parameters of the material in question could be made with a different specimen geometry or machining the specimens to obtain a more uniform cross-section. This would likely provide more reproducible results, which can be used to estimate optimal GTN parameters for AM produced materials. That could further the research towards a complete PPMM model.

As described in Section 4, the yield strength and the UTS of AM produced materials are often higher than with other manufacturing methods. For the application of the GTN-model, the "dense" material properties required to evaluate reduced strength should be the material produced by AM that provides a minuscule amount of porosities. The Johnson-Cook parameters utilized in this discussion may not be a legitimate approach. It must be stressed that the primary goal of the investigation was not to find correct properties, but rather explore the possibilities related to utilizing the GTN-model for AM produced materials.

10 Final Discussion and Summary

In this thesis, a set of material models have been reviewed and summarized. These are valuable tools for accurately describing material properties. For applications to AM, the Mori Tanaka scheme and GTN model may be best suited for generalizing the strength of AM materials due to their semi-analytical nature, and that they account for void behavior in the material, which is a significant defect seen in AM materials. Combining these semi-analytical methods for a strength prediction scheme by linking process parameters to a probabilistic expected amount of porosity, one can evaluate the expected strength of the material. Considerable work is needed in order to achieve this relation as there are a significant amount of parameters influencing the properties of materials produced by AM.

In Section 8.4, the elastic properties of a single void in a unit cube was investigated. PBC are applied to a RVE, and an anisotropic compliance matrix is achieved. Although this study only investigated two void configurations, the procedure presented is relatively simple. The anisotropy of AM-produced materials could be estimated through this procedure. The Young's Modulus is shown to be reduced when flattened voids are perpendicular to the loading direction. To evaluate if this behavior is represented, in the same degree, in AM produced materials as with a modeled RVE, is left for future work.

The phenomenological equations for Young's modulus estimations listed in Section 8.1, could also be incorporated in AM materials. However, it may be necessary to incorporate more material constants, which can represent the observed inhomogeneity in microstructure, causing anisotropic behavior in AM produced materials. A simple suggestion which can be subject for future work is to assume Anisotropy and Young's modulus in the form of,

$$E_z = c_z f(E_0, p) \;\; and \;\; E_{xy} = c_{xy} f(E_0, p) \tag{125}$$

Where c_z and c_{xy} represents constants, and f is a function which represents the reduction in Young's modulus, E_0 and p are solid material young's modulus and porosity respectively. The anisotropy in yield and elongation could be modeled through similar phenomenological models. This could provide rough estimations in the build direction, z, and parallel to layers xy. Further investigations of the effect of process parameters on Young's modulus are encouraged.

It is suggested that the modeling of AM produced materials should separate elastic properties and plastic properties. Of course, these properties are inevitably linked, and factors influencing yield and plasticity will also affect the elastic properties. Still, since sub-optimal process parameters may severely reduce Young's modulus, a behavior model accurately capturing this would be beneficial as many simulations of engineering applications only consider the structure's deformation in the elastic regime.

Porosities have been considered a primary factor both in terms of strength and anisotropy. This is a simplification, which has been made to limit the amount of relevant literature and give the thesis a focus. However, melt pool tracks are often attributed to the anisotropy of AM produced materials, in the way that loading perpendicular to melt tracks leads to less ductility than parallel loading.

Predicting porosities in AM produced materials have seen both analytical and experimental attention [27, 28, 151]. It is suggested that the prediction of voids attributed to lack of fusion could be linked with the prediction of strength in the GTN model. This could be the starting point of a constitutive relationship between process parameters and mechanical properties. If

the plastic potential resulting from combining the predicted relative density of Tang et al. [28] and the GTN model (or MT-model) fits the trends observed in AM produced materials is a field of great interest, and should perhaps have been pursued in this thesis. Still, some discrepancy between the predicted onset of yield by the GTN model and experimental results were showed for highly porous metals (Section 7.8). However, the porosities in AM produced materials rarely achieve such high porosities. Thus the GTN model is still considered a tool that should be investigated on AM produced materials more thoroughly.

While on the topic of implementation of the GTN model it should be emphasized that, in this thesis, obtaining parameters was done by trial and error, by making qualified guesses, and iterating until the desired behavior was achieved. This is not a recommended procedure. For future investigations, a table of suggested parameters should be made before implementation, and all simulations carried out using an automatic simulation generator in Abaqus, e.g., a python script. By performing several systematic approaches for establishing the GTN-parameters, trends in AM produced materials porosities/void nucleating particles and GTN parameters could be observed.

A field largely overlooked in this thesis, but which could be a fruitful area for further work is that of composites. The heterogeneous structure in these materials makes them anisotropic in much of the same way. Loading parallel to fibers yields higher load-bearing capabilities. Incorporating research on modeling of Composite behavior to the anisotropy in resulting from AM could be a possibility. As an example, a tensorial based damage model for composites was developed by Matzenmiller et al. [183]. The model incorporates many aspects also relating to AM produced materials.

The foundation of the GTN model is that the high stress resulting from porosity is averaged throughout the material, and such it assumes isotropic properties. A representative set of GTN parameters may be different for AM produced materials tested in, say parallel or perpendicular to scan layers, even though the porosity content is equal. This is the main weakness of incorporating the GTN model to AM materials. This weakness could be overcome by modifying the model to account for shape and distribution in voids. Still, a degree of simplifications may be robust enough for adequate predictions.

A schematic, describing how modeling elastic-plastic properties of AM produced materials could be performed is shown in Fig. 55. It would not be fair to assume this method as satisfying without accompanying the model with extensive experimental research. It is included here as a summary of explored approaches, and suggested fields of future research. An interesting note is that if the steps in Fig. 55 is finalized, and the ability to predict material properties of AM produced materials is improved, it would be possible to perform a reverse-engineering procedure as well. I.e., determine the material properties necessary for a specific engineering application, and predict the required process parameters for achieving this material.

This work has primarily been concerned with the properties of as-built materials. Heat treatments will alter the behavior of AM produced materials drastically due to changes in microstructure. Heat treatments will indeed complicate the issue of modeling severely. Modeling the alteration of mechanical properties from heat-treatment would likely be challenging to incorporate in a complete PPMM. Still, there has been performed a significant amount of research on heat-treatment of AM produced materials, throughout the literature, and some common trends are observed. Garrett et al. [184] modeled the evolution of yield stress from solution heat-treated aluminum alloys; a similar approach could be utilized for AM produced materials.

As a concluding remark to this discussion, it could be said that modeling and prediction of

mechanical properties in AM materials are challenging primarily due to a large number of factors involved, and the considerable variation in mechanical properties. The versatility of AM produced materials is also one of the benefits of using this manufacturing method. Model selection, the number of factors, and sample size are topics that have troubled research in most scientific fields. In a 1991 paper for the Psychological Bulletin, titled *"Model selection in Covariance Structures Analysis and the "Problem" of Sample Size: A Clarification"*, Cudeck and Henly [185] writes, "Models usually are formalizations of processes that are extremely complex. It is a mistake to ignore either their limitations or their artificiality. The best that one can hope for is that some aspect of a model may be useful for description, prediction, or synthesis. The extent to which this is ultimately successful, more often than one might wish, is a matter of judgment." What is needed for the field of AM is precisely that, a model useful for description and prediction. Evaluating a large selection of models is, of course, necessary, but at some point, a model with an acceptable amount of factors, would need to be chosen, and explored thoroughly by experimental studies.

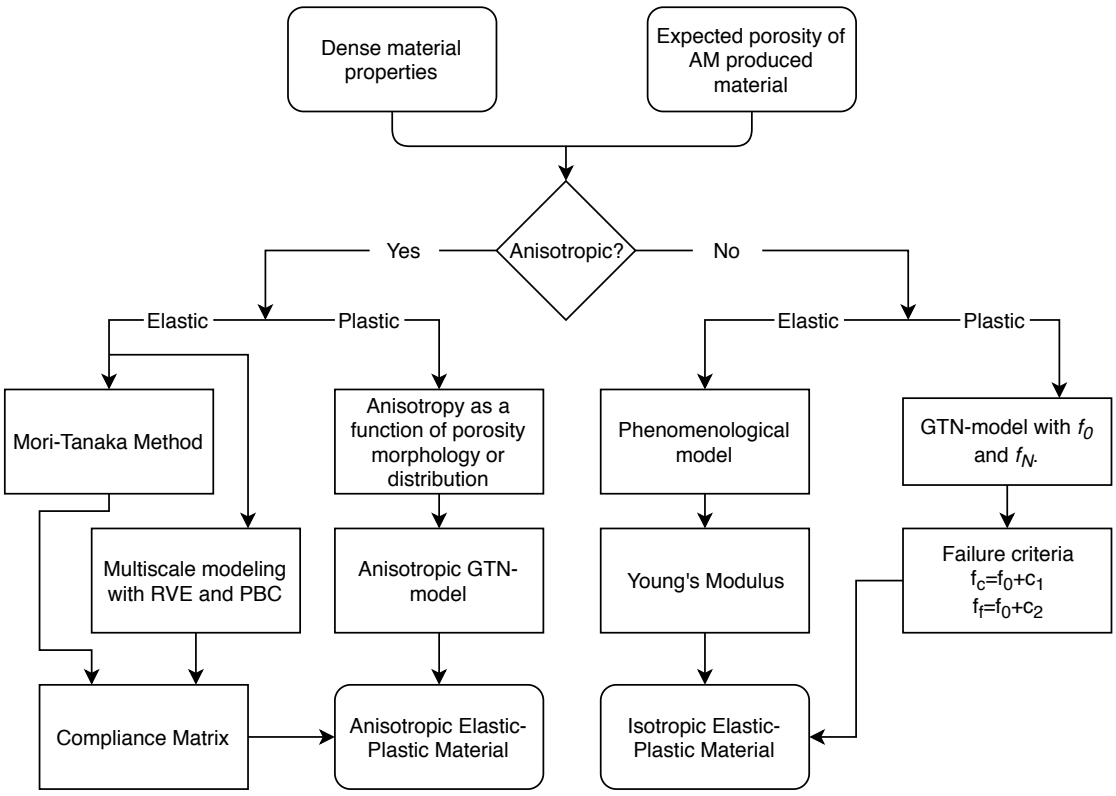

Figure 55: Schematic describing how an AM produced material could be modeled.

11 Conclusion

While the results presented in this report may not be as complete as the author would like, many different concepts in modeling of the mechanical behavior of heterogenous materials have been presented. The concepts should be further examined to achieve fully viable methods for strength prediction, and material modeling of AM produced materials. The reader should consider what has been presented in this report as an introduction to several areas, and may hopefully be inspired to further develop or investigate these concepts for an appropriate application.

The key findings are:

- Porosities is one of the main defects influencing the mechanical properties of AM produced parts. Porosities can be observed and be incorporated into the mechanical behavior prediction model.
- The GTN model is a candidate for mechanical behavior prediction of AM manufactured parts. The relevant regime for the model is plasticity. The reduced hardening due to porosities may be accurately predicted.
- The GTN model could benefit from some modifications as it tends to overestimate strength. Incorporating specific modifications suited for AM produced materials would be beneficial.
- A multiscale modeling approach for estimating Elastic properties could be beneficial for AM produced materials, as this method allows for specific modeling. The method may be time-consuming, but the large range of possible configurations makes this a valuable tool.
- High porosity content in AM produced 316L steel effectively removes any linear elastic part of a stress-strain curve, and cause plasticity to be present throughout loading, making quantification of tensile properties challenging.
- Material Models may serve as powerful engineering tools for strength prediction. An understanding of the possibilities within this field can enhance the accuracy of simulations.
- Linking Process Parameters and Mechanical behavior through a constitutive relation is a challenge that needs a significant amount of experimental and analytical investigations. If a robust model is achieved, this could aid in reducing the need for mechanical testing of AM produced components.

12 Further work

A set of specific topics that could be subject to further research is presented.

GTN model application to AM materials is merely introduced in this thesis. Evaluating how process parameters affect the constants in the constitutive model may further the possibility of incorporation of GTN in the field of AM. Are measured porosity and void nucleating particles viable parameters in the GTN model? What is the common VVF at failure, and is this value representative for the predicted failure in the GTN model?

Anisotropic behavior in AM produced materials correlated with material models. Specimens tested in different directions, could be associated with material models presented in this work to suggest a material model best suited for evaluating anisotropic elastic-plastic properties in complex stress states. How does the MT scheme compare to multiscale modeling for the elastic regime? Is it possible to determine Hill-constants for evaluating equivalent stress? Can defining Porosity morphology and distribution account for the anisotropic behavior seen in AM produced materials?

Young's Modulus and yield point prediction in AM produced materials. This can be evaluated using Equations presented in Section 8.1, but perhaps a more complex model that incorporates Process Parameters as a whole could be more robust.

Strain Rate dependence in AM produced materials is a topic that would benefit from further research. The extent at which the unique microstructure in AM materials affects strain rate is not well documented in the literature.

Combining prediction of porosity-models in AM [28, 151], and plastic potentials concerning porosities [116, 131]. Can the strength of AM produced materials be represented this way?

References

[1] W. E. Frazier. "Metal Additive Manufacturing: A Review". In: *Journal of Materials Engineering and Performance* 23.6 (2014), pp. 1917–1928. ISSN: 1059-9495 1544-1024.

[2] T. DebRoy et al. "Additive manufacturing of metallic components – Process, structure and properties". In: *Progress in Materials Science* 92 (2018), pp. 112–224. ISSN: 00796425.

[3] J. J. Lewandowski and M. Seifi. "Metal Additive Manufacturing: A Review of Mechanical Properties". In: *Annual Review of Materials Research* 46.1 (2016), pp. 151–186. ISSN: 1531-7331 1545-4118.

[4] P. Li et al. "Critical assessment of the fatigue performance of additively manufactured Ti–6Al–4V and perspective for future research". In: *International Journal of Fatigue* 85 (2016), pp. 130–143.

[5] M. Shamsujjoha et al. "High Strength and Ductility of Additively Manufactured 316L Stainless Steel Explained". In: *Metallurgical and Materials Transactions A* 49.7 (2018), pp. 3011–3027.

[6] J. Smith et al. "Linking process, structure, property, and performance for metal-based additive manufacturing: computational approaches with experimental support". In: *Computational Mechanics* 57.4 (2016), pp. 583–610. ISSN: 0178-7675.

[7] C. W. Hull. *Apparatus for production of three-dimensional objects by stereolithography.* US Patent 4,575,330. Mar. 1986.

[8] B. Berman. "3-D printing: The new industrial revolution". In: *Business Horizons* 55.2 (2012), pp. 155–162. ISSN: 00076813.

[9] I. Gibson. "Rapid prototyping: from product development to medicine and beyond". In: *Virtual and Physical Prototyping* 1.1 (2006), pp. 31–42.

[10] Web Page. 2018. URL: `https://www.materialise.com/en/cases/spider-bracket-a-topology-optimization-project-by-altair-materialise-and-renishaw`.

[11] J. O. Milewski. *Additive Manufacturing of Metals: From Fundamental Technology to Rocket Nozzles, Medical Implants, and Custom Jewelry.* Vol. 258. Springer, 2017. ISBN: 3319582054.

[12] E. O. Olakanmi, R. F. Cochrane, and K. W. Dalgarno. "A review on selective laser sintering/melting (SLS/SLM) of aluminium alloy powders: Processing, microstructure, and properties". In: *Progress in Materials Science* 74 (2015), pp. 401–477. ISSN: 00796425.

[13] R. Chou et al. "Additive Manufacturing of Al-12Si Alloy Via Pulsed Selective Laser Melting". In: *JOM* 67.3 (2015), pp. 590–596. ISSN: 1543-1851.

[14] E. O. Olakanmi. "Selective laser sintering/melting (SLS/SLM) of pure Al, Al–Mg, and Al–Si powders: Effect of processing conditions and powder properties". In: *Journal of Materials Processing Technology* 213.8 (2013), pp. 1387–1405. ISSN: 09240136.

[15] J. H. Tan, W. L. E. Wong, and K. W. Dalgarno. "An overview of powder granulometry on feedstock and part performance in the selective laser melting process". In: *Additive Manufacturing* 18 (2017), pp. 228–255. ISSN: 22148604.

[16] P. Mercelis and J. Kruth. "Residual stresses in selective laser sintering and selective laser melting". In: *Rapid Prototyping Journal* 12.5 (2006), pp. 254–265.

[17] J. Suryawanshi et al. "Simultaneous enhancements of strength and toughness in an Al-12Si alloy synthesized using selective laser melting". In: *Acta Materialia* 115 (2016), pp. 285–294. ISSN: 13596454.

[18] M. Cabrini et al. "Effect of heat treatment on corrosion resistance of DMLS AlSi10Mg alloy". In: *Electrochimica Acta* 206 (2016), pp. 346–355. ISSN: 00134686.

[19] K. G. Prashanth et al. “Microstructure and mechanical properties of Al–12Si produced by selective laser melting: Effect of heat treatment”. In: *Materials Science and Engineering: A* 590 (2014), pp. 153–160. ISSN: 09215093.

[20] M. Seifi et al. “Overview of Materials Qualification Needs for Metal Additive Manufacturing”. In: *JOM* 68.3 (2016), pp. 747–764. ISSN: 1543-1851.

[21] S. Siddique et al. “Influence of process-induced microstructure and imperfections on mechanical properties of AlSi12 processed by selective laser melting”. In: *Journal of Materials Processing Technology* 221 (2015), pp. 205–213. ISSN: 09240136.

[22] K. Prashanth et al. “Is the energy density a reliable parameter for materials synthesis by selective laser melting?” In: *Materials Research Letters* 5.6 (2017), pp. 386–390. ISSN: 2166-3831.

[23] F. C. R. Hernandez, J. M. H. Ramıérez, and R. Mackay. *Al-Si Alloys: Automotive, Aeronautical, and Aerospace Applications*. Springer, 2017.

[24] A. Popovich and V. Sufiiarov. “Metal Powder Additive Manufacturing”. In: *New Trends in 3D Printing*. InTech, 2016.

[25] E. Louvis, P. Fox, and C. J. Sutcliffe. “Selective laser melting of aluminium components”. In: *Journal of Materials Processing Technology* 211.2 (2011), pp. 275–284. ISSN: 0924-0136.

[26] T. Mukherjee, W. Zhang, and T. DebRoy. “An improved prediction of residual stresses and distortion in additive manufacturing”. In: *Computational Materials Science* 126 (2017), pp. 360–372. ISSN: 09270256.

[27] I. Rosenthal, A. Stern, and N. Frage. “Microstructure and Mechanical Properties of AlSi10Mg Parts Produced by the Laser Beam Additive Manufacturing (AM) Technology”. In: *Metallography, Microstructure, and Analysis* 3.6 (2014), pp. 448–453. ISSN: 2192-9262 2192-9270.

[28] M. Tang, P. C. Pistorius, and J. L. Beuth. “Prediction of lack-of-fusion porosity for powder bed fusion”. In: *Additive Manufacturing* 14 (2017), pp. 39–48.

[29] M. Tang and P. C. Pistorius. “Oxides, porosity and fatigue performance of AlSi10Mg parts produced by selective laser melting”. In: *International Journal of Fatigue* 94 (2017), pp. 192–201. ISSN: 01421123.

[30] W. E. King et al. “Observation of keyhole-mode laser melting in laser powder-bed fusion additive manufacturing”. In: *Journal of Materials Processing Technology* 214.12 (2014), pp. 2915–2925. ISSN: 0924-0136.

[31] R. Rai et al. “Heat transfer and fluid flow during keyhole mode laser welding of tantalum, Ti-6Al-4V, 304L stainless steel and vanadium”. In: *Journal of physics D: Applied physics* 40.18 (2007), p. 5753.

[32] R. Li et al. “316L stainless steel with gradient porosity fabricated by selective laser melting”. In: *Journal of Materials Engineering and Performance* 19.5 (2010), pp. 666–671. ISSN: 1059-9495.

[33] E. Brandl et al. “Additive manufactured AlSi10Mg samples using Selective Laser Melting (SLM): Microstructure, high cycle fatigue, and fracture behavior”. In: *Materials and Design* 34 (2012), pp. 159–169. ISSN: 02613069.

[34] J. N. D. Ngnekou et al. “Fatigue properties of AlSi10Mg produced by Additive Layer Manufacturing”. In: *International Journal of Fatigue* 119 (2019), pp. 160–172. ISSN: 0142-1123.

[35] ASTM. *Standard terminology for additive manufacturing - coordinate systems and test methodologies, Standard ISO/ASTM 52921*. Standard. ASTM International, 2013.

[36] S. Tammas-Williams et al. “XCT analysis of the influence of melt strategies on defect population in Ti–6Al–4V components manufactured by Selective Electron Beam Melting”. In: *Materials Characterization* 102 (2015), pp. 47–61.

[37] X. Wang et al. "The effect of atmosphere on the structure and properties of a selective laser melted Al–12Si alloy". In: *Materials Science and Engineering: A* 597 (2014), pp. 370–375. ISSN: 0921-5093.

[38] N. E. Dowling. *Mechanical behavior of materials: engineering methods for deformation, fracture, and fatigue*. Fourth. Pearson, 2012. ISBN: 0273764551.

[39] X. P. Li et al. "A selective laser melting and solution heat treatment refined Al–12Si alloy with a controllable ultrafine eutectic microstructure and 25% tensile ductility". In: *Acta Materialia* 95 (2015), pp. 74–82. ISSN: 13596454.

[40] W. F. Hosford. *Mechanical Behavior of Materials*. New York City: Cambridge University Press, 2010, p. 419.

[41] H. M. Westergaard. *Theory of elasticity and plasticity*. Reprint edition (1952). Dover Publications INC, 1952.

[42] F. Dunne and N. Petrinic. *Introduction to computational plasticity*. Oxford University Press on Demand, 2005. ISBN: 0198568266.

[43] T. L. Anderson. *Fracture mechanics: fundamentals and applications*. CRC press, 2017.

[44] T. Mura. *Micromechanics of defects in solids*. 2nd ed. Mechanics of Elastic and Inelastic Solids. Springer Netherlands, 1987. ISBN: 978-94-009-3489-4.

[45] J. D. Eshelby. "The determination of the elastic field of an ellipsoidal inclusion, and related problems". In: *Proceedings of the Royal Society of London. Series A. Mathematical and Physical Sciences* 241.1226 (1957), pp. 376–396. ISSN: 0080-4630.

[46] T. Mori and K. Tanaka. "Average stress in matrix and average elastic energy of materials with misfitting inclusions". In: *Acta metallurgica* 21.5 (1973), pp. 571–574. ISSN: 0001-6160.

[47] J. C. Sabotka, M. P. Enright, and C. McClung. "Application of critical distances to fatigue at pores". In: *Fatigue Fract Eng Mater Struct.* (2019), pp. 1–16.

[48] C. Weinberger, W. Cai, and D. Barnett. "Lecture notes–elasticity of microscopic structures". In: *ME340–Stanford University* (2005). URL: `http://micro.stanford.edu/~caiwei/me340b/content/me340b-notes_v01.pdf`.

[49] O. Pierard et al. "Micromechanics of elasto-plastic materials reinforced with ellipsoidal inclusions". In: *International Journal of Solids and Structures* 44.21 (2007), pp. 6945–6962. ISSN: 0020-7683.

[50] J. Lemaitre. *Handbook of Materials Behavior Models, Three-Volume Set: Nonlinear Models and Properties*. Elsevier, 2001. ISBN: 0080533639.

[51] K. J. Rasmussen. "Full-range stress–strain curves for stainless steel alloys". In: *Journal of constructional steel research* 59.1 (2003), pp. 47–61.

[52] D. C. Drucker. *Variational principles in the mathematical theory of plasticity*. Tech. rep. Brown University Providence RI DIV of Applied Mathematics, 1956.

[53] C. O. Frederick and P. Armstrong. "A mathematical representation of the multiaxial Bauschinger effect". In: *Materials at High Temperatures* 24.1 (2007), pp. 1–26. ISSN: 0960-3409.

[54] D. C. Drucker. "Some implications of work hardening and ideal plasticity". In: *Quarterly of Applied Mathematics* 7.4 (1950), pp. 411–418. ISSN: 0033-569X.

[55] L. R. Alejano and A. Bobet. "Drucker–Prager Criterion". In: *The ISRM Suggested Methods for Rock Characterization, Testing and Monitoring: 2007-2014*. Ed. by R. Ulusay. Cham: Springer International Publishing, 2015, pp. 247–252. ISBN: 978-3-319-07713-0.

[56] A. Franchi, F. Genna, and F. Paterlini. "Research note on quasi-convexity of the yield function and its relation to Drucker's postulate". In: *International journal of plasticity* 6.3 (1990), pp. 369–375. ISSN: 0749-6419.

[57] R. Hill. "On constitutive inequalities for simple materials—I". In: *Journal of the Mechanics and Physics of Solids* 16.4 (1968), pp. 229–242. ISSN: 0022-5096.

[58] R. Hill. "On constitutive inequalities for simple materials—II". In: *Journal of the Mechanics and Physics of Solids* 16.5 (1968), pp. 315–322. ISSN: 0022-5096.
[59] G. K. Sigworth. "Fundamentals of solidification in aluminum castings". In: *International Journal of Metalcasting* 8.1 (2014), pp. 7–20. ISSN: 1939-5981.
[60] K. G. Prashanth, S. Scudino, and J. Eckert. "Defining the tensile properties of Al-12Si parts produced by selective laser melting". In: *Acta Materialia* 126 (2017), pp. 25–35. ISSN: 13596454.
[61] M. Leary et al. "Selective laser melting (SLM) of AlSi12Mg lattice structures". In: *Materials & Design* 98 (2016), pp. 344–357. ISSN: 0264-1275.
[62] N. Kang et al. "Microstructure and strength analysis of eutectic Al-Si alloy in-situ manufactured using selective laser melting from elemental powder mixture". In: *Journal of Alloys and Compounds* 691 (2017), pp. 316–322. ISSN: 09258388.
[63] N. T. Aboulkhair et al. "On the Precipitation Hardening of Selective Laser Melted AlSi10Mg". In: *Metallurgical and Materials Transactions A* 46.8 (2015), pp. 3337–3341. ISSN: 1073-5623 1543-1940.
[64] N. T. Aboulkhair et al. "The microstructure and mechanical properties of selectively laser melted AlSi10Mg: The effect of a conventional T6-like heat treatment". In: *Materials Science and Engineering: A* 667 (2016), pp. 139–146. ISSN: 0921-5093.
[65] N. Read et al. "Selective laser melting of AlSi10Mg alloy: Process optimisation and mechanical properties development". In: *Materials and Design (1980-2015)* 65 (2015), pp. 417–424. ISSN: 02613069.
[66] C. Silbernagel et al. "Electrical resistivity of additively manufactured AlSi10Mg for use in electric motors". In: *Additive Manufacturing* 21 (2018), pp. 395–403. ISSN: 22148604.
[67] U. Tradowsky et al. "Selective laser melting of AlSi10Mg: Influence of post-processing on the microstructural and tensile properties development". In: *Materials & Design* 105 (2016), pp. 212–222.
[68] W. Li et al. "Effect of heat treatment on AlSi10Mg alloy fabricated by selective laser melting: Microstructure evolution, mechanical properties and fracture mechanism". In: *Materials Science and Engineering: A* 663 (2016), pp. 116–125. ISSN: 0921-5093.
[69] M. Awd et al. "Very high-cycle fatigue properties and microstructural damage mechanisms of selective laser melted AlSi10Mg alloy". In: *International Journal of Fatigue* 124 (2019), pp. 55–69.
[70] W. D. Callister and D. G. Rethwisch. *Materials science and engineering: an introduction*. Vol. 7. John Wiley & Sons New York, 2007.
[71] *AZO Materials Silicon*. Web Page. Accessed: 2019-02-27. URL: `https://www.azom.com/properties.aspx?ArticleID=599`.
[72] K. Kempen et al. "Process optimization and microstructural analysis for selective laser melting of AlSi10Mg". In: *Solid Freeform Fabrication Symposium*. Vol. 22, pp. 484–495.
[73] L.-Y. Liu, Q.-S. Yang, and Y. Zhang. "Plastic damage of additive manufactured aluminium with void defects". In: *Mechanics Research Communications* 95 (2019), pp. 45–51.
[74] I. Maskery et al. "Quantification and characterisation of porosity in selectively laser melted Al–Si10–Mg using X-ray computed tomography". In: *Materials Characterization* 111 (2016), pp. 193–204. ISSN: 1044-5803.
[75] S. A. Khairallah et al. "Laser powder-bed fusion additive manufacturing: Physics of complex melt flow and formation mechanisms of pores, spatter, and denudation zones". In: *Acta Materialia* 108 (2016), pp. 36–45. ISSN: 1359-6454.
[76] H. Atkinson and S. Davies. "Fundamental aspects of hot isostatic pressing: an overview". In: *Metallurgical and Materials Transactions A* 31.12 (2000), pp. 2981–3000. ISSN: 1073-5623.

[77] S. Tammas-Williams et al. "Porosity regrowth during heat treatment of hot isostatically pressed additively manufactured titanium components". In: *Scripta Materialia* 122 (2016), pp. 72–76. ISSN: 1359-6462.

[78] S. Tammas-Williams et al. "The effectiveness of hot isostatic pressing for closing porosity in titanium parts manufactured by selective electron beam melting". In: *Metallurgical and Materials Transactions A* 47.5 (2016), pp. 1939–1946. ISSN: 1073-5623.

[79] *MatWeb annealed 316L Strainless Steel*. Web Page. Accessed: 2019-05-16. URL: `http://www.matweb.com/search/datasheet.aspx?matguid=c02b8c0ae42e459a872553e0ebfab648&ckck=1`.

[80] D. Herzog et al. "Additive manufacturing of metals". In: *Acta Materialia* 117 (2016), pp. 371–392.

[81] C. Qiu et al. "A comprehensive study on microstructure and tensile behaviour of a selectively laser melted stainless steel". In: *Scientific reports* 8.1 (2018), p. 7785. ISSN: 2045-2322.

[82] R. Casati, J. Lemke, and M. Vedani. "Microstructure and fracture behavior of 316L austenitic stainless steel produced by selective laser melting". In: *Journal of Materials Science & Technology* 32.8 (2016), pp. 738–744. ISSN: 1005-0302.

[83] J. Čapek et al. "Highly porous, low elastic modulus 316L stainless steel scaffold prepared by selective laser melting". In: *Materials Science and Engineering: C* 69 (2016), pp. 631–639. ISSN: 0928-4931.

[84] E. Liverani et al. "Effect of selective laser melting (SLM) process parameters on microstructure and mechanical properties of 316L austenitic stainless steel". In: *Journal of Materials Processing Technology* 249 (2017), pp. 255–263.

[85] J. D. Majumdar et al. "Microstructure characterisation and process optimization of laser assisted rapid fabrication of 316L stainless steel". In: *Applied Surface Science* 247.1-4 (2005), pp. 320–327. ISSN: 0169-4332.

[86] A. Yadollahi et al. "Effects of process time interval and heat treatment on the mechanical and microstructural properties of direct laser deposited 316L stainless steel". In: *Materials Science and Engineering: A* 644 (2015), pp. 171–183. ISSN: 0921-5093.

[87] J. Suryawanshi, K. Prashanth, and U. Ramamurty. "Mechanical behavior of selective laser melted 316L stainless steel". In: *Materials Science and Engineering: A* 696 (2017), pp. 113–121. ISSN: 0921-5093.

[88] S. Yusuf et al. "Investigation on porosity and microhardness of 316L stainless steel fabricated by selective laser melting". In: *Metals* 7.2 (2017), p. 64.

[89] T. M. Mower and M. J. Long. "Mechanical behavior of additive manufactured, powder-bed laser-fused materials". In: *Materials Science and Engineering: A* 651 (2016), pp. 198–213.

[90] D. Kong et al. "Heat treatment effect on the microstructure and corrosion behavior of 316L stainless steel fabricated by selective laser melting for proton exchange membrane fuel cells". In: *Electrochimica Acta* 276 (2018), pp. 293–303. ISSN: 0013-4686.

[91] M. Montero Sistiaga et al. "Effect of heat treatment of 316L stainless steel produced by selective laser melting (SLM)". In: *Proceedings of the 27th Annual International Solid Freeform Fabrication Symposium-An Additive Manufacturing Conference*. 2016, pp. 558–565.

[92] F. Rahimidehgolan et al. "Determination of the Constants of GTN Damage Model Using Experiment, Polynomial Regression and Kriging Methods". In: *Applied Sciences* 7.11 (2017), p. 1179.

[93] A. He et al. "A comparative study on Johnson–Cook, modified Johnson–Cook and Arrhenius-type constitutive models to predict the high temperature flow stress in 20CrMo alloy steel". In: *Materials & Design (1980-2015)* 52 (2013), pp. 677–685. ISSN: 0261-3069.

[94] W. Ramberg and W. R. Osgood. "Description of stress-strain curves by three parameters". In: *Technical Note No. 902, National Advisory Comittee for Aeronotics* (1943).

[95] Y.-J. Kim et al. "On relevant Ramberg-Osgood fit to engineering nonlinear fracture mechanics analysis". In: *Journal of pressure vessel technology* 126.3 (2004), pp. 277–283.

[96] G. R. Johnson and W. H. Cook. "Fracture characteristics of three metals subjected to various strains, strain rates, temperatures and pressures". In: *Engineering fracture mechanics* 21.1 (1985), pp. 31–48. ISSN: 0013-7944.

[97] Dassault Systèmes. *Abaqus*. Version 2017. URL: `https://www.3ds.com/products-services/simulia/products/abaqus/`.

[98] A. V. Sobolev and M. V. Radchenko. "Use of Johnson–Cook plasticity model for numerical simulations of the SNF shipping cask drop tests". In: *Nuclear Energy and Technology* 2.4 (2016), pp. 272–276. ISSN: 24523038.

[99] A. Shrot and M. Bäker. "Determination of Johnson–Cook parameters from machining simulations". In: *Computational Materials Science* 52.1 (2012), pp. 298–304. ISSN: 0927-0256.

[100] J.-L. Chaboche. "A review of some plasticity and viscoplasticity constitutive theories". In: *International Journal of Plasticity* 24.10 (2008), pp. 1642–1693. ISSN: 0749-6419.

[101] T. Alena et al. "Elasto-plastic TCD as a method of failure prediction". In: *Procedia Structural Integrity* 5 (2017), pp. 569–576. ISSN: 2452-3216.

[102] Y. Zhao et al. "A comparative study on Johnson-Cook and modified Johnson-Cook constitutive material model to predict the dynamic behavior laser additive manufacturing FeCr alloy". In: *Journal of Alloys and Compounds* 723 (2017), pp. 179–187. ISSN: 0925-8388.

[103] F. J. Zerilli and R. W. Armstrong. "Dislocation-mechanics-based constitutive relations for material dynamics calculations". In: *Journal of applied physics* 61.5 (1987), pp. 1816–1825. ISSN: 0021-8979.

[104] *Ansys User's Manual, Zerilli-Armstrong Strength*. June 10, 2019. URL: `https://www.sharcnet.ca/Software/Ansys/16.2.3/en-us/help/wb_sim/ds_ex_mat_zeriarm.html`.

[105] F. H. Abed and G. Z. Voyiadjis. "A consistent modified Zerilli-Armstrong flow stress model for BCC and FCC metals for elevated temperatures". In: *Acta Mechanica* 175.1-4 (2005), pp. 1–18. ISSN: 0001-5970.

[106] D. Samantaray et al. "A thermo-viscoplastic constitutive model to predict elevated-temperature flow behaviour in a titanium-modified austenitic stainless steel". In: *Materials Science and Engineering: A* 526.1-2 (2009), pp. 1–6. ISSN: 0921-5093.

[107] Y. Lin, X.-M. Chen, and G. Liu. "A modified Johnson–Cook model for tensile behaviors of typical high-strength alloy steel". In: *Materials Science and Engineering: A* 527.26 (2010), pp. 6980–6986. ISSN: 0921-5093.

[108] H.-Y. Li et al. "A comparative study on modified Zerilli–Armstrong, Arrhenius-type and artificial neural network models to predict high-temperature deformation behavior in T24 steel". In: *Materials Science and Engineering: A* 536 (2012), pp. 216–222. ISSN: 0921-5093.

[109] Y. Lin and X.-M. Chen. "A combined Johnson–Cook and Zerilli–Armstrong model for hot compressed typical high-strength alloy steel". In: *Computational Materials Science* 49.3 (2010), pp. 628–633. ISSN: 0927-0256.

[110] R. Hill. "A theory of the yielding and plastic flow of anisotropic metals". In: *Proc. R. Soc. Lond. A* 193.1033 (1948), pp. 281–297. ISSN: 0080-4630.

[111] R. Hill. "Theoretical plasticity of textured aggregates". In: *Mathematical Proceedings of the Cambridge Philosophical Society*. Vol. 85. Cambridge University Press, pp. 179–191.

[112] R. Hill. "A user-friendly theory of orthotropic plasticity in sheet metals". In: *International Journal of Mechanical Sciences* 35.1 (1993), pp. 19–25. ISSN: 0020-7403.

[113] J. Martins, A. Andrade-Campos, and S. Thuillier. "Calibration of anisotropic plasticity models using a biaxial test and the virtual fields method". In: *International Journal of Solids and Structures* (2019).

[114] S. Zhang et al. "Calibration of anisotropic yield criterion with conventional tests or biaxial test". In: *International Journal of Mechanical Sciences* 85 (2014), pp. 142–151.

[115] P. L. Moore and G. Booth. *The welding engineer's guide to fracture and fatigue*. Elsevier, 2014. ISBN: 1782423915.

[116] A. L. Gurson. "Continuum theory of ductile rupture by void nucleation and growth: Part I—Yield criteria and flow rules for porous ductile media". In: *Journal of engineering materials and technology* 99.1 (1977), pp. 2–15. ISSN: 0094-4289.

[117] A. Slimane et al. "Parametric study of the ductile damage by the Gurson–Tvergaard–Needleman model of structures in carbon steel A48-AP". In: *Journal of Materials Research and Technology* 4.2 (2015), pp. 217–223.

[118] V. Tvergaard. "Influence of voids on shear band instabilities under plane strain conditions". In: *International Journal of Fracture* 17.4 (1981), pp. 389–407. ISSN: 1573-2673.

[119] V. Tvergaard. "On localization in ductile materials containing spherical voids". In: *International Journal of Fracture* 18.4 (1982), pp. 237–252. ISSN: 1573-2673.

[120] V. Tvergaard and A. Needleman. "Analysis of the cup-cone fracture in a round tensile bar". In: *Acta metallurgica* 32.1 (1984), pp. 157–169. ISSN: 0001-6160.

[121] S. Acharyya and S. Dhar. "A complete GTN model for prediction of ductile failure of pipe". In: *Journal of Materials Science* 43.6 (2008), pp. 1897–1909.

[122] C. Chu and A. Needleman. "Void nucleation effects in biaxially stretched sheets". In: *Journal of engineering materials and technology* 102.3 (1980), pp. 249–256. ISSN: 0094-4289.

[123] S. Hao and W. Brocks. "The Gurson-Tvergaard-Needleman-model for rate and temperature-dependent materials with isotropic and kinematic hardening". In: *Computational Mechanics* 20.1 (1997), pp. 34–40. ISSN: 1432-0924.

[124] Z. Zhang, C. Thaulow, and J. Ødegård. "A complete Gurson model approach for ductile fracture". In: *Engineering Fracture Mechanics* 67.2 (2000), pp. 155–168. ISSN: 0013-7944.

[125] K. Nahshon and J. Hutchinson. "Modification of the Gurson model for shear failure". In: *European Journal of Mechanics-A/Solids* 27.1 (2008), pp. 1–17. ISSN: 0997-7538.

[126] G. Rousselier. "Finite deformation constitutive relations including ductile fracture damage". In: *North-Holland Publ. Comp., Dourdan* (1981), pp. 331–335.

[127] G. Rousselier. "Ductile fracture models and their potential in local approach of fracture". In: *Nuclear engineering and design* 105.1 (1987), pp. 97–111. ISSN: 0029-5493.

[128] J. R. Rice and D. M. Tracey. "On the ductile enlargement of voids in triaxial stress fields". In: *Journal of the Mechanics and Physics of Solids* 17.3 (1969), pp. 201–217.

[129] Y. Hammi and M. Horstemeyer. "A physically motivated anisotropic tensorial representation of damage with separate functions for void nucleation, growth, and coalescence". In: *International Journal of Plasticity* 23.10-11 (2007), pp. 1641–1678. ISSN: 0749-6419.

[130] V. Tvergaard and C. Niordson. "Nonlocal plasticity effects on interaction of different size voids". In: *International Journal of Plasticity* 20.1 (2004), pp. 107–120. ISSN: 0749-6419.

[131] S. Nagaki, R. Sowerby, and M. Goya. "An anisotropic yield function for porous metal". In: *Materials Science and Engineering: A* 142.2 (1991), pp. 163–168. ISSN: 0921-5093.

[132] S. Nagaki, M. Goya, and R. Sowerby. "The influence of void distribution on the yielding of an elastic-plastic porous solid". In: *International journal of plasticity* 9.2 (1993), pp. 199–211. ISSN: 0749-6419.

[133] A. Kami et al. "Application of a GTN damage model to predict the fracture of metallic sheets subjected to deep-drawing". In: *Proceedings of the Romanian Academy, Series A* 15 (2014), pp. 300–309.

[134] Z. Chen and X. Dong. "The GTN damage model based on Hill'48 anisotropic yield criterion and its application in sheet metal forming". In: *Computational Materials Science* 44.3 (2009), pp. 1013–1021. ISSN: 0927-0256.

[135] S. M. Imani et al. "The modified Mori-Tanaka scheme for the prediction of the effective elastic properties of highly porous ceramics". In: *Ceramics International* 44.14 (2018), pp. 16489–16497. ISSN: 0272-8842.

[136] N. Soro et al. "Finite element analysis of porous commercially pure titanium for biomedical implant application". In: *Materials Science and Engineering: A* 725 (2018), pp. 43–50. ISSN: 09215093.

[137] S. Romano et al. "Qualification of AM parts: Extreme value statistics applied to tomographic measurements". In: *Materials & Design* 131 (2017), pp. 32–48. ISSN: 0264-1275.

[138] K. Solberg and F. Berto. "Notch-defect interaction in additively manufactured Inconel 718". In: *International Journal of Fatigue* 122 (2019), pp. 35–45. ISSN: 0142-1123.

[139] Y. Murakami and M. Endo. "Effects of defects, inclusions and inhomogeneities on fatigue strength". In: *International journal of fatigue* 16.3 (1994), pp. 163–182. ISSN: 0142-1123.

[140] M. El Haddad, K. Smith, and T. Topper. "Fatigue crack propagation of short cracks". In: *Journal of Engineering Materials and Technology* 101.1 (1979), pp. 42–46. ISSN: 0094-4289.

[141] R. Smith. "On the short crack limitations of fracture mechanics". In: *International Journal of Fracture* 13.5 (1977), pp. 717–720.

[142] S. Romano et al. "Fatigue properties of AlSi10Mg obtained by additive manufacturing: Defect-based modelling and prediction of fatigue strength". In: *Engineering Fracture Mechanics* 187 (2018), pp. 165–189.

[143] M. F. Horstemeyer. "Multiscale modeling: a review". In: *Practical aspects of computational chemistry*. Springer, 2009, pp. 87–135.

[144] M. Aghdam, S. Hosseini, and S. Morsali. "Simulation of interface damage in metal matrix composites under off-axis loading using cohesive zone model". In: *Computational Materials Science* 108 (2015), pp. 42–47.

[145] H. Shen and L. Brinson. "Finite element modeling of porous titanium". In: *International Journal of Solids and Structures* 44.1 (2007), pp. 320–335. ISSN: 0020-7683.

[146] J.-M. Gatt et al. "Elastic behavior of porous ceramics: application to nuclear fuel materials". In: *Journal of Nuclear Materials* 336.2-3 (2005), pp. 145–155. ISSN: 0022-3115.

[147] L. Chan, X. Lu, and K. Yu. "Multiscale approach with RSM for stress–strain behaviour prediction of micro-void-considered metal alloy". In: *Materials and Design* 83 (2015), pp. 129–137. ISSN: 0264-1275.

[148] *Abaqus Analysis User's Manual, Porous metal plasticity*. June 10, 2019. URL: `https://abaqus-docs.mit.edu/2017/English/SIMACAEMATRefMap/simamat-c-pormetalplas.htm#simamat-c-pormetalplas-t-elemsect1`.

[149] J. Zhou et al. "On the extension of the Gurson-type porous plasticity models for prediction of ductile fracture under shear-dominated conditions". In: *International Journal of Solids and Structures* 51.18 (2014), pp. 3273–3291.

[150] J. Fish and C. Oskay. "A nonlocal multiscale fatigue model". In: *Mechanics of Advanced Materials and Structures* 12.6 (2005), pp. 485–500. ISSN: 1537-6494.

[151] G. Tapia, A. Elwany, and H. Sang. "Prediction of porosity in metal-based additive manufacturing using spatial Gaussian process models". In: *Additive Manufacturing* 12 (2016), pp. 282–290. ISSN: 2214-8604.

[152] Y. Xu and C. Qian. "Application of Gurson–Tvergaard–Needleman Constitutive Model to the Tensile Behavior of Reinforcing Bars with Corrosion Pits". In: *PloS one* 8.1 (2013), e54368. ISSN: 1932-6203.

[153] Z. Zhang. "A practical micro mechanical model based local approach methodology for the analysis of ductile fracture of welded T-joints". In: *Lappeenranta: Lappeenrannan Teknillinen Korkeakoulu* 34 (1994).

[154] A. Falkowska, A. Seweryn, and J. Szusta. "Predicting the fatigue strength and life of 316L steel sinters of varying porosity for implants in a uniaxial loading state". In: *Engineering Fracture Mechanics* 200 (2018), pp. 146–165. ISSN: 0013-7944.

[155] A. Falkowska, A. Seweryn, and A. Tomczyk. "Fatigue life and strength of 316L sintered steel of varying porosity". In: *International Journal of Fatigue* 111 (2018), pp. 161–176.

[156] G. H. Bahrami and S. H. Hoseini. "Ductile Fracture Aanalysis of High-Strength Steel Bars Using Micromechanical GTN Model". In: *Journal of Stress Analysis* ().

[157] H. Richter. "Mote3D: an open-source toolbox for modelling periodic random particulate microstructures". In: *Modelling and Simulation in Materials Science and Engineering* 25.3 (2017), p. 035011. ISSN: 0965-0393.

[158] S. L. Omairey, P. D. Dunning, and S. Sriramula. "Development of an ABAQUS plugin tool for periodic RVE homogenisation". In: *Engineering with Computers* 35.2 (2019), pp. 567–577. ISSN: 1435-5663.

[159] J. Luo and R. Stevens. "Porosity-dependence of elastic moduli and hardness of 3Y-TZP ceramics". In: *Ceramics International* 25.3 (1999), pp. 281–286. ISSN: 0272-8842.

[160] L. F. Nielsen. "Elasticity and damping of porous materials and impregnated materials". In: *Journal of the American Ceramic Society* 67.2 (1984), pp. 93–98. ISSN: 0002-7820.

[161] K. K. Phani and S. K. Niyogi. "Young's modulus of porous brittle solids". In: *Journal of Materials Science* 22.1 (1987), pp. 257–263. ISSN: 1573-4803.

[162] R. Spriggs. "Expression for effect of porosity on elastic modulus of polycrystalline refractory materials, particularly aluminum oxide". In: *Journal of the American Ceramic Society* 44.12 (1961), pp. 628–629.

[163] J. P. Panakkal, H. Willems, and W. Arnold. "Nondestructive evaluation of elastic parameters of sintered iron powder compacts". In: *Journal of Materials Science* 25.2 (1990), pp. 1397–1402. ISSN: 1573-4803.

[164] J. Kováčik. "Correlation between Young's modulus and porosity in porous materials". In: *Journal of materials science letters* 18.13 (1999), pp. 1007–1010. ISSN: 0261-8028.

[165] J. W. Eaton et al. *GNU Octave version 4.2.0 manual: a high-level interactive language for numerical computations*. 2016. URL: `http://www.gnu.org/software/octave/doc/interpreter`.

[166] C. Bourcier et al. "Combs: Open source python library for RVE generation. Application to microscale diffusion simulations in cementitious materials". In: (2014), p. 02107. ISSN: 978-2-7598-1269-1.

[167] J. Gostick et al. "OpenPNM: a pore network modeling package". In: *Computing in Science & Engineering* 18.4 (2016), pp. 60–74.

[168] J. Schöberl. "NETGEN An advancing front 2D/3D-mesh generator based on abstract rules". In: *Computing and Visualization in Science* 1.1 (1997), pp. 41–52. ISSN: 1432-9360.

[169] P. Jana. "Elastic-plastic Behavior of an Ellipsoidal Inclusion Embedded in an Elastic Matrix". In: *Procedia engineering* 173 (2017), pp. 1116–1121. ISSN: 1877-7058.

[170] L. Chan, K. Au, and K. Yu. "FEM–CT integrated design for multiscale damage analysis of hydroformed magnesium-based alloy tubular product". In: *NDT & E International* 56 (2013), pp. 38–47. ISSN: 0963-8695.

[171] K. Solberg et al. “Fatigue of additively manufactured 316L stainless steel: the influence of porosity and surface roughness”. In: *Fatigue & Fracture of Engineering Materials and Structures* 40th Anniversary special issue (2019).

[172] ASTM. *Standard practice for conducting force controlled constant amplitude axial 369 fatigue tests of metallic materials, Standard ASTM E466-15*. Standard. ASTM International, 2015.

[173] E. Hart. “Theory of the tensile test”. In: *Acta metallurgica* 15.2 (1967), pp. 351–355. ISSN: 0001-6160.

[174] H. B. Motra, J. Hildebrand, and A. Dimmig-Osburg. “Assessment of strain measurement techniques to characterise mechanical properties of structural steel”. In: *Engineering Science and Technology, an International Journal* 17.4 (2014), pp. 260–269.

[175] E. Jones, T. Oliphant, P. Peterson, et al. *SciPy: Open source scientific tools for Python*. [Online; accessed 30.04.2019]. 2001. URL: `http://www.scipy.org/`.

[176] E. Voce. “The relationship between stress and strain for homogeneous deformation”. In: *Journal of the Institute of Metals* 74 (1948), pp. 537–562.

[177] D. Umbrello, R. M’saoubi, and J. Outeiro. “The influence of Johnson–Cook material constants on finite element simulation of machining of AISI 316L steel”. In: *International Journal of Machine Tools and Manufacture* 47.3-4 (2007), pp. 462–470. ISSN: 0890-6955.

[178] N. Tounsi et al. “From the basic mechanics of orthogonal metal cutting toward the identification of the constitutive equation”. In: *International Journal of Machine Tools and Manufacture* 42.12 (2002), pp. 1373–1383. ISSN: 0890-6955.

[179] H. Chandrasekaran, R. M’saoubi, and H. Chazal. “Modelling of material flow stress in chip formation process from orthogonal milling and split Hopkinson bar tests”. In: *Machine Science and Technology* 9.1 (2005), pp. 131–145. ISSN: 1091-0344.

[180] A. Yadollahi et al. “Quantification of tensile damage evolution in additive manufactured austenitic stainless steels”. In: *Materials Science and Engineering: A* 657 (2016), pp. 399–405. ISSN: 0921-5093.

[181] N. Kurgan and R. Varol. “Mechanical properties of P/M 316L stainless steel materials”. In: *Powder Technology* 201.3 (2010), pp. 242–247.

[182] Y. Zhong et al. “Intragranular cellular segregation network structure strengthening 316L stainless steel prepared by selective laser melting”. In: *Journal of Nuclear Materials* 470 (2016), pp. 170–178.

[183] A. Matzenmiller, J. Lubliner, and R. Taylor. “A constitutive model for anisotropic damage in fiber-composites”. In: *Mechanics of materials* 20.2 (1995), pp. 125–152.

[184] R. Garrett, J. Lin, and T. Dean. “An investigation of the effects of solution heat treatment on mechanical properties for AA 6xxx alloys: experimentation and modelling”. In: *International Journal of Plasticity* 21.8 (2005), pp. 1640–1657.

[185] R. Cudeck and S. J. Henly. “Model selection in covariance structures analysis and the" problem" of sample size: A clarification”. In: *Psychological bulletin* 109.3 (1991), p. 512. ISSN: 1939-1455.

A Orientation Specification in AM

Orientation Specification schematic adopted from Ref. [3].

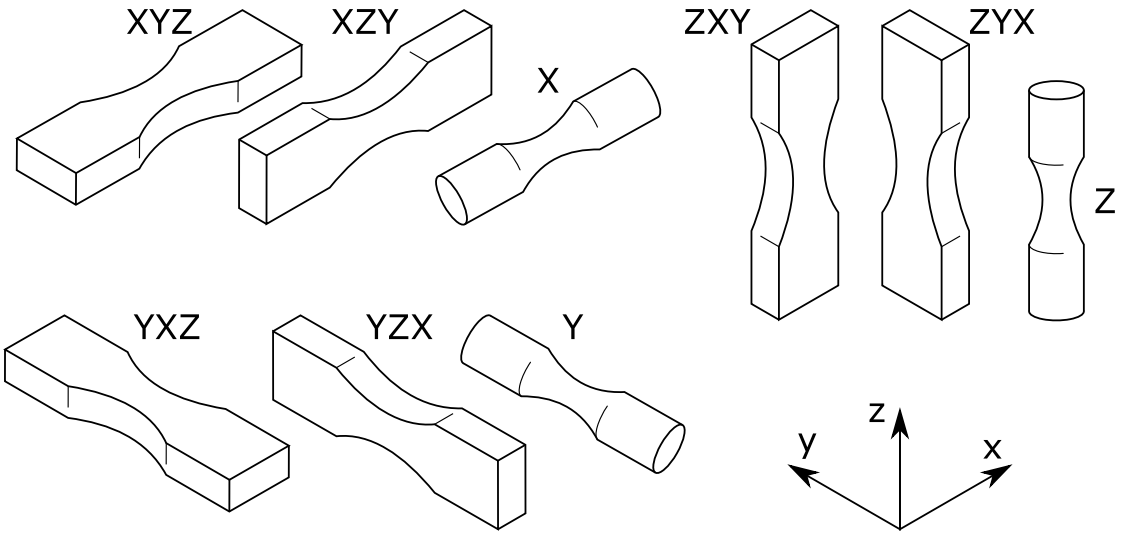

B Summary of Tensile Properties, SLM Al-12Si

Abbreviations: As-Built(AB), Not Available/Applicable (NA), Base Plate Heating (BPH), Single Hatch (SH), Checkerboard Hatch (CH), Double Hatch (DH), Orientation specifications, see Appendix A.

Alloy	Reference	$P, (w)$	$v, (\frac{mm}{s})$	$h(\mu m)$	$t, (\mu m)$	$E_d, (\frac{W}{mm})$	Other info	Orientation	Hatching	Heat Treatment	$\sigma_y, (MPa)$	UTS,(MPa)	$\varepsilon_f, (\%)$	$\sigma_{th}, (MPa)$
Cast A360	ASTM										165	315	3,5	NA
Cast A360	Dynacast										170	317	3,5	
Cast AlSi12	Matweb										131	290	3,5	130 @ 5E8
SLM Al-12Si	[62]	300	500	50	45	266,7	NA	NA	NA	AB	NA	275	9,20	NA
			750			177,8						259	8,2	
			1000			133,3						217	7,2	
	[60]	320	1455	110	50	40,0	/W Contour	ZXY	SH	AB	260	385	2,8	NA
									DH		235	390	3,3	
									SHC		260	400	3	
									CH		290	460	4,5	
							/Wo Contour		SH		200	410	6,6	
							BPH 200°C		NA		230	378	3,5	
							BPH 300°C				182	310	3,9	
							BPH 400°C				115	222	9,5	
	[39]	200	500	150	50	53,3	NA	XZY	NA	AB	240	360	4	NA
										500°C 15min	119	202	22	
										500°C 30min	108	189	25	
										500°C 2h	118	187	25	
										500°C 4h	101	175	25	
	[17]	320	1455	110	50	40,0	NA	XYZ	SH	AB	270	325	4,4	60 @ 1E7
								ZYX			274	296	2,2	NA
								XYZ		300°C 6h	153	228	5,3	110 @ 1E7
								ZYX		300°C 6h	150	210	4,2	NA
								XYZ	CH	AB	262	330	3,9	70 @ 1E7
								ZYX			276	302	2,3	NA
	[37]	200	500	150	50	53,0	N2 Chamber	XZY	DH	AB	224	368	4,8	NA
			1000			27,0					222	366	3,8	
			1500			18,0					180	338	2,4	
			2000			13,0					178	246	1,1	
	[21]	300	1200	250	50	20,0	NA	Z	CH	AB	184	231	1,18	NA
										240°C	180	220	1,05	
							BPH 200°C			AB	154	190	0,98	
							BPH 200°C			240°C	187	230	1,12	
		350	930	190	50	39,6	NA			AB	221	419	3,91	
										240°C	219	372	3,41	
							BPH 200°C			AB	202	369	4,38	
							BPH 200°C			240°C	202	361	4,05	80 @ 1E7
	[19]	320	1455	110	50	40,0	/W Contour	Z	DH	AB	260	384	2,8	NA
										300°C 6h	175	275	4,9	
										452°C 6h	95	143	13	

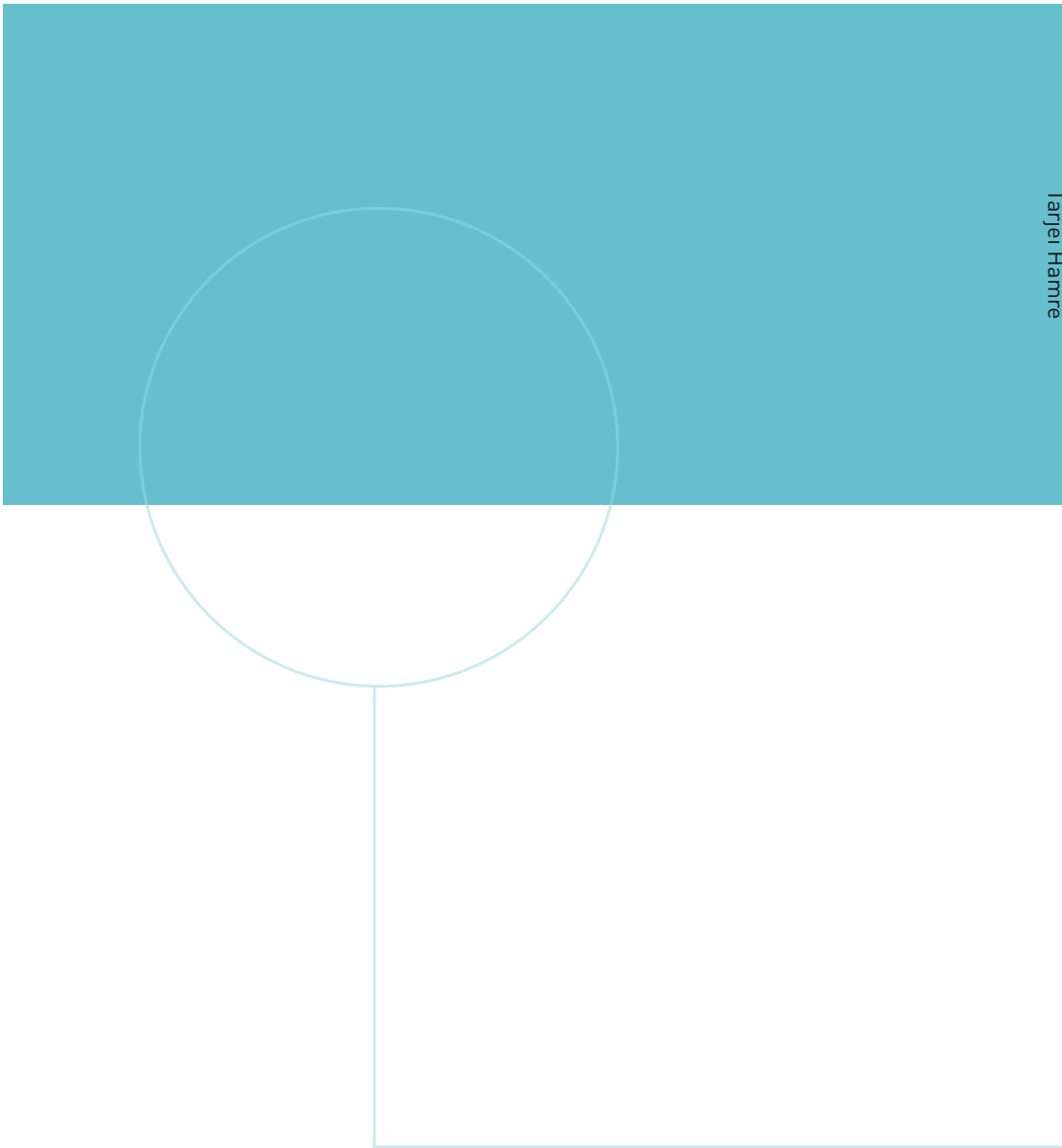

Tarjei Hamre

NTNU
Kunnskap for en bedre verden